Hot Working Characteristics of AISI 321 in Comparison to AISI 304 Austenitic Stainless Steels

By

Richard C. K. Nkhoma

Supervised by:

Dr. Charles W. Siyasiya

and

Professor Waldo E. Stumpf

Submitted in fulfilment of the requirements of the degree

PHILOSOPHIAE DOCTOR (METALLURGY)

In the

Department of Materials Science and Metallurgical Engineering

Faculty of Engineering, Built Environment and Information Technology

University of Pretoria

Republic of South Africa

04 April 2014

Candidate : Richard. C.K. Nkhoma

Supervisors : Dr. Charles W. Siyasiya

Professor Waldo E. Stumpf

Department : Materials Science and Metallurgical Engineering

Degree : Philosophiae Doctor (Metallurgy)

SUMMARY

Although the austenitic stainless steels 304 and 321 are often treated nominally as equivalents in their hot rolling characteristics, the question remains whether any subtle differences between the two allow further optimisation of their respective hot rolling schedules. The hot workability of these two types of austenitic stainless steels was compared through single-hit Gleeble simulated thermomechanical processing between 800°C and 1200°C while the strain rate was varied between $0.001\mathrm{s}^{-1}$ and $5\mathrm{s}^{-1}$. It was found that the constants for the hyperbolic sinh equation for hot working of AISI 321 steel are $\mathrm{Q} = 465\ \mathrm{kJ/mol}$, $A_3 = 9.76 \times 10^{17}\ \mathrm{MPa}^{-1}s^{-1}$, $\alpha = 0.009\ \mathrm{MPa}^{-1}$ and $n = 6.1$ while for 304 steel the constants are $\mathrm{Q} = 446\ \mathrm{kJ/mol}$, $A_3 = 2.14 \times 10^{17}\ \mathrm{MPa}^{-1}s^{-1}$, $\alpha = 0.008\ \mathrm{MPa}^{-1}$and $n = 6.1$. It is shown that the occurrence of dynamic recrystallisation starts when the Zener-Hollomon parameter $\mathrm{Z} \approx 6.4 \times 10^{17}\mathrm{s}^{-1}$ for both steels but that the differences in the values of Q and A_3 (the structure factor) between the two steels does lead to consistently lower steady state stresses for the steel 321 than is found in the steel 304 at the same Z values. This may, therefore, offer some scope for further optimisation of the hot rolling schedules and in particular in the mill loads of these two respective steels.

A modelled constitutive equation derived from hot working tests to predict hot rolling mill loads is proposed and validated against industrial hot rolling data for AISI 321 stainless steel. Good correlation is found between the predicted Mean Flow Stress, the Zener-Hollomon Z parameter and actual industrial mill load values from mill logs if allowances are made for differences in Von Mises plane strain conversion, friction and front or back end tension. The multipass hot working behaviour of this steel was simulated through Gleeble thermomechanical compression testing with the deformation temperature varying between 1200°C down to 800°C and the strain rate between $0.001\mathrm{s}^{-1}$ and $5\mathrm{s}^{-1}$. At strain rates greater than $0.05\mathrm{s}^{-1}$, dynamic recovery as a softening mechanism was dominant, increasing the dynamic recrystallisation to dynamic recovery transition temperature $\mathrm{DR}_{\mathrm{TT}}$ to higher temperatures. This implies that through extrapolation to typical industrial strain rates of about $60\mathrm{s}^{-1}$,most likely no dynamic recrystallisation in plant hot rolling occurs in this steel but only dynamic recovery. Grain refinement by DRX is, therefore, unlikely in this steel under plant hot rolling conditions. Finally, mill load modelling using the hot working constitutive constants of the near-equivalent 304 instead of those specifically determined for 321, introduces measurable differences in the predicted mill loads. The use of alloy-specific hot working constants even for near-equivalent steels is, therefore, recommended.

Key words: dynamic recrystallisation (DRX), dynamic recovery (DRV), AISI 321, constitutive equation, mean flow stress (MFS), dynamic recrystallisation to dynamic recovery transition temperature (DR_{TT}), hot working, modelling.

ACKNOWLEDGEMENT

I am deeply grateful to have had two knowledgeable and encouraging advisors Professor Waldo E. Stumpf and Dr. Charles W. Siyasiya who successfully guided this research to the end. I am particularly indebted for their professional and wonderful ideas, encouragement, support, and confidence they had in me.

I would like to express my sincere thanks to all members of the Materials Science and Metallurgical Engineering Department, University of Pretoria, the likes of Professor G. T. Van Rooyen and Dr. Kevin Banks, who directly and indirectly helped me throughout this research and made it possible and enjoyable.

I am also very much thankful and deeply appreciate the pleasant and friendly international environment created by my fellow postgraduate students like Kofi Annan (not the former Secretary General of UN) and the like along with their knowledge, expertise and skills.

Finally, I would like to express my sincere gratitude to my wife Catherine and kids Peace, Pempho and Phemelo for their never ending love, spiritual and emotional support, empathy and patience, and counsel and appreciation and friends for their continuous support and encouragement.

This thesis is dedicated to

my wife Catherine

and my kids

Peace, Pempho and Phemelo

PUBLICATIONS FROM THE STUDY

1. R. C. K. Nkhoma, C. W. Siyasiya, and W. E. Stumpf, "Hot workability of AISI 321 and AISI 304 austenitic stainless steels," Journal of Alloys and Compounds, Vol 595, 2014, pp 103-112.
2. R. C. K. Nkhoma, C. W. Siyasiya, and W. E. Stumpf, "Constitutive Modelling of Mill Loads during Hot Rolling of AISI 321 Austenitic Stainless Steel," International Journal of Materials Research (formerly: Zeitschrift fuer Metallkunde) (accepted manuscript no. MR3976R1), 2014.
3. R. C. K. Nkhoma, C.W. Siyasiya and WE Stumpf, "Hot Working Characteristics of AISI 321 in Comparison to AISI 304 Austenitic Stainless Steel". The Southern African Institute of Mining and Metallurgy: Ferrous and Base Metals Development Network Conference, 15 to 17 October 2012, Magaliesburg, South Africa, ISBN 978-1-920410-33-9.

TABLE OF CONTENTS

LIST OF FIGURES

LIST OF TABLES

CHAPTER 1: BACKGROUND

1.1 Introduction

Steel is a ferrous metal which primarily contains carbon in proportion to iron, with iron as the main element. Iron in its raw form has the tendency to corrode when it combines with oxygen and water. Corrosion of steel is unwanted in most cases and this led to the development of various types of corrosion resistant steels. There are many types of steel whose classification varies; out of which stainless steel is isolated since it is the primary focus in this work. Stainless steel has been in use since the early 1900s and is made up of an alloy of iron with a minimum of 10.5% chromium. It is the presence of chromium in stainless steels that generally protects the metal from corrosion attack. Metals that are classified as stainless got their name from their resistive behaviour to corrosive attack. Since stainless steel resists attack, it does not stain or rust hence the name stainless.

Stainless steel has been developed into several types over the years and it is mainly classified according to their respective microstructures. The commonly found types are: austenitic (which are face centred cubic, fcc), ferritic (which are body centred cubic, bcc), martensitic (which are body centred tetragonal, bct), duplex (containing both austenite and ferrite), precipitation hardening and super alloyed stainless steels. The common alloy classification or series numbers used to make these stainless steels are popularly known as the 100, 200, 300, 400, 500, and 600 series[1], precipitation hardening (PH) and duplex stainless steels.

Austenitic stainless steels are an allotrope of Fe that have a γ structure as the main phase of the matrix and generally are not magnetic in nature and they have relatively low yield strength, high ductility, excellent weldability and impact toughness down to the true absolute zero temperature with no steep ductile to brittle transition (DBTT) and they are usually found in alloy forms of chromium–manganese–nickel (Cr–Mn–Ni). Austenitic steels have an fcc atomic crystal structure which provides more slip planes and slip directions for the flow of dislocations. A dislocation is a lattice line defect that defines the boundary between slipped and unslipped portions of the crystal and this happens on the atomic scale. It is because of this that this material has no clearly defined yield point, which is why its yield strength is always expressed as a proof stress. The American Iron and Steel Institute (AISI) has several standards for a wide range of stainless steels grades. Figure 1.1 shows some of the common series' groups of austenitic stainless steel which are classified according to AISI and of interest in this research report are AISI 304 and AISI 321 stainless steels.

Generally all austenitic stainless steels cannot be hardened by heat treatment but can be hardened through work hardening or through utilisation of alloying elements or through grain size refinement. As for work hardening, the increase in strength comes because of the low stacking fault energy and the formation of deformation induced martensite which give rise to high strain hardening, leading to a higher flow strength [2].

The importance of controlling thermomechanical processing of steels cannot be over emphasized. It is through the understanding and control of the microstructure's evolution during thermomechanical processing that the desired properties of steels and metals in general are optimised. During plastic deformation of materials, defects in the crystal structure are introduced mainly in the form of dislocations.

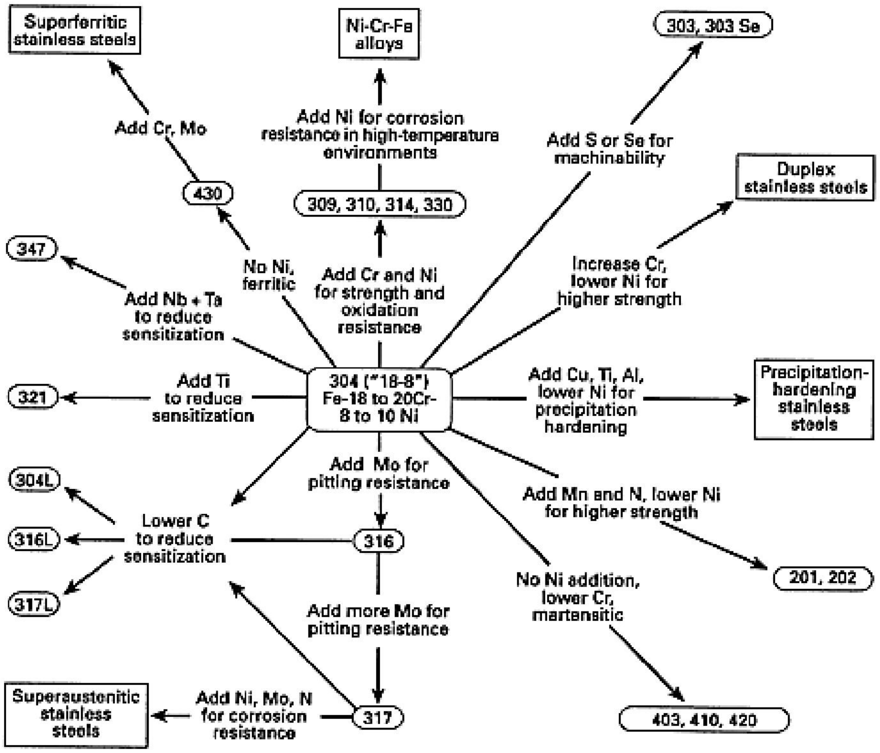

Figure 1.1: **Composition and property linkages in the stainless steel family of alloys**[3].

It is through these dislocations that energy is stored in the deformed material and in hot working this stored energy is released through two main predominant mechanisms that take place which are dynamic recrystallisation (DRX) and dynamic recovery (DRV) which are then followed by grain growth [4]. There is competition between DRV and DRX for this stored energy. Other mechanisms that may occur during deformation are metadynamic recrystallisation (MDRX) and static recrystallisation (SRX). By definition, DRX is when microstructures change as a material (a metal in this case) undergoes simultaneous annealing and deformation at high temperatures. Recrystallisation is characterised by the formation of a new grain structure in a deformed material, mostly by the formation and migration of high angle grain boundaries driven by the stored energy of deformation. More information on DRX and DRV will be presented later under the literature review. High angle grain boundaries are those with greater than 10° to 15° misorientation [4]. Contrary to DRX, there is no migration of a high angle grain boundary in DRV. Instead DRV causes dislocations to polygonise into subgrains [5]. The new grains so produced out of a DRX process are assumed to be relatively strain and stress free with an annealed dislocation content. This phenomenon is more prominent in material with a low stacking fault energy (SFE) and austenitic stainless steel is one example of such materials [6], [7].

Apparently it is very difficult to quantify what goes on instantaneously during deformation and more specifically to conclude that indeed DRX has taken place as deformation of a DRX–grain takes place again immediately after the DRX. The only evidence for DRX is the observation of equiaxed grains. Dynamic recrystallisation is also sometimes referred to as dynamic softening simply because the microstructure changes during hot deformation, with the hardness of the material becoming lower. When nucleation and growth of new grains take place after plastic deformation at elevated temperature, sometimes even during interpass times, the phenomenon is referred to as static recrystallisation or SRX. The occurrence of DRX brings about two things which are grain refinement and reduction in deformation resistance [8].

1.2 Uses of AISI 304 and AISI 321

AISI 304 is the most widely used austenitic stainless steel and the motivation to introduce AISI 321 was to extend the uses of AISI 304 by making the steel more weldable through inhibition of sensitisation, i.e. the withdrawal of chromium from areas adjacent to grain boundaries by the formation of Cr-containing $M_{23}C_6$. It exhibits relatively good corrosion resistance and forming characteristics. It is used in petrochemical and fertiliser industries, dairy product processing equipment, food processing, pharmaceutical industries, hospitals, kitchenware, sinks, cutlery, cryogenic vessels, as heat exchangers in air conditioning, refrigeration, textile machinery, distilleries etc.

AISI 321 resists scaling and vibration fatigue. It is used for aircraft exhaust stacks and exhaust manifolds in general, welding, pressure vessels, mufflers for engines, carburettors, expansion bellows, stack liners, fire walls and furnace parts, etc [9].

1.3 The Hot rolling process

Rolling of metals is defined as the process of plastically deforming the metal by passing it between the rolls where the material is subjected to high compressive stresses from the squeezing action of the rolls. This process is done when the metal is either cold, warm or hot. When it is done as the metal is cold, it is referred to as cold rolling while when it is done at elevated temperature the process is called hot rolling. If the process is performed below the A_{c1} temperature, it is referred to as warm rolling in carbon steels.

The initial breakdown of steel ingots into blooms and billets is mostly done by hot–rolling. This process is further followed by hot rolling into a number of products such as plates, sheets, rods, bars, pipes, rails. Hot rolling at Columbus Stainless SA is done through the Cold Charge Route (CCR) where the slabs from the continuous caster are allowed to cool to room temperature before reheating to the austenitising temperature of about 1200°C before hot rolling. When the slab has, therefore, cooled down, it is taken to the slab grinders where the top and bottom surfaces are removed through grinding (also known as “scarfing”) to smoothen the slab as well as to remove the surface impurities and defects from the outer layers. From the slab grinders, the slab is then taken to the reheat furnace where it is heated to the austenitising temperature before entering the roughing mill. The entry thickness into the roughing mill is about 200 mm which can be reduced down to about 15 mm after several passes. After the reductions in the roughing mill, the slab changes to a “transfer bar”.

From the roughing mill, the transfer bar then enters the Steckel mill which is shown in the sketch of Figure 1.2 in which the mill is made up of a four–high reversing stand rolls which are located below point B in the sketch. This reduces the transfer bar to the desired finished strip thickness in a number of passes. To keep the material hot during the rolling process, the strip is coiled after each pass into one of the two Steckel coil boxes located on the entry and exit sides shown as either A or C in the sketch. The heat in the coil boxes maintains the strip temperature at the desired level [10]. The requirement to effectively reduce the slab to such smaller thicknesses call for a plain strain operation which is possible only if the lubrication during rolling is very efficient [11]. After the Steckel mill, the transfer bar now changes to strip. It is after this process that the outlined problem of the type AISI 321 steel manifests itself.

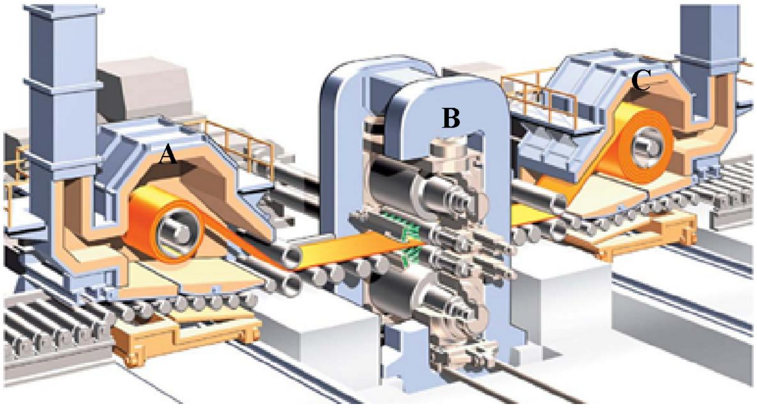

Figure 1.2: Sketch of a Steckle mill[10].

1.4 Problem statement

This project seeks to find solutions to improve the hot working characteristics of AISI 321 stainless steel. Type AISI 321 stainless steel has almost the same chemical composition as type AISI 304 with the only major difference being the addition of titanium to the former for stabilisation of the carbon and nitrogen. The Ti captures the C in the form of TiC and Ti(CN) to avoid sensitisation. Type AISI 321 austenitic stainless steel generally suffers from both metallurgical defects from Ti–inclusions and low room temperature strength as carbon (C) is tied up in TiC/Ti(CN). The challenge is that reducing the C content in order to reduce the amount of Ti required for stabilisation, leads to low strength as less C would be in solid solution at room temperature in this steel.

1.5 Research plan

Figure 1.3 shows the decision tree that was taken to address the problem which is either via route labelled 1: that proposes to optimise the chemical composition or via route labelled 2:

that proposes to optimise the rolling process. In order to address the problem at hand, the following steps were taken:

- Experimental tests were done to determine the hot rolling parameters for both types of stainless steel (AISI 304 and AISI 321)
- Type 304 stainless steel is taken as a bench mark because it doesn't manifest the problems as experienced by type 321.
- The challenge was the maximum strain rate that the machine (Gleeble 1500™) at the University of Pretoria can handle. To address this, specimens were taken to UCT because they have a high strain rate Gleeble machine that can handle higher strain rates which are synonymous with industrial strain rates.
- After the determination of the hot rolling constants, the onset of dynamic recrystallisation of these materials was determined.
- From the results obtained the recommendations and conclusions were drawn.

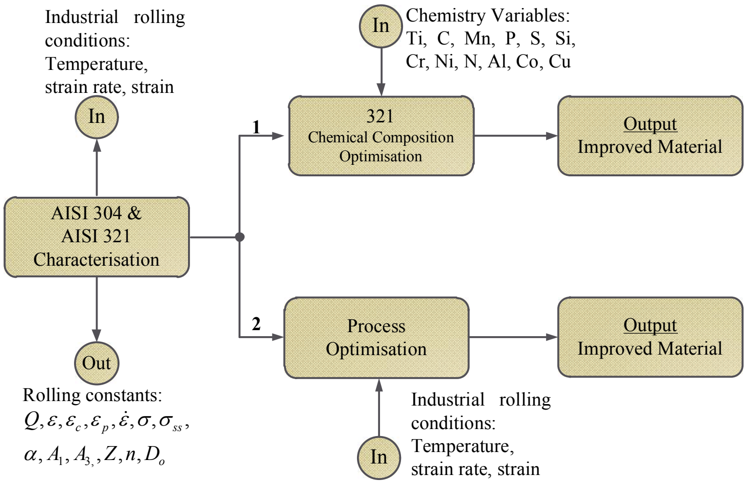

Figure 1.3: **The process decision tree taken to address the problem**

1.6 Objectives

There is more information in the literature on the dynamic recrystallisation and dynamic recovery of 304 stainless steel as compared to 321 and that's why 304 was taken as a benchmark as its experimental results can be easily compared. The objectives of this work were:

1. To evaluate the hot working characteristics of type 304 and type 321 austenitic stainless steels.
2. To develop and implement a model that can predict the onset of recrystallisation in type 321 austenitic stainless steel.
3. To study and optimise the mechanical properties of type 321 austenitic stainless steel through the thermomechanical process.
4. To highlight the subtle (hot working) differences between 321 and 304 steels.

1.7 Conclusion

The flow stress (σ) – strain (ε) curves were used to identify the type of restoration mechanism that was taking place in the material during rolling, be it cold, warm or hot deformation and in this report these curves will be utilised extensively. For example, as DRX takes place during hot deformation, the σ–ε curve displays a behaviour with a single peak stress followed by a gradual decline toward a steady state. As for DRV, the process is generally characterised by the flow stress curve profile that rises to a peak and then reaches a steady state plateau without coming down.

It is worth mentioning that flow stress is a true reflection of microstructure changes that are taking place during deformation and this implies that the analyses based on σ–ε curves have indeed a meaning for the behaviour of metals and alloys. Austenitic stainless steels do not transform on cooling and the high solute levels are said to retard static recrystallisation, making it easier to study both dynamic recovery and recrystallisation. Therefore, in the prediction of forging or rolling loads it is imperative to be able to accurately predict the occurrence and extent of dynamic recrystallisation and dynamic recovery if accurate scheduling parameters' predictions are required as they have an influence on the mechanical properties of the final product.

CHAPTER 2: STRENGTHENING MECHANISMS IN STAINLESS STEELS

2.1 Introduction

Austenitic stainless steels are derived from the Fe-Cr–Mn–Ni alloy system with the addition of austenite formers, which extend the $\gamma - Fe$ region by promoting the formation of austenite. In addition to the minimum prescribed elements by AISI, the two steels being investigated also contain the following additional elements: (a) 304: Co, Cu and O, (b) 321: Ti, Co, Al, Cu and O. The precise compositions of these two steels will be presented latter.

Alloying elements are added to steels for a number of reasons such as (a) to provide solid solution strengthening, (b) to cause the precipitation of alloy carbides rather than that of Fe_3C, (c) to improve corrosion resistance and other special characteristics of the steel, (d) for grain refinement, and (e) improve the hardenability. In alloy steels, the alloying elements can be found in various forms such as (a) in the free state; (b) as intermetallic compounds with iron or with each other; (c) as oxides, sulphides and other non–metallic inclusions or (d) in the form of carbides, nitrides or often as carbonitrides [12].

There are several ways that can be employed in order to improve the mechanical strength properties of materials. Basically, the mechanical properties of the materials are controlled by the microstructure. Some of the suggested methods to improve the material's strength are: solid solution strengthening, work hardening, precipitation hardening, grain boundary strengthening, strengthening from second phase particles, martensitic strengthening, preferred orientation (texture) and dispersoids (dispersion strengthening) among other methods [13]. The fundamental principle for a metal to plastically deform depends on the ease of dislocations to move and propagate. Strengthening methods capitalise on restricting dislocation motion by raising the dislocation density to render a material harder and stronger. In other words, plastic deformation stores energy in the form of dislocations and also distorts the shape of the grains and it is this stored energy that acts as the driving force for the nucleation and growth of new grains in both DRX and SRX. In order to obtain material of the required strength sometimes some of the mechanical properties are sacrificed such as ductility and toughness. Under hot working situations, there are very few options that can be exploited in order to improve the strength of the material and these are: solid solution strengthening, work hardening, grain boundary strengthening, strengthening from second phase particles, and preferred orientation (texture). The following subsections offer an explanation on how these strengthening mechanisms operate.

2.1.1 Solid solution strengthening

Solid solution is defined as a homogeneous crystalline phase that contains two or more chemical species [14] where the solute (sometimes even impurity) atoms are randomly distributed throughout the matrix. There are two types of solid solutions as depicted in Figure 2.1 which are: (a) substitutional solid solution where the solute and solvent atoms are somewhat similar in size (not more than $\pm 15\%$ difference with the solvent atoms) where part of the solvent atoms are substituted by atoms of the alloying element and this makes the solute atoms to occupy lattice spaces of the solvent atoms in the matrix and (b) interstitial solid solution where the solute atoms are smaller in size as compared to the solvent atom which makes the solute atoms to occupy the interstitial spaces in the solvent lattice of the matrix. The governing equation is given by[15]:

$$\Delta\tau = Gb\varepsilon^{2/3}c^{1/2} \qquad [2\text{-}1]$$

where $\Delta\tau$ is the incremental shear stress necessary to overcome dislocation barriers, G is the shear modulus, b is the Burger's vector ε is the lattice strain due to the solute/solvent misfit and c is the concentration of the solute atoms, generally in atomic concentration terms.

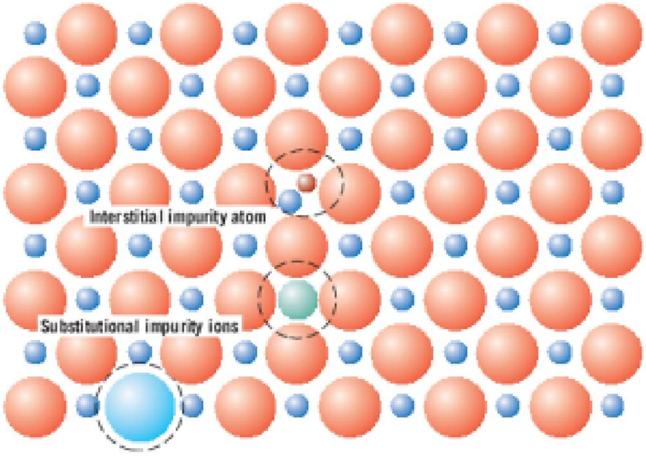

Figure 2.1: Schematic representation of solid solution [14]**.**

Solid solution strengthening therefore capitalises on the use of alloying elements that can be used to improve the strength of the material by adding alloying elements to the crystalline lattice of the base metal. As said before, the strength of a material depends on the ease of the dislocation's movement as these dislocations create stress fields within the material. Local stress fields are formed when the solute atoms are introduced by imposing lattice strains on the surrounding host atoms which could either be compressive strains or tensile strains as shown in Figure 2.2. The compressive or tensile lattice strains interact with stress fields that are created by dislocations by either attracting or repelling dislocations [14]. The net effect is that the dislocation's motion is restricted, thereby causing an increase in the yield stress of the material and this eventually has an overall effect on the strength of the material. Second phase compounds and precipitates generally form when the solubility of solute elements in solution surpasses the requirement of solid solution. They are soluble at high temperatures but insoluble at low temperatures. These compounds also play an important role in strengthening of some steels.

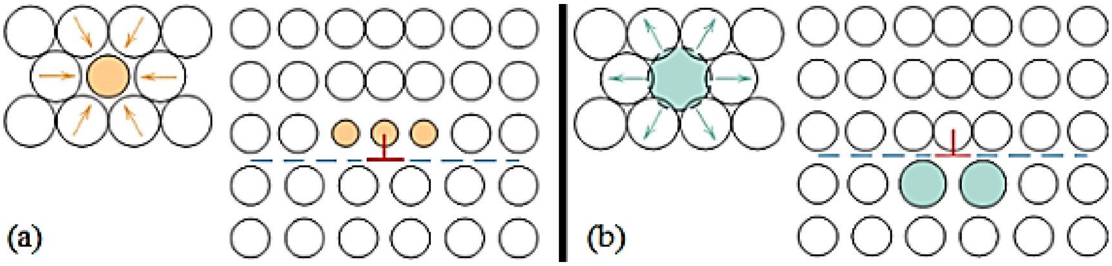

Figure 2.2: Sketch showing (a) tensile lattice strain produced by smaller atoms and (b) compressive lattice strain produced by larger solute atoms than the solvent atoms[14].

The shear strength of the material is improved by using solutes of higher shear modulus and this also improves the strength of the material. The dislocation motion is hindered at these stress concentration sites and in the end, this improves the strength of the material. In summary, factors that will directly influence the solid solution strengthening method are: (a) solute atom’s concentration, (b) solute atom’s size, (c) solute atom’s valence, (d) the symmetry of the solute stress field and (d) the shear modulus of the solute atoms.

2.1.2 Work hardening strengthening

Work hardening is the phenomenon of strengthening materials by which a ductile metal becomes harder and stronger as it undergoes plastic deformation [16]. This is when there is dislocation–dislocation interaction and the use of this method to strengthen the material is frequently used in cold working but it equally applies to hot working. This interaction generates stress fields in the material which can impede dislocation motion positively or negatively.

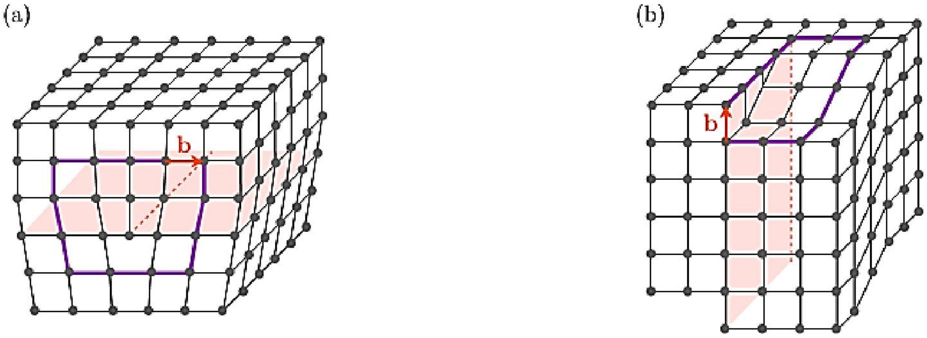

Figure 2.3: Schematic representation of (a) edge and (b) screw dislocations in a simple cubic crystalline material, where filled circles denote the lattice points of a crystal, b is a Burgers vector, hatched area and dashed line illustrate the slip plane and dislocation line, respectively[17].

There are two types of dislocations as shown in Figure 2.3 which are edge dislocations which move in response to a shear stress applied in a direction perpendicular to its line and screw dislocations which lies parallel to its Burgers vector [18]. The movement of the screw dislocation from one slip plane to another takes place by the process known as cross-slip [13]. In an edge dislocation, localized lattice distortions exist along the end of an extra half-plane of atoms whereas for screw dislocations it results from shear distortion. Most of the dislocations in crystalline materials have both edge and screw dislocation components being present at the same time.

When dislocations intersect, jogs and kinks form as depicted in Figure 2.4 and Figure 2.5. Jogs are steps in the dislocation line onto another slip plane while kinks which are steps in the dislocation line in the slip plane.

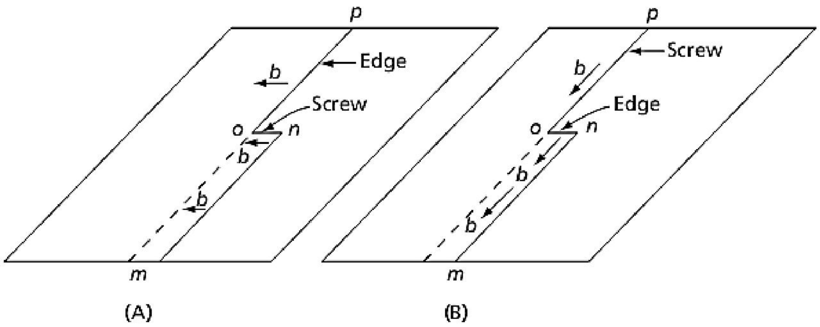

Figure 2.4: Dislocations with kinks that lie in the slip plane of the dislocations[18].

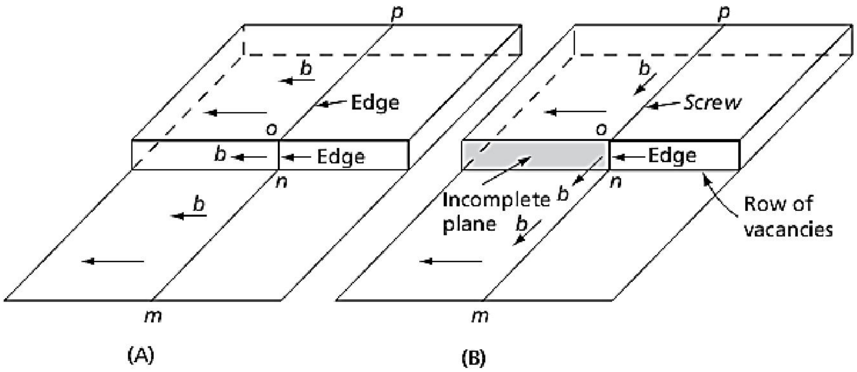

Figure 2.5: Dislocations with jogs normal to their slip planes [18].

There are two basic types of dislocation movement which are glide or conservative motion and climb. Glide is when the dislocation moves in the plane that contains both its line and Burgers vector. When a dislocation is able to move in this manner it is known as glissile and when it cannot it is known as sessile. Climb or non-conservative motion occurs when the dislocation moves out of the glide plane, and thus normal to the Burgers vector [18]. Since vacancy diffusion is a thermally activated process, dislocation climb becomes an important process only at elevated temperatures [13].

The strengthening of any metal or alloy primarily takes place through some form of “interference” with the free movement of the gliding dislocations [15]. Equation [2-2] can be used to describe the effect of dislocations on the increase in shear stresses where ρ is the dislocation density. Before work hardening, the material is usually soaked for some time to produce a regular, relatively “defect–free” pattern. As the material is being strained, dislocations are generated until the material is saturated with dislocations. When it is saturated, these dislocations interact with other dislocations with some annihilation taking place and thereby prevent extra dislocations from nucleating by a balance or steady state being achieved. Therefore, work hardening results from a dramatic increase in the number of dislocation–dislocation interactions, which reduces dislocation mobility. As a result, larger stresses must be applied in order that additional deformation may take place. This increase in stresses required to move the dislocation is what translates into an increase in the strength of the material[15].

$$\Delta\tau \propto Gb\rho^{1/2} \qquad [2\text{-}2]$$

This equation predicts that the flow stress of a metal being plastically deformed will increase as the dislocation density increases, i.e. work hardening takes place [15]. It has been highlighted [13] that if work hardening is to be used as a method of improving the strength of the material, it is important to consider the temperature at which deformation is to take place. A material that contains retained strain (characteristic of DRV and SRV) has a very high dislocation density which remains stable only when the combination of stored strain energy (related to the dislocation substructure) and thermal energy (determined by the deformation temperature) is below a certain level. If not, the microstructure becomes unstable and new strain–free equiaxed grains are formed by recrystallisation (DRX, SRX or MDRX) with the formed new grains that have a much lower dislocation density. Factors that influence work hardening are: (a) the stacking fault energy of the matrix and (b) the stability of the matrix. Hence, face centred cubic metals exhibit higher work hardening rates than body centred cubic metals because of the more stable dislocation interactions, particularly from extended dislocations which contain stacking faults between the two partial dislocations which are possible in the face centred cubic structure [19].

2.1.3 Grain boundary strengthening

Grain boundaries are one of the examples of planar defects; it separates regions of different crystalline orientation that occur when the crystalline structure of the material is discontinuous across a region of disorder. Some examples of planar defects are free surfaces, stacking faults, twins, and phase boundaries [20]. The presence of grain boundaries has an additional effect on the deformation behaviour of a material by serving as an effective barrier to the movement of glide dislocations. From the work of Petch and Hall the yield strength of a polycrystalline material is given by[13]:

$$\sigma_{ys} = \sigma_i + k_y d^{-1/2} \qquad [2\text{-}3]$$

where σ_{ys} is the yield stress, σ_i is the overall resistance of lattice to dislocation movement, k_y is the locking parameter which measures the relative hardening contribution of grain boundaries also known as the Hall–Petch constant and d is the grain size. Equation [2-3] is further reformulated in terms of shear stress and becomes[13]:

$$\tau = \tau_i + k_y d^{-1/2} \qquad [2\text{-}4]$$

where τ is the applied shear stress and τ_i is the frictional shear stress associated with the intrinsic lattice resistance to dislocation motion. It can be seen from equation [2-3] or equation [2-4] that the grain size has an inverse effect on the stresses. The smaller the grain size the higher the strengthening effect. More also, if the number of grains per unit area (i.e. a small grain size) is high , there will be more grain boundaries per unit area and this will lead to more difficulty for dislocations to move as these grain boundaries act as barriers for dislocations. This explains why in alloys with fine grains there is rapid dislocation accumulation which results in DRX being initiated at a lower strain because the critical driving force for the nucleation of a new grain is easily attained [5]. All steel alloys contain at least some carbon which, by combining with other alloying elements, produces a network of fine, stable carbide particles. The carbide network, if made up from small enough but also numerous particles, interferes with the dislocation movement and prevents grain boundary sliding at high temperatures [20].

2.2 Effects of alloying elements

The overall final effect of an alloying element on steel depends on the effects of other alloying elements as they cannot just be added algebraically. For example almost all of the alloying elements impede the growth of austenite grains and almost all of the alloying elements in solid solution reduce the M_s and M_f temperaturesThe only notable exception is manganese, which has the tendency to have an additional effect on the growth of grains [2]. The strongest grain growth retardants are V, Ti, Al, Zr, W, Mo, and Cr; Ni and Si produce a weaker retarding effect[2]. The main cause of this retarding effect is believed to be the formation of low–soluble carbides, nitrides, and other phases, which may serve as barriers for the growth of austenite grains but also from so-called solute drag by solute atoms. Such active carbide–forming elements as Ti, Zr, and V impede grain growth more strongly than Cr, W, and Mo do. This is because the carbides of the former elements are more stable and less soluble in austenite [2].

2.2.1 Carbon

The amount of carbon (C) required in the finished steel limits the type of steel that can be made. Steels can also be classified according to carbon content and there are basically three classes in this regard namely: low, medium and high carbon steels. Carbon has a moderate tendency for macrosegregation during solidification, and it is often more significant than that of any other alloying elements. It has a strong tendency to segregate to the defects in steels (such as grain boundaries and dislocations). Carbide forming elements may interact with carbon and form alloy carbides. Carbon is the main hardening element in all steels except the precipitation hardening (PH) stainless steels, maraging steels, and interstitial–free (IF) steels. The strengthening effect of carbon in steels consists of solid solution strengthening and carbide dispersion strengthening. As the carbon content in steel increases, strength increases, but ductility and weldability decrease [2]. A comparative study of the two 304 stainless steels [21] showed no significant effect of the carbon content on the conditions for the onset of dynamic recrystallisation or on dynamic recrystallisation kinetics.

2.2.2 Manganese

Manganese (Mn) is one of the common alloying elements of steel with 2.0% as the maximum amount to be added to austenitic stainless steel and it was introduced in austenitic stainless steels as a substitute for nickel during shortages in the international market. It has a deoxidising and desulphurising effect on steel. The combination of manganese and sulphur prevents the formation of iron sulphides which can cause "hot shortness" in the steel. Mn is beneficial to surface quality in all carbon ranges (with the exception of extremely low–carbon rimmed steels) and reduces the risk of hot shortness. Mn favourably affects the forgeability and weldability. It is a weak carbide former, only dissolving in cementite, and forms alloyed cementite in steels. Manganese promotes the stability of austenite at or near room temperature and improves hot working properties. Manganese increases the solubility of nitrogen and is used to obtain high nitrogen contents in austenitic steels [2]. The addition of manganese delays the precipitation of TiC [22] in carbon microalloyed steels.

2.2.3 Silicon

Silicon (Si) is one of the principal deoxidisers used in steelmaking; therefore, the silicon content also determines the type of steel produced. It is a noncarbide former. If combined with Mn or Mo, silicon may produce greater hardenability of steels. Due to the addition of Si, stress corrosion can be eliminated in Cr–Ni austenitic steels. In heat–treated steels, Si is an important alloying element, and increases hardenability, wear resistance, elastic limit, yield strength and scale resistance in heat–resistant steels. It has been shown that addition of silicon retards both dynamic and static recrystallisation as well as increases the flow stress of austenite. The addition of Si also increases hardenability and solid solution strengthening [2],[23],[24].

2.2.4 Phosphorus

Phosphorus (P) segregates during solidification, but to a lesser extent than C and S. Phosphorus dissolves in ferrite and increases the strength of steels. As the amount of P increases, the ductility and impact toughness of steels decrease, and raises the cold–shortness. In a strong oxidising environment, it causes grain boundary corrosion in austenitic stainless steels after solid solution treatment as a result of its tendency to segregate to grain boundaries. Phosphorus tends to delay the initiation of dynamic recrystallisation [2],[8].

2.2.5 Sulphur

Increased amounts of sulphur (S) can cause red or hot shortness, unless sufficient manganese is added, due to the low–melting sulphide eutectics surrounding the grain in reticular fashion. Sulphur has a detrimental effect on transverse ductility, notch impact toughness, weldability, and surface quality. Sulphur has a very strong tendency to segregate to grain boundaries and causes reduction of hot ductility in alloy steels. The formation of the sulphides have a marked delaying effect on dynamic recrystallisation [2],[26].

2.2.6 Aluminium

The addition of aluminium (Al) in steel is usually done to prevent oxidation and it is also used to produce fine grains. It is recommended that the grained structural steel contains up to at least 0.015 % Al to produce the fine grained structure which is responsible for the high strength and ductility properties. Aluminium forms oxides and nitrides with nitrogen which impedes grain boundary rotation and migration and thereby helps to keep the austenitic grain size small. It increases scaling resistance and is therefore often added to heat–resistant steels and alloys. Of all the alloying elements, Al is one of the most effective elements in controlling grain growth prior to quenching. Aluminium has the drawback of a tendency to promote graphitisation [2] in ferritic steels.

2.2.7 Nitrogen

Nitrogen (N) is one of the important elements by expanding the $\gamma -$phase field as it is a strong austenite stabiliser. It can expand and stabilise the austenitic structure, and partly substitute Ni in austenitic steels. If the nitride– forming elements V, Nb, and Ti are added to steels, fine nitrides and carbonitrides will form which also increases the creep life of austenitic stainless steels. Nitrogen can be used as an alloying element in microalloying steels or austenitic stainless steels, causing precipitation or solid solution strengthening. It induces strain aging, quench aging, and blue brittleness in low–carbon steels [2].

2.2.8 Chromium

Chromium (Cr) is a medium strength carbide former which is responsible for sensitisation in most stainless steels. In the low Cr/C ratio range, only alloyed cementite $(Fe,Cr)_3C$ forms but if the Cr/C ratio rises, chromium carbides $(Fe,Cr)_7C_3$ or $(Fe,Cr)_{23}C_6$ or both, are likely to be present in the absence of other stabilising alloys like titanium. It is the withdrawal of this Cr from the areas adjacent to grain boundaries that creates localised Cr-poor areas which corrode preferentially, which is known as sensitisation. Chromium carbides are hard and wear–resistant and increase the edge–holding quality. Complex chromium–iron carbides dissolve slowly into austenite during solution heat treatment; therefore, a longer time at temperature is necessary to allow dissolution to take place before quenching is accomplished. Chromium is the one of the main alloying elements in steels. The addition of Chromium in steels enhances the segregation of impurities, such as P, Sn, Sb, and As to grain boundaries and induces temper embrittlement[2]. It is also added to austenitic steels to increase resistance to oxidation and it has been found that this resistance increases as more chromium is added. This resistance to oxidation is directly related to resistance to corrosion which is due to the formation of a self-repairing passive invisible barrier of chromium oxide (CrO) on the surface of the stainless steel.

2.2.9 Nickel

Nickel (Ni) is one of the main alloying elements for austenitic stainless steels and is a noncarbide forming element but is an austenite–forming element. Austenitic stainless steels contain a minimum of 18 % chromium and 8% nickel. If combined with Cr and Mo, it produces greater hardenability, impact toughness, and fatigue resistance in ferritic steels. Ni dissolving in ferrite improves toughness, decreases the fracture appearance transition temperature $FATT_{50\%}$(°C), even at subzero temperatures. Nickel raises the corrosion resistance of Cr–Ni austenitic stainless steels in nonoxidising acid media [2].

2.2.10 Titanium

Titanium (Ti) is a very strong carbide and nitride former which is also usually added as a sensitisation stabilising alloying element to eliminate intergranular corrosion. The effects of Ti are similar to those of Nb and V, but titanium carbides and nitrides are more stable than those of Nb and V. Titanium increases the creep rupture strength through formation of special nitrides and tends significantly to segregation and banding. Ti is an effective grain growth inhibitor because its nitrides and carbides are quite stable and difficult to dissolve in austenite and pin grain boundaries. It has the same effect as aluminium on grain size and it is used as a grain refiner by precipitation of titanium nitrides and carbides at high temperatures which increases ductility, strength and weldability. If Ti dissolves in austenite, the hardenability of ferritic alloy steels may increase strongly due to the presence of Mn and Cr in the steels. Mn and Cr decrease the stability of Ti carbides in steels. A titanium addition retards recrystallisation, i.e. it pushes the recrystallisation temperature to higher limits as more is added. This is attributed to the dynamic interaction of the precipitation of fine TiC/Ti(CN) particles with the recovery of dislocations as the primary source of the retardation of the recrystallisation in the higher Ti containing steels [2], [27].

2.2.11 Copper

A copper (Cu) addition has a moderate tendency to segregate to the grain boundaries and above 0.30% Cu can cause precipitation hardening in ferritic steels. Nitrogen and copper act similarly in that they expand the $\gamma -$phase field. The presence of copper in ferritic steels increases the hardenability of the parent metal. If Cu is present in appreciable amounts, it is detrimental to hot–working operations [2]. In austenitic stainless steels, a Cu content above 1% results in improved resistance to H_2SO_4 and HCl and stress corrosion [28].

2.2.12 Boron

Boron (B), in very small amounts (0.0005–0.0035%), has a starting effect on the hardenability of ferritic steels due to the strong tendency to segregate to grain boundaries. The segregation of B in steels is a non–equilibrium segregation. It also improves the hardenability effect of other alloying elements. It is used as a very economical substitute for some of the more expensive elements. However, large amounts of B result in brittle, unworkable steels as BN tends to form. It has been reported that boron has a positive effect on the creep properties of austenitic stainless steels. Adding 50 ppm of boron to types 316, 321, and 347 stainless steels increases the mean stress rupture life by a factor of three or increases the stress to failure in 10,000 hours by up to 25% [28]. In other studies done on austenitic stainless steels, both critical stress and critical strain were noticed to decrease as the boron content was increased. The flow curves show a delaying effect on the kinetics of dynamic recrystallisation when increasing the boron content. Such behaviour is attributed to a solute drag effect by boron atoms on the austenitic grain boundaries and also to a solid solution softening effect [2][29][30].

2.2.13 Cobalt

Cobalt (Co) is the only alloying element known to decrease hardenability of ferritic carbon steels, but by the addition of Cr, it increases hardenability of Cr–Mo alloy steels. Cobalt raises the martensitic transformation temperature M_s (℃), and it is a noncarbide former. It inhibits grain growth at high temperatures and significantly improves the retention of tempered and high–temperature strength. It becomes highly radioactive when exposed to the intense radiation of nuclear reactors, and as a result, any stainless steel that is in nuclear service will have a cobalt restriction, usually approximately 0.2% maximum. This problem is emphasised because there is residual cobalt content in the nickel used in producing these steels [2].

2.2.14 Oxygen

The purpose for the introduction of oxygen (O) is to deliberately create a surface oxide layer Cr_2O_3 on the immediate surface of the steel. The oxide layer will act as a corrosion resistant barrier on top of the diffusion formed case. Studies have shown that chromium unites with oxygen to form a very tight transparent layer over the steel surface that prevents rusting by precluding further oxidation. This transparent layer is self-healing when damaged by scratches, wear or denting. Oxygen also promotes the formation of Ti_3Al [31], [32].

CHAPTER 3: SOFTENING MECHANISMS IN STEELS

3.1 Dynamic recrystallisation

Dynamic recrystallisation (DRX) is one of the important restoration mechanisms during hot deformation of austenite affecting the final microstructure and, therefore, the mechanical properties of the deformed material. During DRX, the grain boundaries of the material are continuously reconstructed and rearranged as they undergo simultaneous annealing and deformation at high temperatures. It is being said that the descriptive model for DRX is that during deformation, the pre–existing grain boundaries elongate along the deformation direction, grain boundary serrations appear and then new DRX grains nucleate at the serrated parts of grain boundaries (i.e. bulging by the Strain Induced Boundary Migration or SIBM mechanism as the most probable nucleating mechanism) [7]. Dynamic recrystallisation is also sometimes referred to as dynamic softening simply because the microstructure changes during hot deformation and the hardness of the material is lowered. When a metal undergoes microstructural changes after deformation at high temperatures, the phenomenon is called static recrystallisation (SRX). In dynamic recrystallisation as opposed to static recrystallisation, the nucleation and growth of new grains occur during deformation rather than afterwards as part of a separate heat treatment [6]. Also dynamic recrystallisation has a strong effect on the flow curve, leading to much lower stresses at high strains and temperature than dynamic recovery. It is this lowering of stresses that can translate into low strength of the material, i.e. lower mean flow stresses in the mill.

3.2 Initiation of DRX

In a constant strain rate hot isothermal deformation test, dynamic recrystallisation is characterised by the presence of stress peaks in flow stress curve profiles such as the one shown in Figure 3.1. The peak in the $\sigma - \varepsilon$ curve is the major indicator for the occurrence of DRX, but it has been confirmed that dynamic recrystallisation begins before this peak point. There is, therefore, a critical threshold for DRX of stress σ_c, and strain ε_c, which are usually smaller than the peak stress σ_p, and strain ε_p, which represent the true onset of DRX [25]. The flow stress continues to rise in value from this critical point as the strain is increased until the softening due to the progress of DRX is balanced by the continuing strain hardening in the unrecrystallised parts of the material. This balance is manifested by the peak stress σ_p which is found at a corresponding peak strain ε_p which is then followed by work softening until the steady state is reached. The end of work softening is considered to be completion of the first wave of recrystallization which proceeds by nucleation of “necklaces” of new grains until the initial grains have been consumed [33] after which the strain independent steady state flow stress σ_s is reached. The onset of this steady stress is attained at strain ε_s and this zone reflects the balance in the rates on strain hardening and restoration[34].

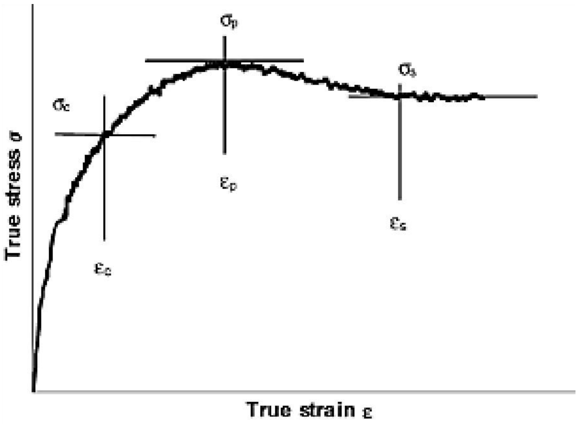

Figure 3.1: A typical stress–strain curve extracted from hot isothermal deformation tests[34]

Deferent models have been used to determine σ_c and ε_c [8], [25], [34–40] and mostly the following relationships are used:

$$\varepsilon_c = a\varepsilon_p \qquad [3\text{-}1]$$

$$\sigma_c = b\sigma_p \qquad [3\text{-}2]$$

where a and b are constants which may be obtained as explained in the next section whereas the relationship between the two is not as simplistic as it appears but it is sufficient that this is a good approximation. The strain to peak ε_p is usually greater than the strain for the initiation of DRX ε_c. Because of this complexity, the reported values of a differ from one study to another. Some of the reported values of a are 0.83, 0.86, and 0.67 [41]. It will be seen later that equation [3-1] can be used after generating the graphs in order to find ε_c with ε_p easily approximated from the graphs and once ε_c is found, σ_c can be read off from the graph at the location of ε_c. The values of a and b are found as averages of the ratios from the corresponding points in the graph. Some of the materials do not exhibit the trend as depicted in Figure 3.1 and there are some alternative methods that are used to characterise them [25], [34], [35].

3.2.1 How to find the critical stress σ_c

Poliak and Jonas [34][42] devised a method based on the thermodynamics of irreversible processes to predict the onset of dynamic recrystallisation where the initiation of dynamic DRX is governed by both the kinetic and energetic critical conditions. The onset of DRX then corresponds to a local maximum in the stored energy attained as a result of substructural evolution under the conditions of deformation. In order to find these critical points on the graph, the stress flow curves are first redrawn starting from the apparent 2% offset yield strength up to about the onset of steady state as shown in Figure 3.2. The extracted curve is then approximated by an n^{th} – order polynomial as shown because it is very difficult to differentiate the original curve because of the "noise" in the recorded data. This polynomial is then differentiated in order to get θ which is the work hardening rate, i.e. $\theta = \frac{d\sigma}{d\varepsilon}$. The differentiated results are then plotted against the flow stress σ as shown in Figure 3.3(a).

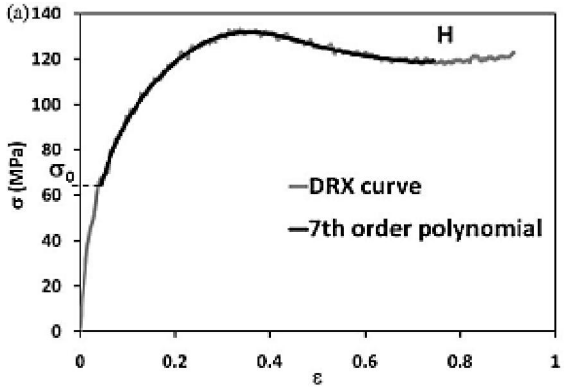

Figure 3.2: The true stress σ versus true strain ε curve indicated by line H and the 9th order approximated polynomial curve superimposed (in bold line). There is less difference between the approximated and the actual flow curves if higher order polynomials are considered [40].

Since this is numerical differentiation from the generated analog data, θ is calculated as follows:

$$\theta_i = \frac{\sigma_{i+1} - \sigma_{i-1}}{\varepsilon_{i+1} - \varepsilon_{i-1}} \qquad [3\text{-}3]$$

3.2.2 *How to find the critical strain ε_c*

To find the critical strain values, a similar procedure is followed where lnθ is plotted against strain values as shown in Figure 3.3(b) and the point of inflection of this curve indicates the location of ε_c. In order to generate this plot, the data is taken from the same $\theta - \sigma$ curves but truncated at the peak because the area of interest is before the peak (critical stress and strain). This curve is then differentiated to find the work hardening rate $\theta = \frac{d\sigma}{d\varepsilon}$ just as it is done when approximating the critical condition for stress.

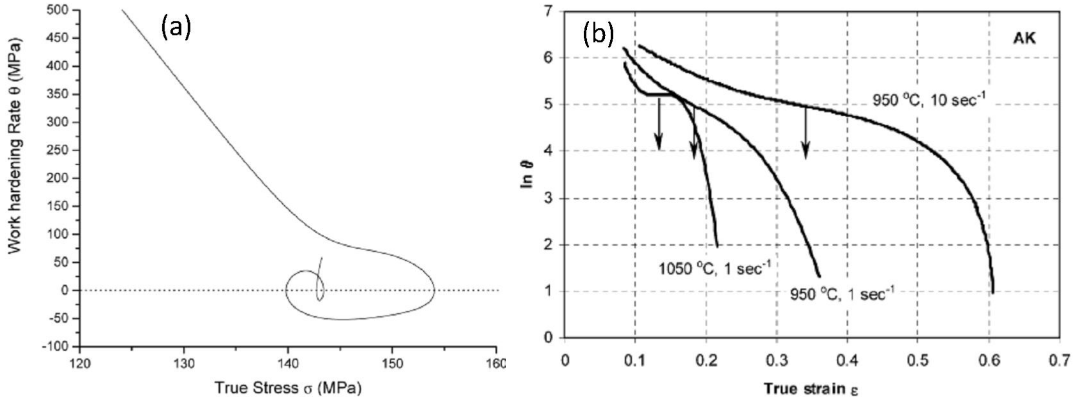

Figure 3.3: Stain hardening rate plots indicating (a) how to find the critical stresses and (b) how to find the critical strain values [25], [34].

Figure 3.3(a) has three important stages. The first stage is where one can clearly see the slanting line which indicates that the work hardening rate decreases rapidly with increasing stress due to dynamic recovery in the actual building up process to the initiation of a second stage. The second stage starts from the point of inflection and this is the point where DRX is considered to start. This second stage crosses the zero line first time, indicating the peak stress σ_p and peak strain and ends when it crosses the zero line for the second time. When it crosses the zero line the second time, the value read off indicates the onset of steady state deformation. Figure 3.3(b) depicts how to identify the critical strain ε_c for the initiation of DRX and is identified by the inflection point.

3.2.3 *How to find the relationship between σ_c, σ_p and $\varepsilon_c, \varepsilon_p$*

The values of σ_c and ε_c that are obtained through the above outlined procedure are then plotted against the Z parameter as shown in Figure 3.4 as well as their corresponding σ_p and ε_p values where their ratios can then be obtained as outlined in equations [3-1] and [3-2].

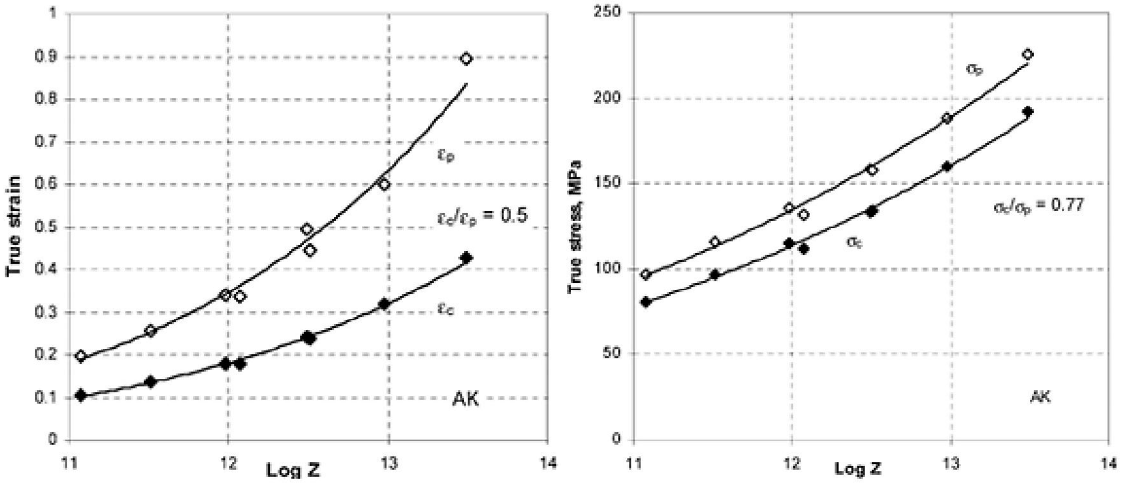

Figure 3.4: **Plots indicating how to find the critical stress σ_c and the critical strain ε_c** [34].

3.3 Dynamic Recovery

It was mentioned earlier that there are two mechanisms responsible for restoration in hot working which depend on the material under study. The first one is dynamic recrystallisation as discussed in §3.1 and the second one is dynamic recovery. In some materials with moderate to high stacking fault energy like aluminium, dynamic recovery is predominant, and the material does not exhibit the flow stress profile characteristic of dynamic recrystallisation at all. Figure 3.5 shows the plot of the characteristic flow stress profiles for (a) dynamic recovery and (b) dynamic recrystallisation. It can be seen that if the material is undergoing dynamic recovery, there is no peak but the flow stress profile rises to a plateau followed by steady state deformation.

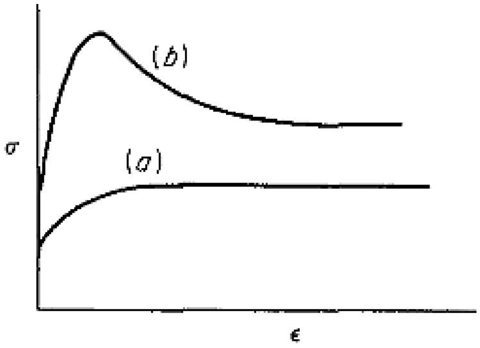

Figure 3.5: **The plots show (a) hot–working stress–strain curve for a metal which shows dynamic recovery; (b) metal which undergoes dynamic recrystallisation after initial period of dynamic recovery**[43]**.**

If the material is undergoing dynamic recovery, there is an accumulation of dislocations due to the generation of new dislocations and dislocation multiplication. Dynamic recrystallisation only sets in if the critical conditions are reached and DRX is characterised by the annihilation of the dislocations through the formation of the new “dislocation-free” nuclei. What happens before recrystallisation is that elimination of point defects and diffusion assisted reorganisation of dislocations occurs and subgrains are formed [44].

If the material is undergoing only dynamic recovery, the accumulated dislocations remain (although in a re-arranged form) and this results in retained strain in the material and because of this retained strain the material does not experience a decrease in strength. The basic deformation mechanisms of dynamic recovery are dislocation climb, cross–slip and glide. During this period of dynamic recovery, the microstructure of low angle boundaries and subgrains develops [6].This process of strengthening is known as strain hardening or work hardening and will be explained later. DRV is a process which is a function of deformation temperature, strain and strain rate which can be manifested by an elongated and pancaked grain structure. In aluminium and alpha iron dynamic recovery is the only known softening mechanism. This occurs by the formation of a well-developed subgrain structure by cross slip and climb, as occurs in creep deformation. The activation energy for hot working should naturally be equal to that for creep and for self–diffusion. In metals with a lower stacking fault energy (copper, nickel, and austenitic stainless steel), the activation energy for softening in hot work is higher than for creep [43]. DRV and DRX compete as both are driven by the stored energy.

3.4 Constitutive governing equations

The following expressions are some of the many empirical equations commonly used in the literature for modelling hot working characteristics:

$$Z = \dot{\varepsilon} e^{\frac{Q}{RT_d}} = Af(\sigma) \qquad [3\text{-}4]$$

$$\varepsilon_p = A_1 d_o^m Z^q \qquad [3\text{-}5]$$

where Z is the Zener–Hollomon parameter also known as the temperature compensated strain rate, $\dot{\varepsilon}$ is the strain rate which also represents the rate/speed of deformation, Q is the activation energy of deformation, R is the universal gas constant which is normally taken as

$8.314\, Jmol^{-1}K^{-1}$, T_d is the absolute deformation temperature (in Kelvin), $A_1, m\ , q$ are material constants, d_o is the initial grain size, ε_p is the peak strain which is obtained (read off) directly from the flow stress–strain graphs, A is the material structural factor which depends on the initial austenite grain size and chemical composition of the material [45] and $f(\sigma)$, is the stress function which has the following three forms [46]:

$$Z = \dot{\varepsilon} e^{\frac{Q}{RT_d}} = A\sigma_p^{n'} \qquad [3\text{-}6]$$

$$Z = \dot{\varepsilon} e^{\frac{Q}{RT_d}} = A_2 e^{\beta\sigma_0} \qquad [3\text{-}7]$$

$$Z = \dot{\varepsilon} e^{\frac{Q}{RT_d}} = A_3\left[\sinh(\ \alpha\sigma_p)\right]^n \qquad [3\text{-}8]$$

where β is a constant, $\alpha$is a material constant and can be calculated from $= \beta/\acute{n}$, σ_p is the peak flow stress which is obtained (read off) directly from the flow stress–strain graphs and n is the stress sensitivity constant. σ_{ss}, which is the steady state flow stress, is used instead of σ_p as this makes the Z value independent of strain. Generally, equation [3-6] is used for low stress calculations while equation [3-7] is used for high stress calculations. The sinh–hyperbolic equation [3-8] was proposed by Sellars and Tegart [47] to cover both stress regimes. When $\alpha\sigma \leq 0.8$, the hot working is considered to be in the low stress regime while when $\alpha\sigma \geq 1.2$, the high stress regime is assumed. The activation energy is taken as a constant throughout the calculations as no change in the dislocation glide mechanism is suspected.

Equation [3-5] suggests that the peak strain is a function of deformation temperature, strain rate and structure of the material which includes the initial grain size. In the literature[48][49], it is highlighted that the peak strain depends on other additional variables apart from deformation temperature, strain rate and structure of the material. These variables include chemical composition, reheat temperature and dislocation accumulation. One of the alloying elements in steel that can be singled out and that contributes to the rise of peak strain when it is added, is titanium (others are niobium and vanadium). Titanium is mentioned because in 321 steel it is added for stabilisation purposes and possibly for grain refinement and no titanium is present in 304 steel. This means that 321 is expected to have higher peak strains as compared to 304 steel. Reheat temperature goes hand-in-hand with the austenite grain size because the reheat temperature affects the initial grain size. On the other hand, the effect of deformation temperature and strain rate can be seen through the Zener–Hollomon parameter. The higher the strain rate, the higher the Z parameter which implies higher peak strain and the reverse is also true. Also, the lower the deformation temperature, the higher the Z parameter; hence the peak strain will be higher.

Taking natural logarithms on both sides of equation [3-6] and using partial differentiation, one obtains the following relationship assuming a constant deformation temperature:

$$\ln \dot{\varepsilon} + \frac{Q}{RT_d} = \ln A_1 + n' \ln \sigma_p \qquad [3\text{-}9]$$

$$n' = \frac{\partial \ln \dot{\varepsilon}}{\partial \ln \sigma_p} \tag{3-10}$$

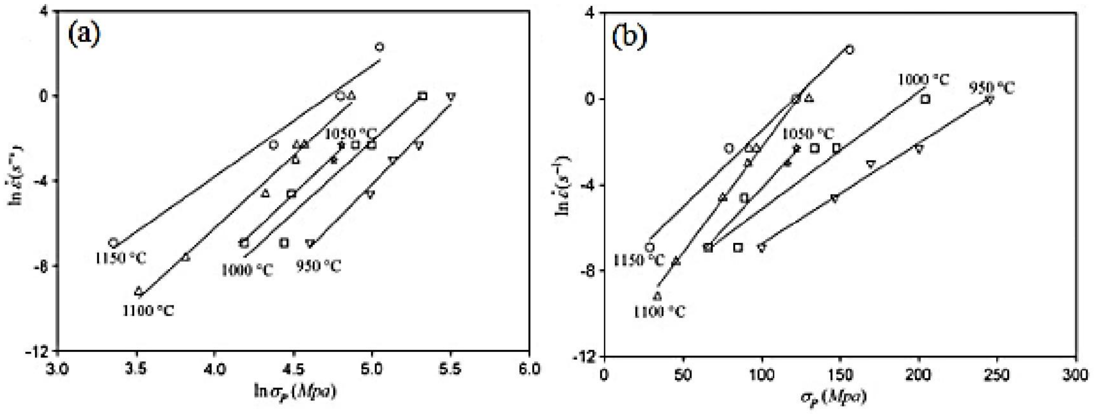

Figure 3.6: **Plots of $\boldsymbol{ln\dot{\varepsilon}\ vs\ ln\sigma_p}$ and $\boldsymbol{ln\dot{\varepsilon}\ vs\ \sigma_p}$ used for the calculation of constants (a) $\boldsymbol{n'}$ and (b) $\boldsymbol{\beta}$ from the power law respectively** [50]

The plots of $ln\dot{\varepsilon}\ vs\ ln\sigma_p$ are shown in Figure 3.6(a), the slope of which gives the value for ń and taking natural logarithms on both sides of equation [3-7] and using partial differentiation, one obtains the following relationship:

$$\ln \dot{\varepsilon} + \frac{Q}{RT_d} = \ln A_2 + \beta \sigma_p \tag{3-11}$$

Assuming constant temperature, the equation simplifies to:

$$\beta = \frac{\partial \ln \dot{\varepsilon}}{\sigma_p} \tag{3-12}$$

A plot of $ln\dot{\varepsilon}\ vs\ \sigma_p$ is shown in Figure 3.6(b) of which the slope provides the value of β.

Equation [3-6] can be rewritten as follows:

$$Z = \dot{\varepsilon} e^{\frac{Q}{RT_d}} \tag{3-13}$$

$$\dot{\varepsilon} = A\left[\sinh\left(\alpha \sigma_p\right)\right]^n e^{\frac{-Q}{RT_d}} \tag{3-14}$$

Taking natural logarithms of equations [3-13] and [3-14] provide:

$$\ln Z = \ln \dot{\varepsilon} + \frac{Q}{RT_d} \tag{3-15}$$

$$\ln \dot{\varepsilon} = \ln A + n \ln\left[\sinh\left(\alpha \sigma_p\right)\right] - \frac{Q}{RT_d} \tag{3-16}$$

If one uses partial differentiation on equation [3-16] and assuming a constant temperature, one obtains:

$$n = \frac{\partial \ln \dot{\varepsilon}}{\partial\left\{\ln\left[\sinh\left(\alpha \sigma_p\right)\right]\right\}} \tag{3-17}$$

If temperature and strain are kept constant, the plot of $ln\dot{\varepsilon}\ vs\ ln\left[sinh\left(\alpha\sigma_p\right)\right]$ gives straight lines of which the slope provides the stress exponent n and the plot of this relationship at various temperatures is shown in Figure 3.7(a).

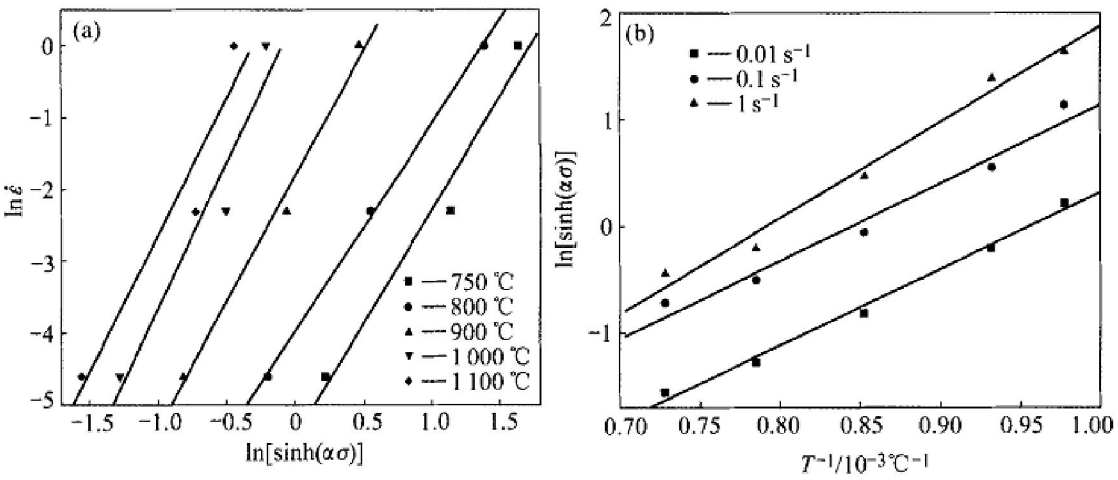

Figure 3.7: Plots of $\ln\dot{\varepsilon}$ vs ln[sinh$\alpha\sigma$] and ln[sinh$\alpha\sigma$] vs $1/T$ used for the calculation of constants (a) n (b) Q from the hyperbolic law [51]

If the strain rate is assumed to be constant but the temperature is varied, equation [3-16] can be simplified into:

$$Q = nR\frac{\partial\left\{\ln[\sinh(\alpha\sigma_p)]\right\}}{\partial(1/T_d)} \qquad [3\text{-}18]$$

If the strain rate is kept constant, the plot of $ln\left[sinh\left(\alpha\sigma_p\right)vs\ \ 1/T\right]$ gives straight lines of which the slope is Q/nR and the plot of this relationship at various temperatures is shown in Figure 3.7(b). Substituting n into this relationship that has been obtained from Figure 3.7(a), the value of the activation Q can be found.

3.5 Nucleation and growth kinetics

As mentioned earlier, dynamic recovery occurs at all temperatures and strain rates and in most cases up to the critical values of strain and the applied stress. Until the material is strained to certain critical values, nucleation of new grains occurs at the margins of existing grains by local grain boundary bulging through SIBM [52]. Therefore dynamic recovery is taken as the precursor for the nucleation of dynamically recrystallised grains if DRX is to take place. It is predominant at high strain rates and low deformation temperatures while dynamic recrystallisation is dominant at low strain rates and high deformation temperatures.

The evolution of a dynamically recrystallised microstructure based on the necklace structure has been suggested to be the most likely DRX mechanism that takes place during hot deformation [6], [7], [47], [53], [54]. Figure 3.8 depicts schematically the microstructure evolution that takes place during dynamic recrystallisation where the new grain nucleates on the prior grain boundaries as shown in Figure 3.8(a) through what is known as the SIBM nucleation mechanism (originally conceived by Bailey–Hirsch[6]. The formed new grains stop to grow at the characteristic size, allowing new necklaces of same–size grains to form [55]. The process continues as deformation progresses as shown in Figure 3.8(b–d) until new grains develop fully as depicted in Figure 3.8(e)

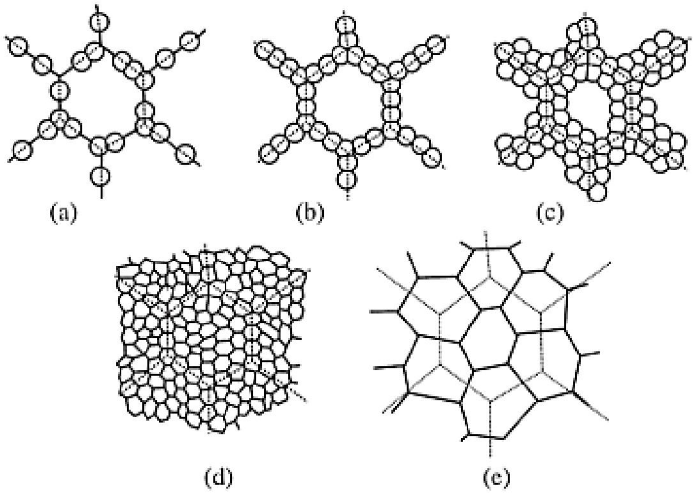

Figure 3.8: Schematic representation used to describe the microstructure evolution during dynamic recrystallisation. (a)–(d) Large initial grain size, (e) small initial grain size where the dotted lines show the prior grain boundaries[6]**.**

Unlike in other restoration mechanisms, the overall steady state mean grain size of a dynamically recrystallised material remains fairly constant as depicted in Figure 3.8(d).

In general the nucleation of new grains takes place on preferred sites such as prior grain boundaries (as shown in Figure 3.8) or at transition bands and shear bands or second–phase particles, or may be on inhomogeneities induced by the deformation or transition band or at (oxide) inclusions. As for dynamic recrystallisation, nucleation originates at high angle boundaries as they are more mobile. These may be the original grain boundaries, boundaries of dynamically recrystallised grains, or high angle boundaries created during straining (e.g. those associated with deformation bands or deformation twins). Bulging of grain boundaries is frequently observed as a prelude to dynamic recrystallisation, and it is usually assumed that a mechanism closely related to strain–induced grain boundary migration (SIBM) operates. If nucleation only occurs at grain boundaries, then a given number of nuclei in a fine–grained material will lead to more homogeneous recrystallisation than the same number in a coarse grained material [6]. Recrystallisation is a microstructural transformation, which is most directly measured by quantitative metallography. However, it is also possible to follow the progress of recrystallisation by the measurement of various physical or mechanical properties. The progress of recrystallisation with time during isothermal annealing is commonly represented by a plot of the volume fraction of material recrystallised, as a function of log(time), as shown in Figure 3.9.

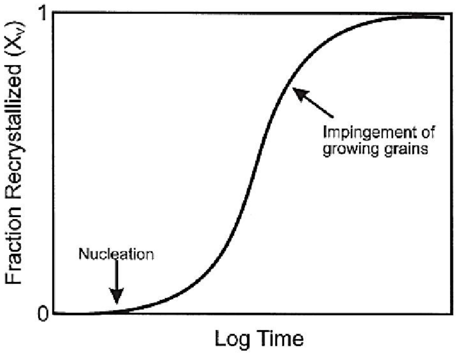

Figure 3.9: Schematic representation of the recrystallisation kinetics [56]**.**

This plot usually has the characteristic sigmoidal form and typically shows an apparent incubation time before recrystallisation is detected. This is followed by an increasing rate of recrystallisation, a linear region, and finally a decreasing rate of recrystallisation. The extent of recrystallisation is often described by the volume fraction X_v, and for isothermal experiments it is convenient to use the time at which recrystallisation is 50% complete $t_{0.5}$, as a measure of the rate of recrystallisation.

The type of curve shown in Figure 3.9 is typical of many transformation reactions and may be described phenomenologically in terms of the constituent nucleation and growth processes. The early work in this area is due to Kolmogorov (1937), Johnson and Mehl (1939) and Avrami (1939) and is commonly known as the JMAK model. A more general discussion of the theory of the kinetics of transformations may be found in the phase transformation literature.

It is assumed that nuclei are formed at a rate $\dot{N}$ and that grains grow into the deformed material at a linear rate $\dot{G}$. If the grains are spherical, their volume varies as the cube of their diameter, and the fraction of recrystallised material (X_v) rises rapidly with time. However, the new grains will eventually impinge on each other and the rate of recrystallisation will then decrease, tending to zero as X_v approaches 1. The number of nuclei (dN) actually appearing in a time interval (dt) is less than $\dot{N}dt$ because nuclei cannot form in those parts of the specimen which have already recrystallised. The number of nuclei which would have appeared in the recrystallised volume is $\dot{N}X_v dt$ and therefore the total number of nuclei (dN') which would have formed, including the 'phantom' nuclei is given by [56]:

$$dN' = \dot{N}dt = dN + \dot{N}X_v dt \qquad [3\text{-}19]$$

In order to define a recrystallisation nucleus it is taken to be a crystallite of low internal energy growing into deformed or recovered material from which it is separated by a high angle grain boundary. If the number of nuclei per unit volume (N_v) remains constant during recrystallisation, then this is the key parameter. However, if this is not the case, the nucleation rate $\dot{N} = dN/dt$ also needs to be considered.

The growth of the new grains during recrystallisation is more readily analysed than is their nucleation. It is generally accepted that the velocity (v) of a high angle grain boundary, which is also the growth rate (G) is given by [56]:

$$v = \dot{G} = MP \qquad [3\text{-}20]$$

where M is the boundary mobility and P is the net thermodynamic pressure on the boundary. The driving pressure (P_d) for recrystallisation is provided by the dislocation density (ρ), which results in a stored energy (E_D). The resultant driving force for recrystallisation is then given approximately as [56]:

$$P_d = E_D = \alpha \rho G b^2 \qquad [3\text{-}21]$$

where α is a constant of the order of 0.5. For a dislocation density of $10^{15} m^{-2}$, typical of a metal, and taking Gb^2 as $10^{-9}\ N$, the driving pressure for primary recrystallisation is of the order of 1 MPa. If the dislocations are in the form of low angle boundaries, then the driving pressure may be expressed in terms of subgrain size and misorientation.

By rearranging together with the necessary assumptions, equation [3-19] can be rewritten by making X_v the subject of the formula as follows:

$$X_v = 1 - \mathrm{e}^{-Bt^n} \qquad [3\text{-}22]$$

where $B = \left(f \dot{N} \dot{G}^3\right)/4$ and f is the shape factor which may be taken as $4\pi/3$ for a spherical nucleus in the JMAK equation. The derivation of equation [3-22] assumed that the rates of nucleation and growth remained constant during recrystallisation. Avrami (1939) also considered the case in which the nucleation rate was not constant but is a decreasing function of time, $\dot{N}$ having a simple power law dependence on time. In this situation, n lies between 3 and 4, depending on the exact form of the function.

The JMAK equation was latter modified by Cahn [57] to take into account the grain boundary nucleation, hence equation [3-22] changes to the following:

$$X_v = 1 - \mathrm{e}^{-\pi/3 \dot{N} S_v \dot{G}^3 t^4} \qquad [3\text{-}23]$$

where S_v is the grain boundary surface area per unit volume and after site saturation, i.e. when it is assumed that all nucleation takes place at the beginning of transformation, equation [3-23] reduces to:

$$X_v = 1 - \mathrm{e}^{-2 S_v \dot{G} t} \qquad [3\text{-}24]$$

An alternative approach is proposed [58] where the time t from the start of the reaction is replaced by $(\varepsilon - \varepsilon_c)$ in the JMAK equation which now changes to equation [3-25]. The plots shown in Figure 3.10 of this modified equation depict that the slopes are not a function of the original grain size. The term $(\varepsilon - \varepsilon_c)$ represents the instantaneous time taken for the progress of dynamic recrystallisation process.

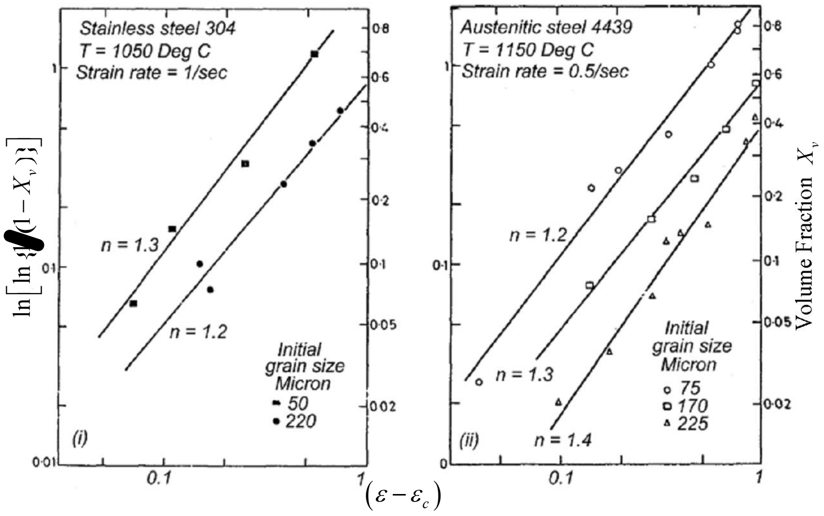

Figure 3.10: **Plots of** $\ln[\ln\{1/(1 - X_v)\}]$ **against** $(\varepsilon - \varepsilon_c)$ **showing an alternative approach to JMAK equation where time** t **is replaced by** $(\varepsilon - \varepsilon_c)$ [58]

$$X_v = 1 - e^{-B(\varepsilon - \varepsilon_c)^n} \tag{3-25}$$

3.6 Friction

Tribological factors affect tool and tool life, metal flow during forming, work–piece integrity and surface finish, the relationship of lubricant to machine elements, cost considerations and energy conservation.

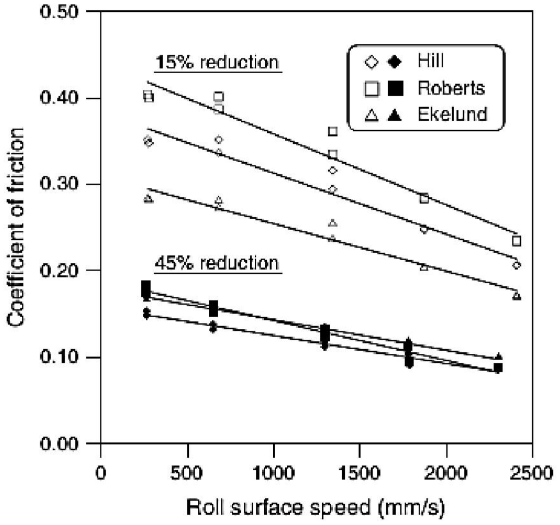

Figure 3.11: **The coefficient of friction, as predicted by Hill's, Roberts' and Ekelund's formulae, for cold rolling of a low carbon steel** [59]

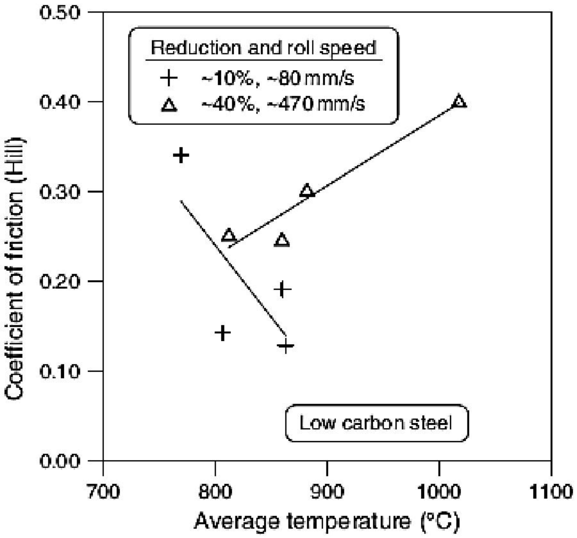

Figure 3.12: **The dependence of Hill's coefficient of friction on the temperature at low speeds and reductions and secondly at high speeds and reductions**[59]

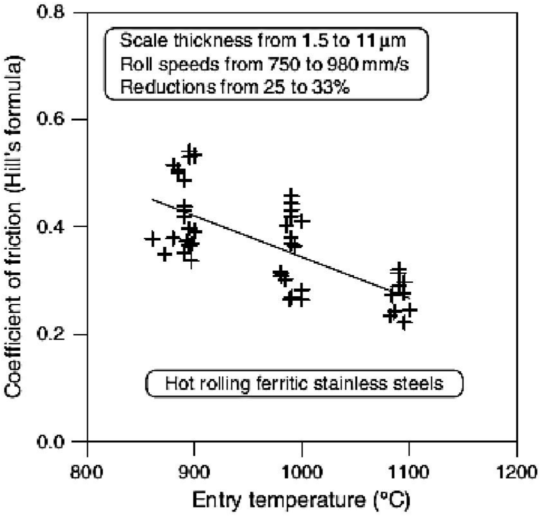

Figure 3.13: **The coefficient of friction as a function of the temperature during hot rolling of ferritic stainless steel strips** [59]

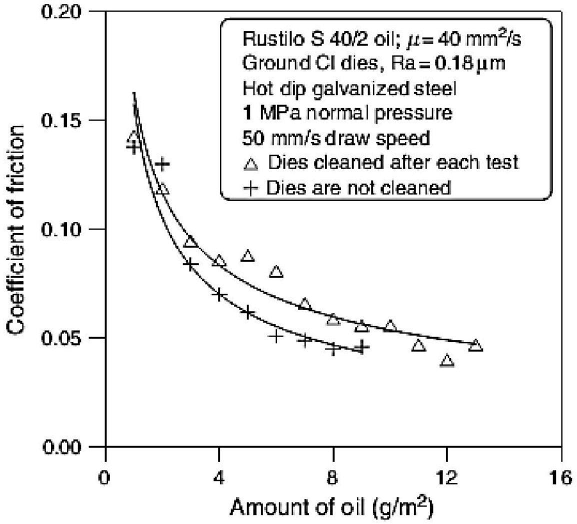

Figure 3.14: **The dependence of the coefficient of friction on the film thickness in the flat-die test** [59]

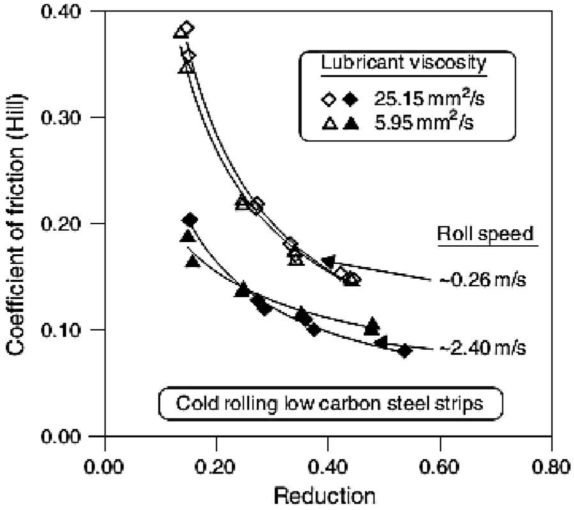

Figure 3.15: **The dependence of the coefficient of friction on the reduction in low carbon steel strips** [59].

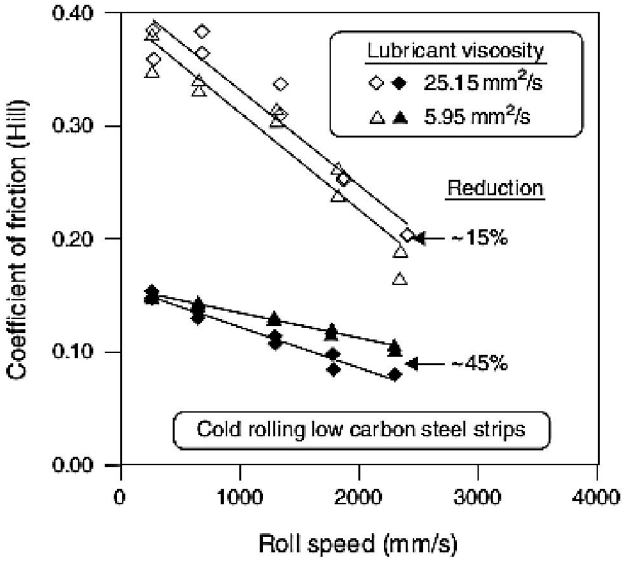

Figure 3.16: **The dependence of the coefficient of friction on the rolling speed in low carbon steel strips** [59].

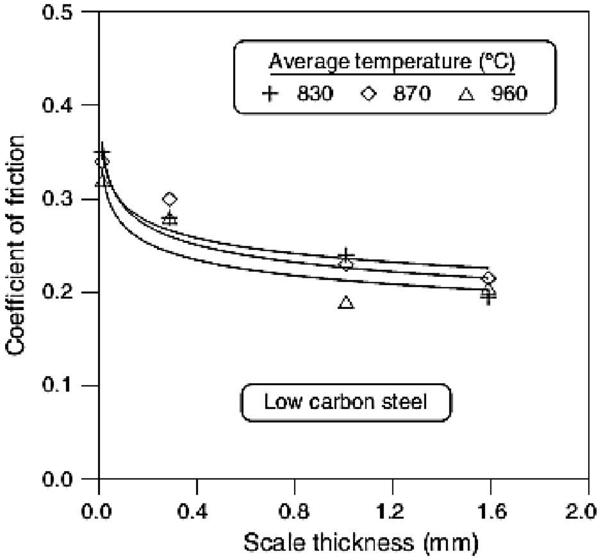

Figure 3.17: **The dependence of the coefficient of friction on the temperature and thickness of the layer of scale** [59].

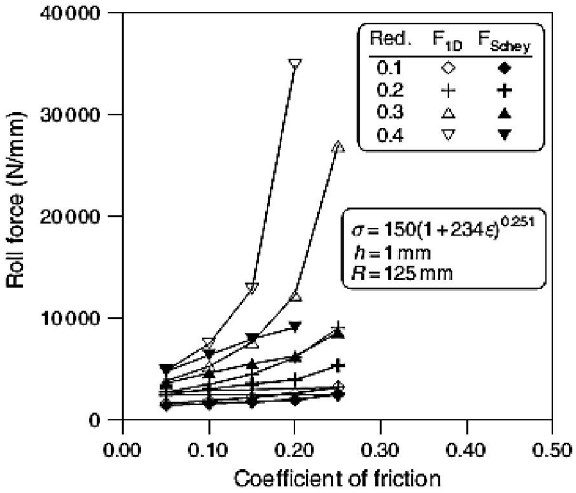

Figure 3.18: **The dependence of the roll separating force on the reduction and the coefficient of friction; the predictions of the empirical model of Schey and that of the refined 1D model are shown** [59].

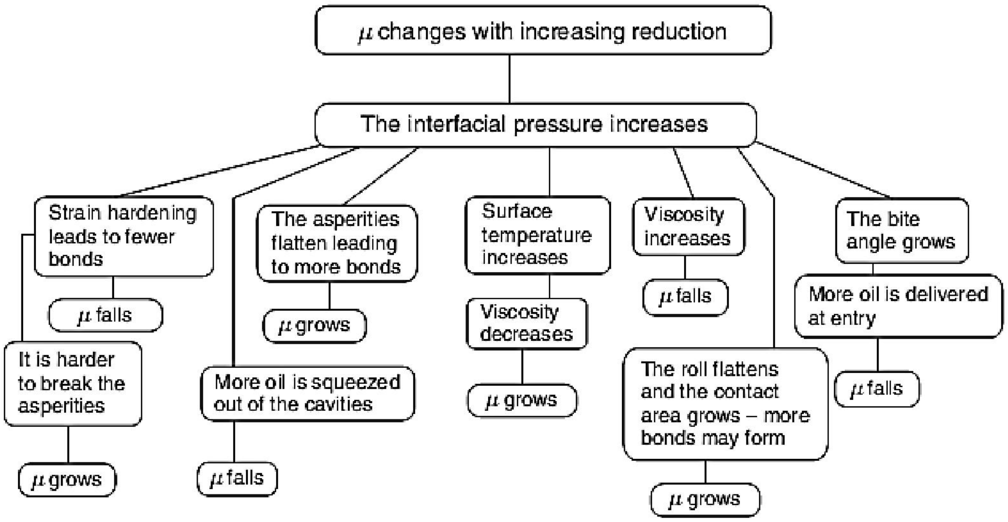

Figure 3.19: **Summary of the effect of increasing reduction on the coefficient of friction** [59].

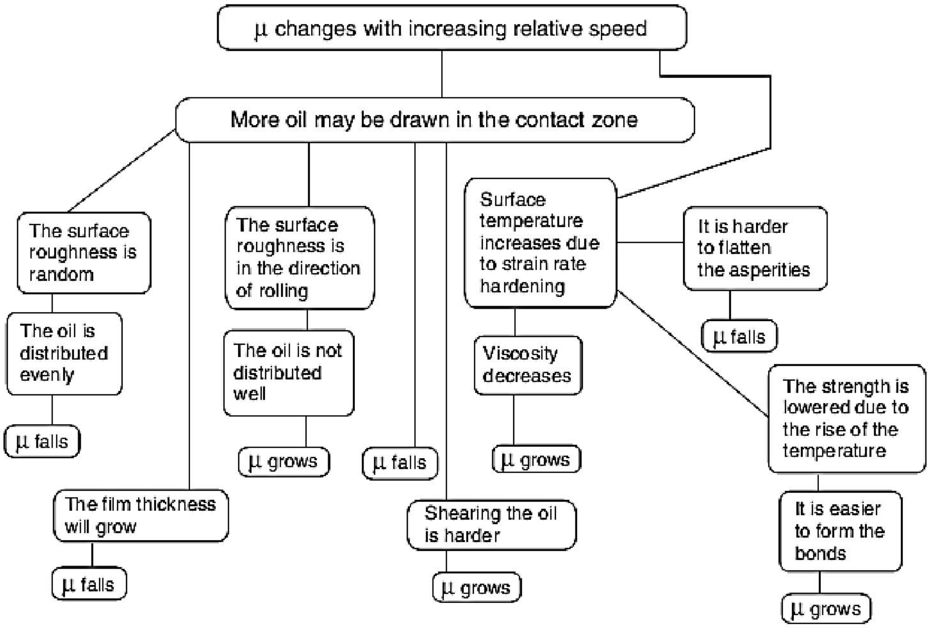

Figure 3.20: Summary of the effect of increasing relative velocity on the coefficient of friction [59].

It is reported [60] that among the various friction models that have been suggested in the literature, the most accurate model is still undefined and controversial. Friction is one of the most important fundamental phenomena that should be taken into account with rolling analysis because there is always relative motion and contact between the tool/roll and the workpiece. Without friction it would be impossible to deform the materials in hot rolling as friction is necessary to “pull the work piece into the roll gap”. The occurrence of friction is, however, complex in nature as highlighted from Figure 3.11 to Figure 3.20 because of the geometry of the contact area and other interrelationships between the parameters involved in deformation such as loading conditions, rolling speed/strain rate (Figure 3.11 Figure 3.16 and Figure 3.20), surface roughness or finish (Figure 3.15 and Figure 3.19), deformation temperature (Figure 3.12, Figure 3.13, Figure 3.13 and Figure 3.17), scale formation (Figure 3.17), lubricant used (Figure 3.14), rolling force (Figure 3.18) and the material being deformed (i.e. its material properties) [51], [61–85]. Figure 3.21 shows the process of deforming a work piece from Figure 3.21(a) to either Figure 3.21(b) which depicts an ideal case where the material is assumed to be deformed in the absence of friction or to Figure 3.21(c) which is more realistic and is invariably encountered during experimental deformation. Friction has the tendency to increase the pressures and forces between the workpiece and the tool and because of this the amount of reduction is also affected. If there was no friction between the circular ends of the workpiece and the platens of the press then the cylindrical specimen would reduce in height while remaining cylindrical in shape. The normal pressure would be constant over the contact circles.

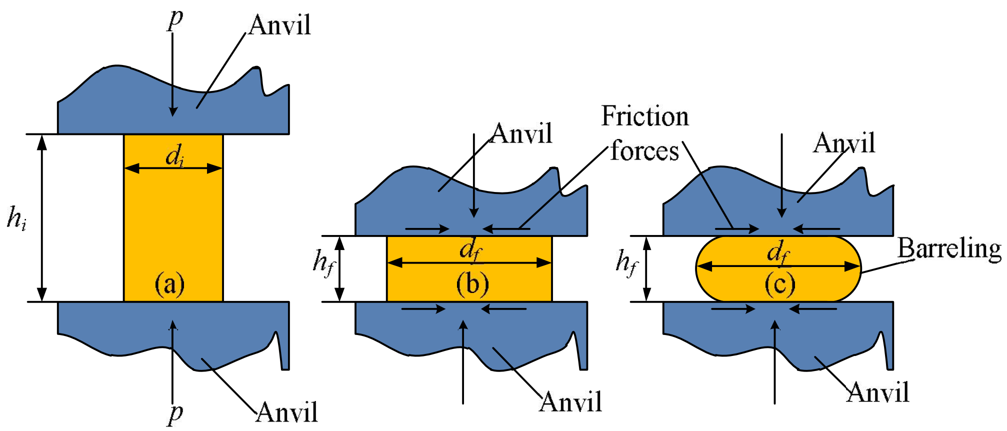

Figure 3.21: Schematic sketch showing a work piece being compressed from (a) initial height h_i to (b) idealised case final height h_f when friction is assumed not to be present or to (c) final height h_f when friction is present. Friction brings about barrelling in the specimen.

In metalworking simulations, deformation analyses are based on work pieces deformed in the laboratory. The hot compression deformation tests in the Gleeble simulators are done on cylindrical specimens that are held between the deformation jaws and the tungsten carbide anvils. Frictional effects are minimised by the use of tantalum foils which are placed between the anvil platens and the workpiece. Measuring friction along the contact area is a tedious task and as a result workers in this field have resorted to the use of a constant value for friction which is generally accepted [62]. The coefficient of friction is taken to be constant based on the assumption that the environment and surface conditions remain constant. The frictional conditions on the top and bottom faces of the specimens and the anvils are approximated by several models. Some of the commonly used ones are:

a. Coulomb friction model

$$\mu = \frac{\tau}{p} \qquad [3\text{-}26]$$

b. Constant friction model

$$m = \frac{\tau\sqrt{3}}{\sigma_o} \qquad [3\text{-}27]$$

c. General friction model [74]

$$f = \frac{\tau}{\alpha k} \qquad [3\text{-}28]$$

d. the Geleji equation [74]

$$\mu = A - BT - Cv \qquad [3\text{-}29]$$

e. the Roberts equation [74]

$$\mu = aT - b \qquad [3\text{-}30]$$

where τ is the shearing stress at the interface and p is the stress normal to the interface, μ is the coefficient of friction, m is the friction factor, f is the friction factor expressing the friction in the real contact area and α is the ratio of the real to the apparent contact area [60]. In equations [3-29] and [3-30], $A, B, C, a,$ and b are constants while T and v are deformation temperature and rolling speed respectively. The last two equations indicate that friction varies with deformation temperature and rolling speed. They somehow contradict each other in that in equation [3-29], it is shown that the higher the temperature the lower the coefficient of friction while in equation [3-30], a higher deformation temperature has a positive effect.

The use of equation [3-27] is gaining more grounds compared to the rest of the models because of the simplicity with which it can be used to calculate m. The value of m is measured from the geometry of the deformed specimens and it is related to the coefficient of friction μ through the following empirical relationship[47]:

$$m = \frac{\frac{R_{av}}{h_f} b}{\frac{4}{\sqrt{3}} - \frac{2b}{3\sqrt{3}}} \qquad [3\text{-}31]$$

where b is the barrelling coefficient and is calculated using the following equation[47]:

$$b = \frac{h_i d_i^2}{h_f d_f^2} \qquad [3\text{-}32]$$

If the calculated barrelling coefficient, $b < 0.9$, the effect of barrelling on the final analysis of the results may be neglected. R_{av} is the average radius of the specimen after deformation which is mainly measured at the centre of the deformed specimen and is given by [68]:

$$R_{av} = R_i \sqrt{\frac{h_i}{h_f}} \qquad [3\text{-}33]$$

m lies between 0, which is the condition for perfect sliding, and 1 which represents the sticking condition. m is relatively easier to find (unlike μ to be measured directly) and once m is calculated, μ can be found from the following relationship[47]:

$$\mu = \frac{m}{\sqrt{3}} \qquad [3\text{-}34]$$

From this relationship, it can be seen that for a perfectly sliding condition μ will also be equal to 0 and that for a sticking condition, the maximum value for μ is 0.5774. This relationship between μ and m can be used for the justification of the use of constant values for the inclusion of coefficient of friction in the friction compensated equations.

The friction hill caused by friction as depicted in Figure 3.22 [43] shows that the distribution of pressure across the workpiece surfaces is not constant, i.e. it is highest at the so-called neutral point where no relative movement between the work piece and the rolls or platens is found and in hot rolling, the position of this neutral point is a function of *inter alia* factors such as the geometry, the presence of front and/or back tension, etc.. When friction is present in a standard compression test, the outward movement of the material in contact with the platens is restricted and as a result the cylinder barrels as depicted in Figure 3.21(c).

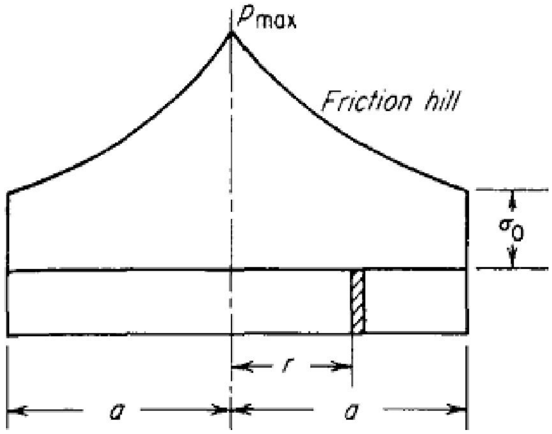

Figure 3.22: **Friction hill for homogeneous compression of a disk with Coulomb friction**[43]

Van Rooyen and Backofen tried to understand the complexity of friction (reported by ref [43]) by using small pressure pins which were buried in the tool under the workpiece. Some of the results as published by Backofen in 1972 are shown in Figure 3.23 for an unlubricated aluminium cylinder that was subjected to compression testing. From this figure, it can be seen that the coefficient of friction varies from the centre to the periphery of the cylinder with perfect sliding at the centre and a sticking condition at the periphery. They proposed the use of smooth, hardened platens, grooving the ends of the specimen to retain lubricant in order to minimise friction at the specimen-platen interface. The complexity of friction in hot compression of cylinders further affects the material flows inside the cylinder as shown in Figure 3.24. This figure shows that there are three zones that are expected which are:

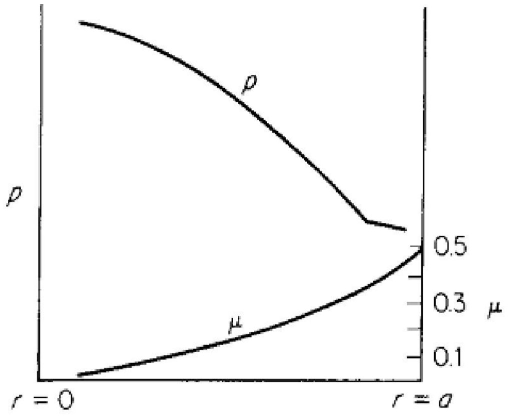

Figure 3.23: **Variation of normal pressure p and coefficient of friction μ with radial distance r from the centre** [43]

a. zone I – this zone is referred to as the dead zone because in this zone, the material is not deformed.
b. zone II – in this zone the material is deformed most and the strain rate is the highest.
c. zone III – in this zone the deformation of the material is moderate.

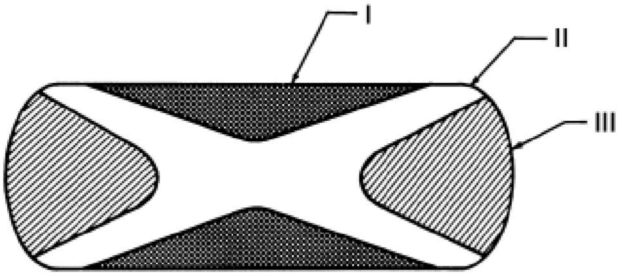

Figure 3.24: **Sketch showing the likely deformation zones of the cylinder after compression** [47]

Observing these three scenarios it is found that due to the complexity of friction, even the strain rate within the material itself is also affected. In the analysis this fact is often neglected and as a result a constant value of strain rate is considered and is, therefore, the representation of an *assumed average value*.

For characterisation of the multi-axes stresses present in the specimen, the data from the Gleeble should be converted to true Von Mises flow stress and true Von Mises strain by using the equation that takes into account the effect of friction between the pressure anvils and the specimen. Von Mises flow stress and strain are the most frequently used invariant functions to describe multi-axial plastic deformation and they are presented as follows [43][86].

$$\sigma_o = \frac{0.0625 P_x \mu^2 h_x^{-2}}{e^{\mu\sqrt{\left(d_i^2 h_i / h_x\right)} / h_x} - \mu\sqrt{\left(d_i^2 h_i / h_x\right)} / h_x - 1} \qquad [3\text{-}35]$$

$$\sigma_o = -0.0981 P_x \frac{\Delta h + h_i}{h_i d_i^2 \left(\pi/4\right)} \qquad [3\text{-}36]$$

where: P_x is the Gleeble force, h_x is the Gleeble stroke, h_i is the initial height of the specimen, d_i is the initial diameter of the specimen, σ_o is the calculated flow stress. The subscript x stands for instantaneous values and $\Delta h = h_x - h_i$ which makes it negative at all times. Equation [3-35] is used for friction compensated flow stress and it arises from the Von Mises stress analysis for plastic flow while equation [3-36] is used when no friction is considered [43].

As for Von Mises strain, the following equation can be used, based on the Von Mises yielding criteria [87]:

$$\varepsilon = \frac{2}{\sqrt{3}} ln\left(\frac{h_x}{h_i}\right) \qquad [3\text{-}37]$$

The Von Mises factor of $\frac{2}{\sqrt{3}}$ that is used in both the flow stress and strain equations is a multiplier that corrects the stress–strain relationship obtained in an experimental uniaxial tension or compression tests to plane strain conditions. This acts as a conversion factor that makes it possible to apply the uniaxial loading experimental results for the analysis of the plane-strain flow problem of flat rolling.

3.7 Multipass compression tests and interpass time

Interpass time is the period that a rolled item takes between the scheduled rolling passes after the previous pass has been completed, i.e. when the leading edge of the strip, for example, becomes the trailing edge upon reversing in a Steckle mill. It is a term commonly used in multipass rolling schedule and Figure 3.25 shows a 15 multipass simulated torsional test. This is one of the most important parameters as it can affect the final mechanical properties of the material being rolled as some form of "static" restoration will be present in this time interval. The effect of changing the interpass time on grain size, for example in controlled rolling, has been widely studied together with other parameters such as deformation temperature and strain per pass [88], [89]. It may be used to determine whether dynamic recovery, or dynamic recrystallisation or metadynamic recrystallisation or static recrystallisation occurs during rolling as these also affect the following pass' rolling loads. Generally, interpass times are much greater than deformation times.

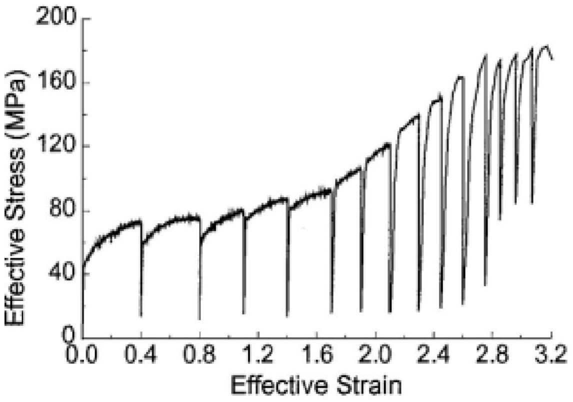

Figure 3.25: A typical hot rolling torsional multipass schedule [90]

It is mentioned in the literature [91] that when the interpass time is short, insufficient time is available for conventional recrystallisation during the interpass delay. The amount of carbonitride precipitation that can take place is also severely limited. As a result, dynamic recrystallisation is easily initiated because the critical strain for its initiation is more easily reached as there is accumulation of strain and the dislocation density is high. Also, the absence of precipitation during the short interpass intervals in tandem rolling mills permits the initiation and propagation of dynamic recrystallisation.

It has also been suggested [91] that precipitation of carbides is necessary because recrystallisation can only be arrested during finish rolling, and only if a copious number of precipitates form during passage of the strip between successive mill stands. When the interpass time is high, a high density of precipitates is promoted by the occurrence of some cooling ΔT between passes (which increases the driving force for precipitation) and interpass intervals. Moreover, the accumulation of strain and dislocation density is low and this makes the critical strain for the initiation of dynamic recrystallisation to be delayed or to be absent. This means that recrystallisation is most readily arrested during rolling in slow reversing mills, such as plate and Steckel mills, while precipitation plays a much smaller role in tandem mills, such as hot strip, rod, and other mill installations where interpass times are short [91].

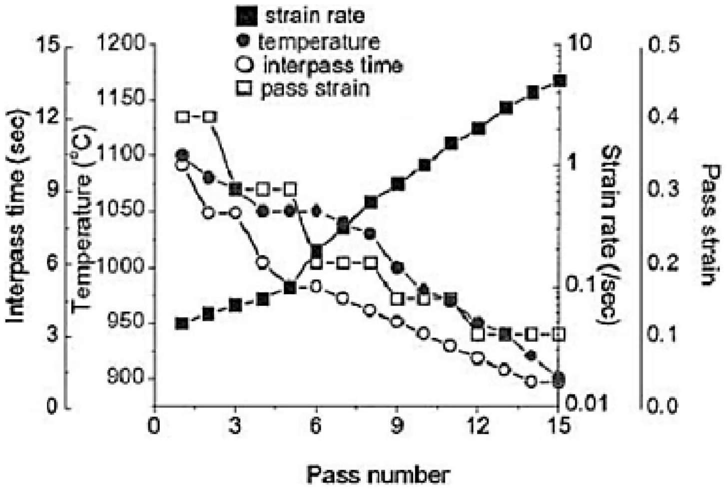

Figure 3.26: **Plots of Interpass time against pass number showing the effects of deformation temperature, interpass time, strain rate and strain[91]**

3.8 The dynamic recrystallisation to dynamic recovery transition temperature ($\mathbf{DR_{TT}}$)

The mean flow stress (MFS) for each pass under multipass tests is calculated from the flow curves using the following relationship [43]:

$$MFS = \frac{1}{\varepsilon_2 - \varepsilon_1} \int_{\varepsilon_1}^{\varepsilon_2} \sigma d\varepsilon \qquad [3\text{-}38]$$

This equation is a representation of an area under the stress–strain curve. The calculated results are plotted against deformation temperature as shown in Figure 3.27. Deformation is usually initiated at high temperature and terminated at low temperatures. It can be observed that the MFS gradually increased at each pass as the temperature decreased and that there is a clear change of gradient signalling the change in the softening mechanism, i.e. from DRX to DRV. This transition temperature has been observed in most steels that have Nb and Ti as some of the alloying elements. The point where this change in gradient takes place is often referred to as the nil–recrystallisation temperature (T_{nr}) but in this report, it will be referred to as the dynamic recrystallisation to dynamic recovery transition temperature, (DR_{TT}) because (T_{nr}) has been exclusively used for the controlled rolled Nb-containing steels. This temperature is known to be the temperature below which material stores energy during an anisothermal interrupted test, i.e. softening processes are not completed during the pass as well as during the pause between the passes [92]. This change in gradient is also attributed to the accumulation of strain or work hardening, that takes place since the specimens are now being deformed below the DR_{TT} [90]. When the strain rate is low, the DR_{TT} is also low, which means that it is easier to be in the DRX region at a lower temperature when deformation is done slowly. When rolling is done above the DR_{TT} the austenite grain sizes are refined and the work hardening that is accumulated within the roll pass is eliminated [91].

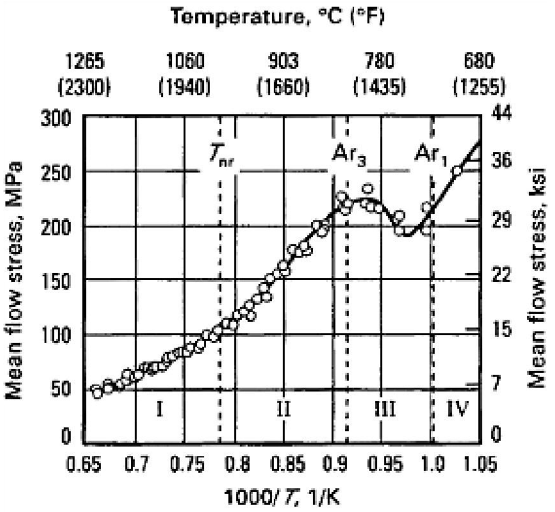

Figure 3.27: Plot of MFS against 1/T showing the relationship between MFS and deformation temperature and how to find T_{nr} [93]

CHAPTER 4: EXPERIMENTAL PROCEDURES

4.1 Introduction

In this chapter, the specimen materials, the specimen preparation and the experimental procedures that were followed for the investigation on the characterisation of the two steels under study are presented. The choice of techniques used is based on the industrial information provided by Columbus Stainless as well as the available scientific information and insights provided by the available literature. In order to properly characterise the two steels, deformation temperature, strain rate and interpass time were taken as experimental variables because changing chemical composition and heat treatment beyond the choice of the two stainless steels were not part of the objectives of this study.

4.2 The specimen materials

Table 4.1 shows the chemistry, in weight percentages, of the materials used in this work which were kindly sourced from Columbus Stainless SA. Two specimens were provided for each steel type and were sampled from the head and tail sections of the strip. Presented in Table 4.2 are the chemical compositions of the two austenitic stainless steels under study as recommended by the American Iron and Steel Institute for comparison.

Table 4.1: Weight % composition of AISI 321 and AISI 304 steels of the as received specimens

Steel	C	Cr	Si	Mn	N	Ti	Al	B	Co	Cu	Ni	P	S
321	0.027	17.13	0.59	1.08	0.0105	0.346	0.012	0.0003	0.09	0.12	9.11	0.021	0.0005
304	0.024	18.21	0.38	1.43	0.0725	0.001	0.003	0.0031	0.07	0.15	8.11	0.027	0.0023

Table 4.2: Weight % composition of 321 and 304 steels as recommended by AISI

	C	Cr	Si	Mn	N	Ti	Ni	P	S	Fe
321	0.08	19.00	0.70	2.00	0.10	0.70	12.00	0.045	0.030	Balance
304	0.08	20.00	0.70	2.00	0.10	0.00	12.00	0.045	0.030	Balance

The composition percentages shown in Table 4.3 are maximum values allowable according to American Iron and Steel Institute.

4.3 Optical microscopy

In order to determine whether the material has been processed correctly it is crucial to carefully analyse the initial microstructures and chemistry for product reliability. Preparation of metallographic specimens demands that a step-by-step procedure be followed. From time immemorial, the following have been the steps that have been used: documentation, sectioning and cutting, mounting, coarse grinding, fine grinding, polishing, etching, microscopic (optical and electron-based) examination and sometimes these steps are followed by microhardness testing. For this to be effective it is imperative that all specimens be kept as clean as possible and that these preparation steps be religiously followed. Wrongly prepared specimens can influence wrong interpretation of what is being observed. The microstructures so revealed tell a "story" which helps in decision making. This is the main focus of metallography which is defined as the scientific study of the constitution and structure of metals and alloys, its control through processing and its influence on properties and behaviour [94].

As mentioned before, two alloys were investigated in this study. The as received specimens' micrographs for 321 and 304 were obtained after preparing specimens according to the ASTM E3 and E883 standards and etched according to ASTM standard E407 so that practically all grains are distinct and visible. The specimens for optical microscopy analysis were prepared by initially cutting the specimen pieces out of the as received transfer bar materials. The pieces were cut along the rolling direction (RD) with a Struers Disctom–5 cutting machine under water cooling. The specimens were then mounted either using the thermoplastic transparent hot mounting resin powder or bakelite black hot mounting powder in readiness for grinding and polishing. The machine used for mounting was an Impetech HA 30. The specimens were mechanically ground systematically using silicon carbide paper with grit sizes of 240, 320, 400, 800, 1000 down to 1200 under water cooling using Struers grinding and polishing machines. After grinding, the specimens were polished using polishing cloth from 9 micron, 5 micron, 3 micron to 1 micron in that order while periodically applying the lubrication and diamond polishing suspension and paste to enhance surface smoothness. For better results, the specimens were either electro–polished using an Electromet electro–polishing machine from Buehler Ltd or the process from grinding up to polishing was done using the Struers RotoPol–11 polishing and grinding machine.

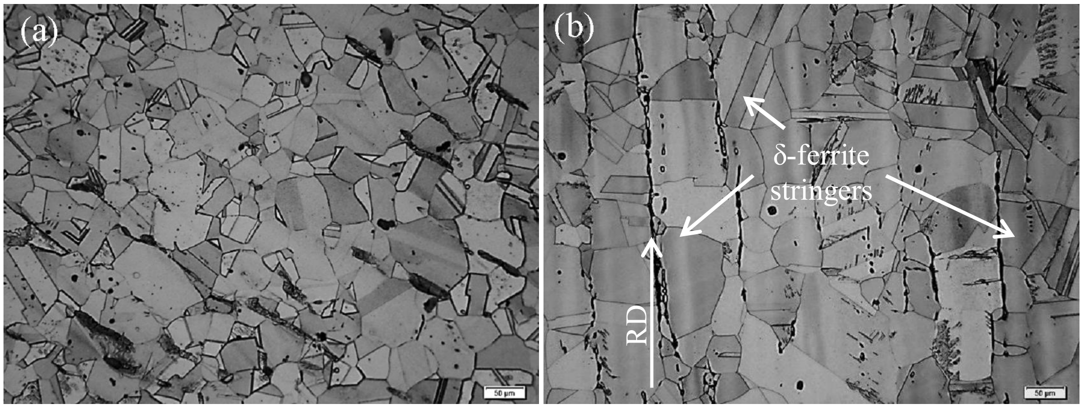

Figure 4.1: The as received micrographs with (a) showing the as received AISI 304 microstructure and (b) showing the as received AISI 321 microstructure.

Two etchants were used that revealed the microstructures very well which are: (a) "1 part" solution (made of 1 part HCL, 1 part ethanol and 1 part water) and (b) modified Kalling's reagent. The specimens in the "1 part" solution had to be stirred continuously for about 10 minutes in order to nicely reveal the grain boundaries and as for the Kalling's modified reagent, the specimens were swabbed for about 5 seconds because this etchant heavily attacked the surfaces of the specimens. After etching, the microstructures were examined using an Olympus BX51M microscope with a high resolution digital camera using the Olympus Stream Essentials software.

Optical microscopy was basically used as an initial characterisation tool in order to gain a first understanding on the difference between the two steels. It was observed that there is a distinctive difference between these two materials, i.e. mainly on the presence of $\delta -$ ferrite which is seen as a series of stringers and the difference in the grain size. There is evidently more $\delta -$ ferrite in 321 as compared to 304. The $\delta -$ ferrite stringers lie parallel to the RD. 321 did not show a clear distinctive pattern in terms of grain size as can be seen from the micrograph but a variety of large, medium and small grains. It was also observed that the grains were banded for 321 in that one band was dominated by large grains while the other band was being dominated by small grains.

4.4 Compression test procedure

Usually the austenitisation temperature is left to the researcher's discretion but the austenitisation temperature and the soaking time play an important role as they have an effect on the starting grain size, the degree of carbide dissolution in the matrix. The reheating schedule should aim at dissolving as much of the carbides as possible so that the material remains in equilibrium before deformation starts. This can only happen if the austenitising temperature and the soaking period are sufficient and, therefore, the Thermo-Calc computer software was used to determine the soaking temperature during the hot rolling simulations. In hot rolling, as with all hot–working processes, temperature control is required for success. If the soaking time is insufficient, the hotter exterior will flow in preference to the cooler, stronger interior. Conversely, if a uniform temperature material is allowed to cool prior to working or has cooled during previous working operations, the cooler surfaces will tend to resist deformation. Cracking and tearing of the surface may result as the hotter, weaker interior tries to deform [95]. It is, therefore, advisable that the specimen should be heated to a uniform elevated temperature which can be ascertained by holding it at the austenitising temperature long enough although the definition of "long enough" is also often loosely defined.. The period can also be guided by the volume and type of carbides that are expected in the specimen. Obviously if the specimen temperature is inhomogeneous, the subsequent deformation will then likewise be inhomogeneous.

In order to obtain the hot working parameters, two uniaxial compression experiments were devised with the first experiment designed to observe the hot rolling characteristic constants followed by simulation of the Steckel hot rolling process. The Gleeble 1500^{TM} thermomechanical simulator — that is equipped with a specially constructed load cell fitted to a stationary part of the load train [96], was used in both types of experiments and the procedures are shown in the two sections below. The hot working parameters are fundamentally important because they are used in the universal hot working equations to predict the flow behaviour of the material as it is being plastically deformed.

4.4.1 Hot rolling characterisation

In this series of experiment, the specimens with chemistry as provided in §4.2, were machined to a standard size of 10 mm in diameter and 15 mm in length. The specimens were heated and subjected to a single isothermal deformation test (single hit), see Figure 4.2

below. Initially the specimen was heated to point 1 say at 1100°C as shown in Figure 4.2 and then held at that temperature for homogenisation up to point 2. From point 2, the specimen was heated to point 3 which was 1250°C which was above the planned deformation temperature where it was soaked for fifteen minutes before reducing it to the deformation temperature in two stages. This procedure ensured that the temperature of the specimen was uniform. Figure 4.3 shows the Gleeble machine that was used and the specimens before deformation and after deformation.

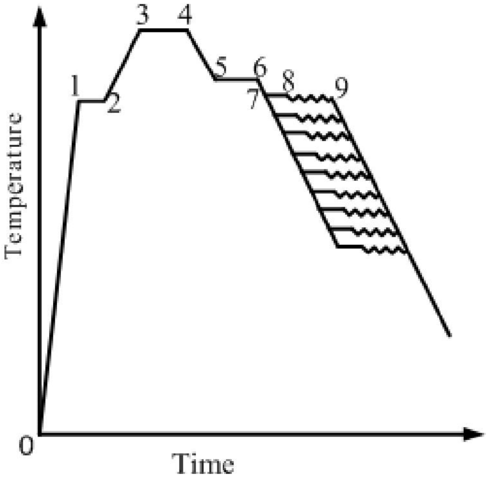

Figure 4.2: Schematic diagram showing the procedure that was followed during the heating and isothermal single compression of specimens at various test temperatures.

All the tests followed the same pattern of heating and each test was carried out to a constant true strain of 1.0 but varying the strain rates and test temperatures while the deformation time is dependent on the targeted strain rate. The strain rates used were $0.001s^{-1}$, $0.01s^{-1}$, $0.05s^{-1}$, $0.1s^{-1}$, $1.0s^{-1}$ $3.0s^{-1}$, and $5.0s^{-1}$ for each deformation temperature. Details of the deformation temperatures and strain rates are as shown in the Appendix A below.

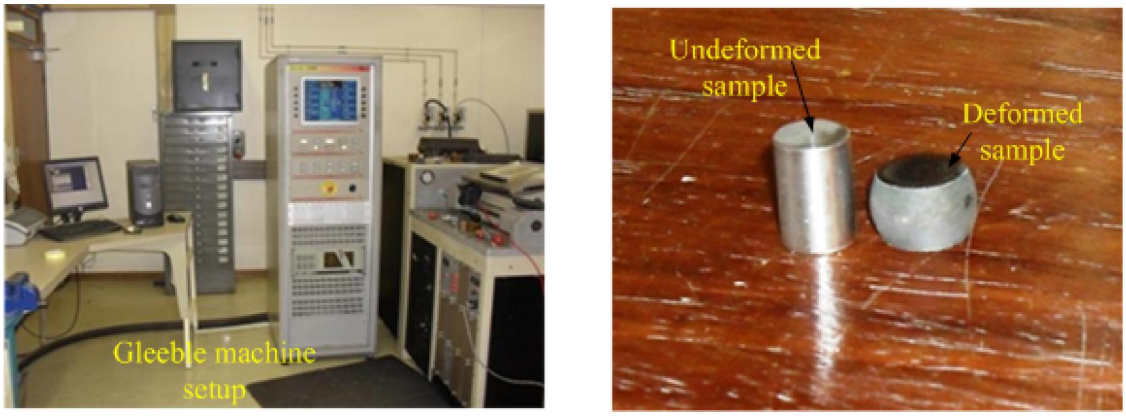

Figure 4.3: Pictures showing the Gleeble machine on left and the undeformed and deformed specimens on the right.

Argon gas was used during deformation to avoid excessive oxidation of the specimens and they were either air cooled or quenched to room temperature after deformation with a helium stream depending on the targeted results of the experiment. Tantalum foils were placed between the anvils that are placed between the deformation jaws of the Gleeble and the specimen on both ends to avoid barrelling (nonuniform deformation) of the specimen as it deforms. The K–type thermocouple was used to measure temperature. The ends of the specimen were machined flat to avoid inhomogeneous loading which could lead to significant differences in the $\delta - \varepsilon$ curve responses. Specially designed "isothermal platens" which minimised both the radial and axial "drain" of heating from the specimen were also used to ensure a reasonably uniform temperature distribution throughout the specimen.

4.4.2 Multipass simulation tests

These were multiple hit uniaxial compression tests performed with the aim of simulating the multi-pass Steckel mill hot rolling process. The data used to determine the hot rolling parameters were obtained from the mill logs kindly supplied by Columbus Stainless from their Steckel mill and the calculations of the hot working parameters were done using the constitutive equations as outlined by Stumpf [96]. Figure 4.4 shows the deformation schedule where a specimen was heated the same way as outlined under single hit deformation schedule followed, however, by deformation in nine subsequent passes. After each compression test, the specimens were quenched in helium fast enough to freeze the microstructures so that there was no further microstructural transformation taking place. The materials used in the deformation tests were of the same dimensions as outlined in §4.4.1 4.5.1 above and the experimental plan used is as shown in Table 4.3 with P1 to P9 identify the individual pass numbers.

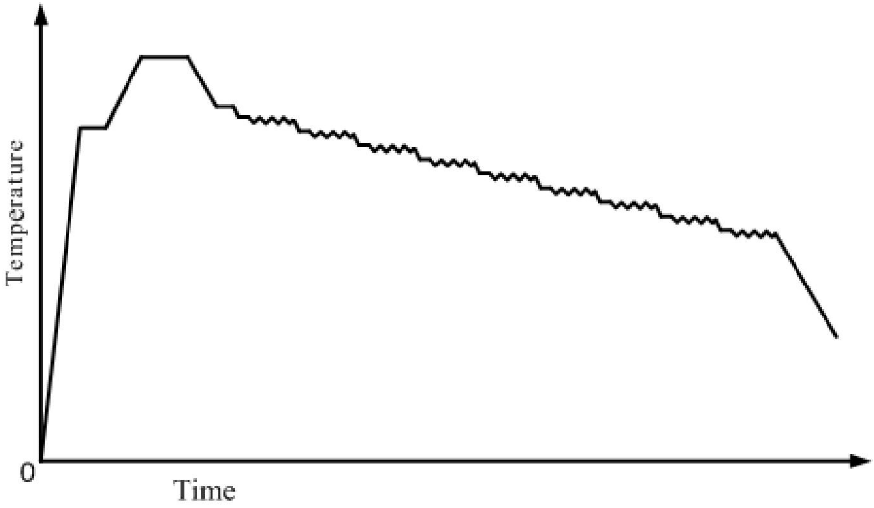

Figure 4.4: Sketch depicting the deformation schedule where a specimen was heated as outlined under the single hit deformation schedule but with the deformation in nine passes.

Table 4.3: **The table showing multipass experimental schedule for both AISI 321 and AISI 304**

Pass	P1	P2	P3	P4	P5	P6	P7	P8	P9
Entry height H (mm)	15.0	13.7	12.5	11.5	10.5	9.5	8.6	7.7	6.8
Exit height h (mm)	13.7	12.5	11.5	10.5	9.5	8.6	7.7	6.8	6.0
Change in height ΔH (mm)	1.3	1.2	1.0	1.0	1.0	0.9	0.9	0.9	0.8
Entry Temp (°C)	1200	1150	1100	1050	1000	950	900	850	800
Exit Temp (°C)	1200	1150	1100	1050	1000	950	900	850	800
Time	1.0	1.1	1.0	1.1	1.2	1.1	0.1	0.1	0.0
Cumulative ΔH (mm)	-1.3	-2.5	-3.5	-4.5	-5.5	-6.4	-7.3	-8.2	-9.0
True strain per pass (ratio)	-0.1	-0.1	-0.1	-0.1	-0.1	-0.1	-0.1	-0.1	-0.1
Cumulative true strain (ratio)	-0.1	-0.2	-0.3	-0.4	-0.5	-0.6	-0.7	-0.8	-0.9
Interpass time (s)	20.0	20.0	20.0	20.0	20.0	20.0	20.0	20.0	20.0

4.5 Initial austenite grain size test

In this test, the aim was to measure the prior austenite grain size after reheating but before the start of deformation of these two materials – 304 and 321. The specimens were heated to about 1250°C for 2 hours to grow the grains and then fast quenched in helium to freeze the microstructures. The microstructures are shown in Figure 4.5 and 4.6 for the two steels. An attempt was made to carry out a grain size measurement by mean line intercept method according to ASTM E1181 / E112, but it proved to be a difficult exercise because of the type of microstructures which were a mixture of various sizes of grains interspersed with twins.

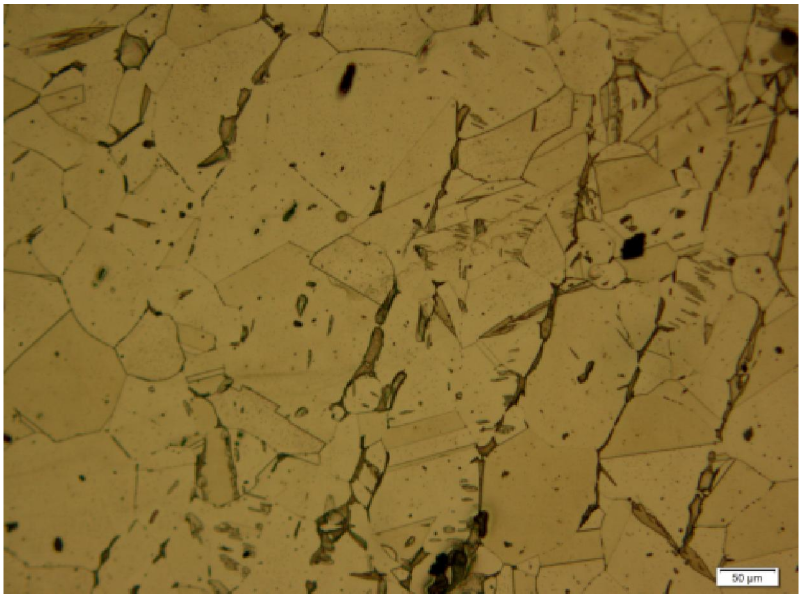

Figure 4.5: **Micrograph showing the starting grain structure of AISI 304. The specimens were heated to 1250°C for 2 hours and then quenched in helium to preserve the microstructures. The specimens were then etched using the "one part" solution.**

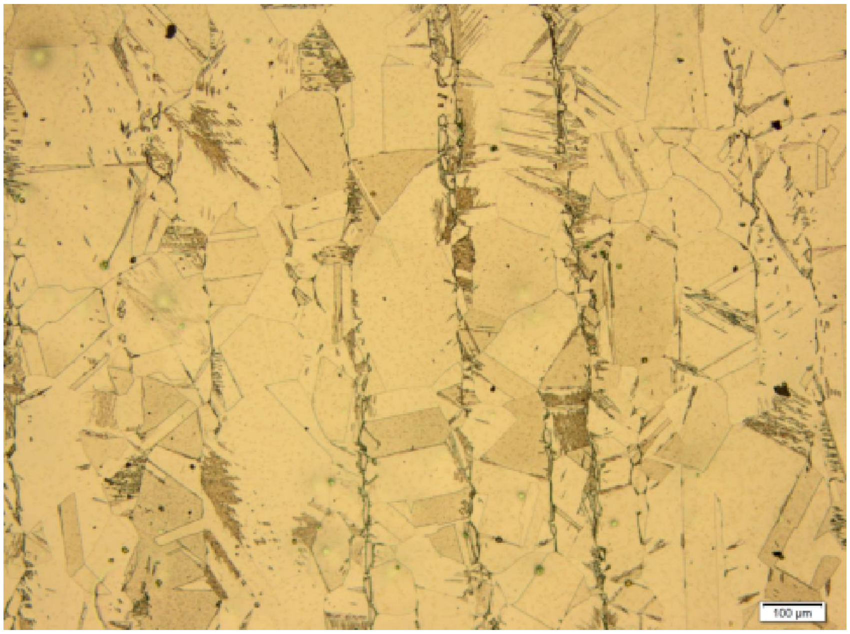

Figure 4.6: Micrograph showing the starting grain structure of AISI 321. The specimens were heated to 1250℃ for 2 hours and then quenched in helium to preserve the microstructures. The specimens were then etched using the "one part" solution.

4.6 Microhardness measurements

These were done according to ASTM standard number E384 to compare differences in hardness of the as-received 304 and 321 since hardness is related to the ultimate tensile strength of the material. Hardness tests were done using a Future-Tech Microhardness Test FM-700 machine fitted with a diamond indenter and this machine gives the Vickers hardness reading with the load ranging from 1 to 2000 kgf.

4.7 Scanning Electron Microscope specimen preparation

The magnifications that are not practical with light microscopes are possible with electron microscopes. There are a variety of electron microscopes and one good example is the scanning electron microscope (SEM). Electron beams are used to scan the surface of the specimen under study where the reflected beam of electrons is collected and this produces the picture on the screen which can then be capture and processed with software. There is no special preparation for the specimens required in order to use the SEM as the specimens are mostly prepared in the same way as described in §4.3. SEM was mainly used for the characterisation of the microstructures and for qualitative microanalysis and not for any quantitative analysis in this work.

The analyses were conducted using a Jeol JSM – 6300 field emission gun scanning electron microscope operated at $15\,kV$ accelerating voltage. This instrument was interfaced to an EDAX energy dispersive x-ray spectrometer and analysis system. The microstructure, surface morphology and qualitative chemical analysis of the two steels and inclusions were examined using secondary electron and backscatter electron imaging techniques.

4.8 Transmission Electron Microscope specimen preparations

The Transmission Electron Microscope (TEM) is another example of electron microscopes available for higher magnification analysis technique. It is described as a microscope that produces an image by using electron beams that are transmitted or pass through the specimen and this makes the examination of internal features at high magnifications possible. Solid materials are highly absorptive to electron beams and as such the specimens to be examined are supposed to be very thin. The rods 3 mm in diameter were initially cut by electro-machining from the specimens as shown in Figure 4.7 below and then using a diamond saw cutter, thin slices were cut off from the middle of the cylinders where the maximum deformation had occurred. The slices were then mounted using wax and polished manually to a thickness of about $50\mu m$ and there after using twin jet polishing method, the specimens were thinned to about $1\mu m$ thickness before examined in the TEM.

The TEM studies were carried out using a Philips CM 200 TEM operating at an accelerating voltage of $160kV$ and also a Jeol JEM 2100F field emission TEM using an acceleration voltage of 200kV. The second TEM was equipped with a double tilt specimen holder and connected to a computer containing a semi-automatic program for orientation measurements.

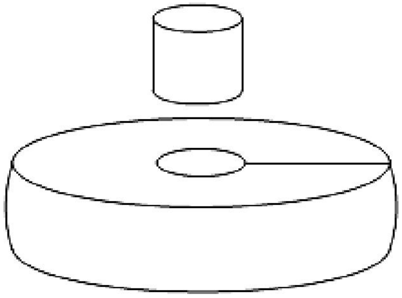

Figure 4.7: Sketch illustrating how the cylinders were cut out of the Gleeble 1500^{TM} hot deformed specimens.

Nine lab deformed specimens representing one specimen per pass were taken for TEM examination plus two as-received specimens from both the steels 304 and 321. The as-received specimens were used as benchmarks. The deformation temperatures were systematically reduced from $1200^{\circ}C$ down to $800^{\circ}C$ as shown in Figure 4.8. The specimen at $1200^{\circ}C$ was deformed once, while the specimen at $1150^{\circ}C$ was deformed twice. This trend continued until the specimen at $800^{\circ}C$ had been deformed nine times. The deformation times represented the number of passes; for instance, the specimen that was deformed five times at $1000^{\circ}C$ represented five passes. Six thin foils on average were produced per specimen for TEM examination.

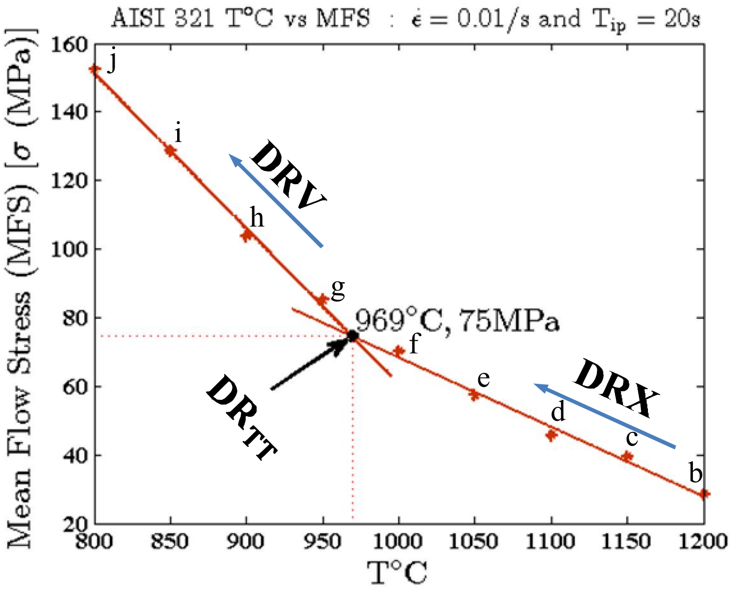

Figure 4.8: Graph showing representative multipass compression results that were carried out for the AISI 321 steel. The deformations were started at 1200℃ which is represented by data point (b) down to 800℃ which is represented by the data point (j).

4.9 Electron Backscattered Diffraction (EBSD) Sample Preparation

The Electron backscattered diffraction (EBSD) technique of microstructural analysis was performed with the SEM as shown in Figure 4.9. This is a FEI NOVA NanoSEM 230 FEG at Mintek equipped with an EDAX Digiview EBSD Camera operated at 20kV. It is used to get a wide range of analytical data such as, crystallographic orientation studies (texture), phase identification and grain size measurements amongst others. According to the literature [97], a diffraction pattern can be obtained in much less than a second, and it is suggested that pattern quality is improved by utilizing a longer scan time. The quality of the diffraction pattern, regardless of the collection time, influences the confidence in indexing the pattern and depends mainly upon the degree of removal of damage in the lattice due to specimen preparation-induced damage. Generally, the removal of this damage can be obtained using electrolytic polishing or ion-beam polishing. Because of the acute angle between the specimen and the electron beam (70 – 74°), exceptional surface flatness is also necessary for best results.

It is also mentioned in literature [97] that microstructural image quality in polarized light is dependent upon the elimination of preparation damage and upon the quality of the microscope's optics. Consequently, when preparing these metals and alloys for SEM EBSD, always check the polarized light response of those specimens that will respond to polarized light to verify the preparation quality before performing EBSD. For cubic metals, etch first with a general-purpose reagent to confirm the nature of the expected microstructure. A well-prepared, un-etched specimen will exhibit a good grain-orientation contrast image with a backscattered (or forescattered) electron detector; another good test for freedom from surface damage.

Figure 4.9: **The Mintek's FEI NOVA NanoSEM 230 FEG used for EBSD**

Specimen preparation methods for metals and alloys have been developed that yield excellent results using straightforward methods that generally require less than about twenty-five minutes. High-purity metals require more preparation time than alloys. Automated preparation equipment is recommended, as the methods will be performed accurately and reproducibly. Manual preparation should be avoided as it cannot produce flatness, phase retention and damage removal as easily as automated processing and is less reproducible [97].

Because damage removal is very important, it is obvious that each step in the preparation sequence must be designed to impart minimal damage. In almost all cases, the specimen must be sectioned to provide the desired size and plane-of-polish. Sectioning imparts more damage than any other step in the preparation sequence, so it is obvious that cutting damage must be minimized. It is generally necessary to use an additional final polishing stage using colloidal silica. Final polishing should not be prolonged, but just sufficient to achieve the desired surface finish without causing excessive relief [97].

The method used for sample preparation in this study was similar to what was described above for normal optical microscopy.

To enhance flatness of the samples, colloidal silica which is a chemo-mechanical polish, i.e., it combines the effect of mechanical polishing with etching, was used after the 1 m finish. This type of stock removal is ideal in many cases for EBSD, as a damage-free surface can be obtained with little effort with a typical abrasive size of 0.05 micron. Colloidal silica crystallizes readily and will ruin polishing cloths if left to dry and a film can form on the polished surface of the sample which must be removed. A convenient method to achieve this is to flush the polishing cloth with water during the last few seconds of polishing to clean the sample surface. Remove and dry the sample in the usual manner, using a solvent with low water content and not so volatile as to cause water condensation on the surface. Alcohol is ideal, whereas acetone is not. Flush the polishing cloth with water until all traces of colloidal silica are washed away, spin to drain and store in a suitable container such that contamination of the polishing cloth cannot occur. Meticulous attention to avoiding contamination of polishing cloths is an important aspect to achieve the best results [98].

The specimens were further electropolished in a solution of 5% perchloric acid and 95% ethanol using an applied voltage of about 40V dc for a period of 45 sec to ensure excellent surface finish.

4.10 Phases as predicted by Thermo–Calc

Thermo-calc is the powerful thermodynamic equilibrium phase simulation commercial software that has been used over the years to predict phases both by the academia and industry. It is also used for estimating precipitation of second phases in materials, phase compositions, phase properties and phase transformations. There are other comparable software that can predict equilibrium phase transformations like DICTRA, ChemSage, GEMINI, HSC, Pandat, FACTSage, MTDATA, JMatPro, MICRESS and PrecipiCalc [100] among others. In this work, Thermo-Calc version 5 was used to check the phases for the two steels under study, mainly in the hot working area with the TCFE6 database. The phase predicted by Thermo-calc confirms that indeed the structure of these two materials is austenite at all temperature as expected. Figure 4.10 shows the plots of temperature against weight per cent carbon in which the Thermo-Calc global equilibrium stable phase predictions for the two steels are shown while Figure 4.11 and Figure 4.12 shows the volume fractions of some of the phases present. The calculations were performed for temperatures between 900 K and 1600 K while the carbon content ranged from 0 to 0.06%. The vertical dotted lines in both graphs indicate the composition of carbon according to:

Steel	C	Cr	Si	Mn	N	Ti	Al	B	Co	Cu	Ni	P	S
321	0.027	17.13	0.59	1.08	0.0105	0.346	0.012	0.0003	0.09	0.12	9.11	0.021	0.0005
304	0.024	18.21	0.38	1.43	0.0725	0.001	0.003	0.0031	0.07	0.15	8.11	0.027	0.0023

, i.e. the typical carbon content for the steel and the numbers along the dotted lines have been inserted to indicate the stable compounds as predicted by Thermo-Calc as follow:

a. AISI 321:

1. $(\delta - Fe) + \gamma + Ti(CN) + Ti_4C_2S_2$
2. $\gamma + Ti(CN) + Ti_4C_2S_2$
3. $\gamma + Ti(CN) + MnS$
4. $\gamma + Ti(CN) + Laves\ phase\_C14\#1 + M_3P + MnS$
5. $\gamma + Laves\ phase\_C14\#1 + M_3P + MnS + \sigma + Ti\ (CN)$
6. $(\alpha - Fe) + \gamma + Laves\ phase\_C14\#1 + M_3P + MnS + \sigma + Ti\ (CN)$
7. $\gamma + Ti(CN) + Laves\ phase\_C14\#1$

b. **AISI 304:**

1. $Liquid + (\delta - Fe) + \gamma + Corundum + MnS + Spinel$
2. $\gamma + Corundum\_M_2O_3 + MnS + Spinel$
3. $\gamma + BN\_hP4 + MnO\_Al_2O_3 + MnS + Spinel$
4. $\gamma + BN\_hP4 + MnO\_Al_2O_3 + MnS + Spinel + Z\,phase$
5. $\gamma + BN\_hP4 + MnO\_Al_2O_3 + MnS + Spinel + Z\,phase + M_{23}C_6$
6. $\gamma + BN\_hP4 + MnO\_Al_2O_3 + MnS + Spinel + Z\,phase + M_{23}C_6 + HCP\_A3\#2$
7. $\gamma + BN\_hP4 + MnO\_Al_2O_3 + MnS + Spinel + M_{23}C_6 + HCP\_A3\#2$
8. $\gamma + BN\_hP4 + MnO\_Al_2O_3 + MnS + Spinel + M_{23}C_6 + HCP\_A3\#2 + M_3P$
9. $\gamma + MnO\_Al_2O_3 + MnS + Spinel + M_{23}C_6 + HCP\_A3\#2 + M_3P$
10. $\gamma + MnO\_Al_2O_3 + MnS + M_{23}C_6 + HCP\_A3\#2 + Cr_2B\_Orth + \sigma + M_3P + spinel$
11. $(\alpha - Fe) + \gamma + MnO\_Al_2O_3 + MnS + Spinel + M_{23}C_6 + HCP\_A3\#2 + M_3P + Cr_2B\_Orth + \sigma$

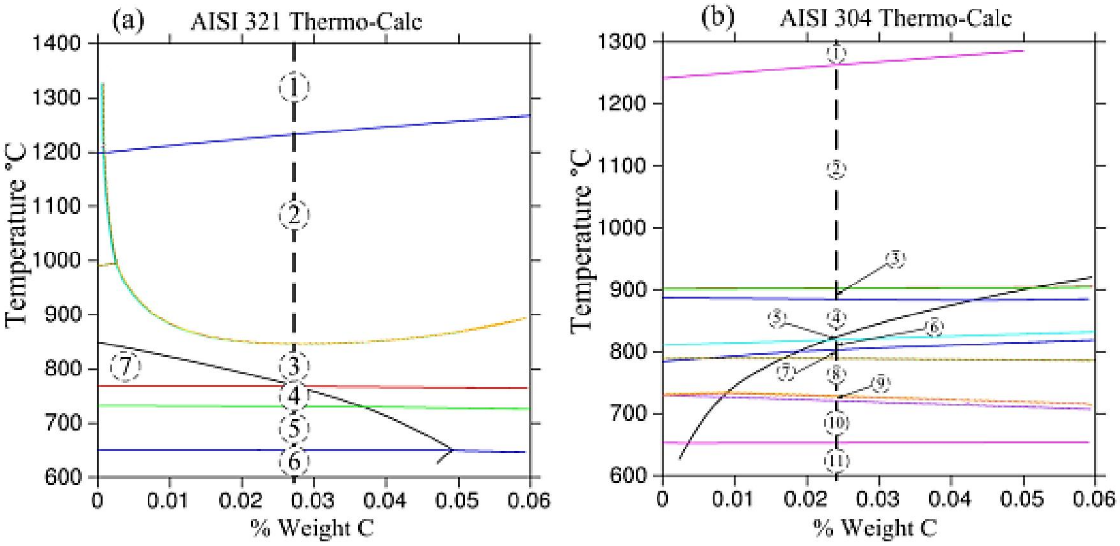

Figure 4.10: **Thermo-Calc predictions of stable phases for (a) AISI 321 and (b) AISI 304 stainless steels.**

Thermo-Calc reports the γ phase as FCC_A1 but if there is more than one phase with a fcc structure, the labelling changes to $FCC\_A1\#1$ for the main γ matrix and FCC_A1#2 for the secondary phase. If there are more than two phases with the fcc lattice, the numbering continues as FCC_A1#3, FCC_A1#4 so on. The bcc structure is not differentiated in Thermo-Calc between delta ferrite $(\delta - Fe)$ and alpha iron $(\alpha - Fe)$ because both of them are simply shown as BCC_A2 on the equilibrium phase diagram.

It has been reported [101] that the formation of the stable compound $Ti_4C_2S_2$ usually occurs at elevated temperatures and that this compound remains undeformed during hot rolling because of its property of high hardness at high temperatures. Titanium carbonitride, $Ti(CN)$, is a second phase which is a blocky rectangular and hard titanium rich carbide of the form MC that is yellowish in colour. As mentioned before, titanium is added as a stabiliser in the

321 steel to tie up the carbon as well as nitrogen in solution. Apart from the prevention of sensitization, the other reasons for producing this Ti stabilized steel is that the low carbon concentration, which is almost interstitial free, improves the quality of enamel coatings and formability. The $Ti(CN)$ was not expected to form in AISI 304 because it contains only trace amounts of titanium.

The Manganese sulphide MnS, is less stable than $Ti_4C_2S_2$ and it has been observed [101] that MnS can be deformed into undesirably long stringers during hot rolling and Ti has the ability to restrain the formation of MnS stringers so formed during deformation. But the influence of titanium on MnS stringers is dependent on the amount that remains after the formation of $Ti_4C_2S_2$ and $Ti(CN)$.

The phosphide, $(Cr + Fe + Ni + P)$, precipitates in the form of M_3P and is a needle shaped secondary phase which nucleates on either complex defects or dislocations resulting from the initial thermomechanical processing [102].The influence of phosphorus in the formation of phosphide makes the steel brittle and if in excess, it will render the steel less ductile and tough.

The Laves phase is an intermetallic compound that has the general stoichiometric composition of AB_2 and is named after a German chemist and researcher Fritz Laves who first described it. This phase is often said to be a minor phase precipitating intragranularly in the form of equiaxed particles, with occasional occurrence at the grain boundaries [103]. There are three different laves phase types identified so far and these are classified on the basis of geometry alone. For example cubic $MgCu_2$ $(C15)$ and two hexagonal $MgNi_2$ $(C36)$ laves phases. Thermo-Calc predicts that in this steel (AISI 321) there is a laves phase of type C14 that has a hexagonal structure similar to $MgZn_2$. It is made up of $(Fe + Ti + Si + Ni + Cr)$ with trace amounts of $Mn, Co, Cu,$ and Al. They are of particular interest in modern metallurgy research because of their abnormal physical and chemical properties. They are brittle at ambient temperature and their brittleness is attributed to the difficulty in moving dislocations in their presence and currently the research in the possible use of laves phases is on using it to produce heat resistant steels [104].

Sigma phase $(\sigma - \text{phase})$ is one of the most commonly found intermetallic phases precipitating in austenitic steels at lower temperatures and its characteristic property is that it is highly brittle. It has a detrimental effect on creep properties when precipitated on grain boundaries [103] and it also reduces the corrosion resistance of the steel by removing chromium from the austenitic matrix. From the provided graphs of 321 and 304, it can be seen that this phase forms below the Steckel rolling temperatures and therefore it can be safely said that it will not have any influence on hot rolling properties unless very slow cooling is employed after the completion of rolling.

Corundum is an oxide compound of the type M_2O_3 that forms at high temperatures in type 304 steels where M is mainly made up of Cr and Fe. Two other forms of oxide that form in 304 are (a) alumina (Al_2O_3) which is mainly made up of Al, Mn and O and (b) a spinel- type oxide of the form AB_2O_4 where A is Mn and Cr with trace amount of Fe. The formation of these oxides is well documented in the literature [105][106].

Boron nitride BN_hP4 is another phase compound found in 304 with chemical formula BN as type hP4. This phase is made up of equal numbers of boron and nitrogen atoms. BN has a hexagonal close packed structure and is isoelectronic to a similarly structured carbon lattice and thus exists in various crystalline forms.

The $Z-$phase can be considered to be one of the minor phases in 304 steel under study as it is only prevalent in Nb stabilised 304 stainless steels such as in the AISI 347 stainless steel. In the steel under study here, there is just a trace amount of Nb. The $Z-$phase is characterised as a complex carbonitride that forms in steels that contain relatively high levels of nitrogen but the conditions for its formation are not very clear, and even less is its relative stability when compared to other carbonitrides. It is mainly thought to be made up of Cr, V, Nb. Much of the information about $Z-$phase is well documented in the literature [107].

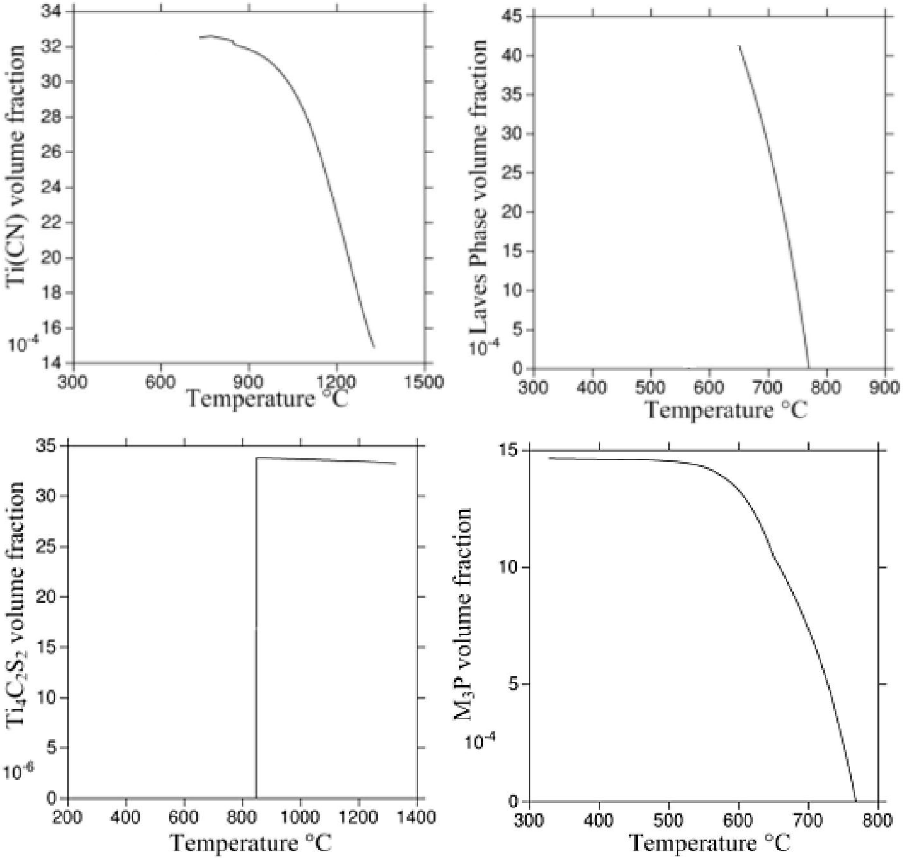

Figure 4.11: Predicted volume fractions of some of the phases as a function of temperature for AISI 321 stainless steel under equilibrium conditions obtained from Thermo-Calc.

Here HCP_A3#2 is another carbonitride with hexagonal close packed structure and is composed of Cr, Nb, Fe, Nb, Mn, C and *N* with trace amount of Ni and Ti and very rich in Cr. Whereas $M_{23}C_6$ is a carbide with M consisting of Cr, Fe, Nb, Mn, B and Ni with trace amount of Co. These two carbonitrides and carbides have a detrimental effect on the material’s mechanical properties.

The graphs below are plotted for the individual phase fractions against temperature as predicted by Thermo-Calc under equilibrium conditions.

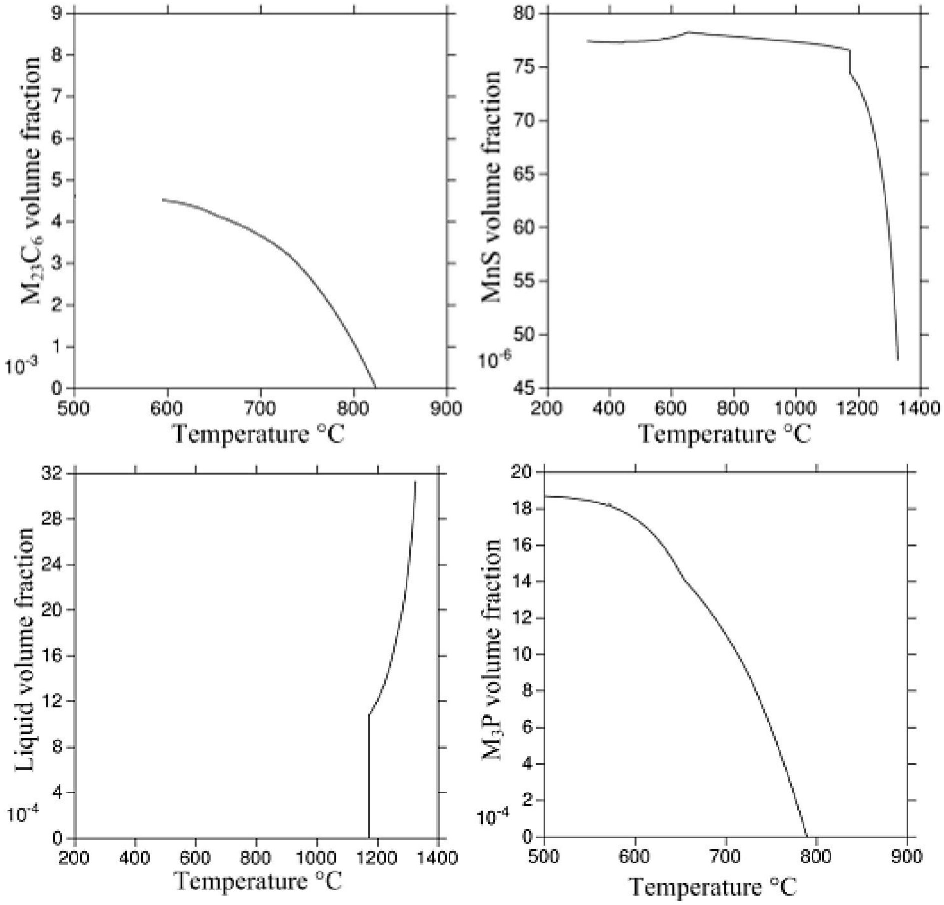

Figure 4.12: **Predicted volume fractions of some of the phases as a function of temperature for AISI 304 stainless steel under equilibrium conditions obtained from Thermo-Calc.**

CHAPTER 5: EXPERIMENTAL RESULTS

5.1 Introduction

In this chapter, all the results obtained using uniaxial compression tests, phases as predicted by Thermo-Calc, TEM, SEM, microhardness tests and the normal optical microscopic analysis will be presented. On compression tests, both single hit and multi-hit compression test results will be presented in this chapter. The main emphasis will be to highlight the two regions under study namely dynamic recrystallisation and dynamic recovery as these have a direct bearing on the mechanical properties of the material after deformation such as hardness which may be converted to ultimate tensile strength of the material. The bulk of the results will be on the steel 321 as it is the main material under study and 304 is taken as a benchmark. Moreover the procedures that were performed on 321 were equally performed on 304. Wherever possible, results on 321 will be presented first and then the 304 results will follow. In the presentation of the experimental results, the following will be highlighted:

a. Mill data analysis
b. Effect of strain rate $(\dot{\varepsilon})$ on peak strain $\left(\varepsilon_p\right)$ and flow stress $\left(\sigma\right)$
c. Effect of test temperature $\left(\mathrm{T_d}\right)$ on peak strain $\left(\varepsilon_\mathrm{p}\right)$ and flow stress $\left(\sigma\right)$
d. Effect of interpass time $\left(\mathrm{T_{ip}}\right)$ on peak strain $\left(\varepsilon_\mathrm{p}\right)$ and flow stress $\left(\sigma\right)$

Mill logs provide the much needed vital information for modelling such as the strain rate, the mill loads, the interpass time and the number of passes among others. Using the steps and equations as described in §4.4.2 and Table 10.2 in the appendix, Table 10.1 provides an example of the extracted results. It must be mentioned here that a number of authors have tried to produce new mathematical models recently but those listed in Table 10.2 form the backbone of all the models. These equations have been used to analyse and describe the cold, warm or hot flat rolling processes of materials in a number of studies.

The data collected from the Gleeble was extracted and entered into an Excel matrix template as shown in Table 10.1. The information presented in this table is cut off in the middle as it is only used to show the MFS, average T, time, force, total strain stroke, etc and is a representation of all the data that was collected and analysed. When plotting the stress – strain curves, there were three columns of main interest namely; the true negative strain column, the friction compensated flow stress column and flow stress column with no friction considered.

5.2 Single hit Gleeble tests results for 321

For characterisation of the hot rolling parameters, the data from the Gleeble was converted to true Von Mises flow stress and strain by using the corrective equation [3-35] that takes into account the effect of friction between the pressure anvils and the specimens. The Von Mises stress and strain are the most frequently used invariant functions to describe plastic deformation [43]. They are a representation of plane stress and strain as the deformations were uniaxial compression. A constant value of 0.1 for the coefficient of friction μ, was used for all test temperatures as it was in good agreement with the measured data and is a value which was similarly used in the literature [99] for ferritic steels.

There were 40 uniaxial isothermal single pass compression deformation tests which were planned according to Table 10.2 in the appendix and the graphs below show the effect of changing deformation temperature and strain rate. The calculations were done using equation [3-35] and [3-36] for the friction compensated and no friction flow stresses respectively. The plotted graphs' information comes from Table 10.1. The graphs demonstrate the following

a. that as the strain rate is increased at constant deformation temperature, the peak stress increases and vice versa.
b. that when the deformation temperature is lowered at constant strain rate, the peak stress increases and vice versa. This is so because there is a greater extent of dynamic recovery or recrystallisation when the temperature is raised and, therefore, at higher deformation temperatures, the material flows more easily.
c. that as the strain rate is increased at constant deformation temperatures, the peak strain increases and vice versa. This can be attributed to the effect of dislocations at a high strain rate, when there is little room for dislocation annihilation and as a result the dislocations pile up impeding the ease of material flow.

Figure 5.1 shows typical stress-strain graphs for steel 321 for conditions that depict the microstructure undergoing (a) DRV and (b) DRX respectively. The black dotted lines are when the friction compensated equation was used (equation [3.35] while the red lines are when friction was not considered in the equation (equation [3.36].

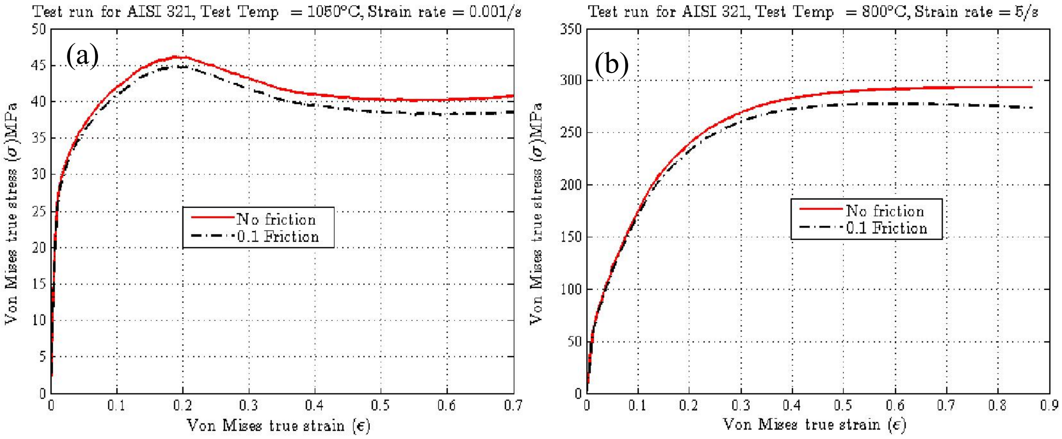

Figure 5.1: Graphs showing the Von Mises stress – strain curves for AISI 321 austenitic stainless steel specimens that were deformed by single-hit at different strain rates and temperatures.

From now onwards all the stress flow curves that will be presented were generated using the friction compensated equation only. The graphs in Figure 5.2 below show the effect of keeping the strain rate constant while varying the deformation temperature for 321 stainless steel. From the graphs, it can be seen that as the deformation temperature is raised, the maximum flow stress decreases. Moreover, when the strain rate is raised, the flow curves' characteristics show that the dominant mechanism is DRV while when the strain rates are low, the dominant mechanism becomes DRX.

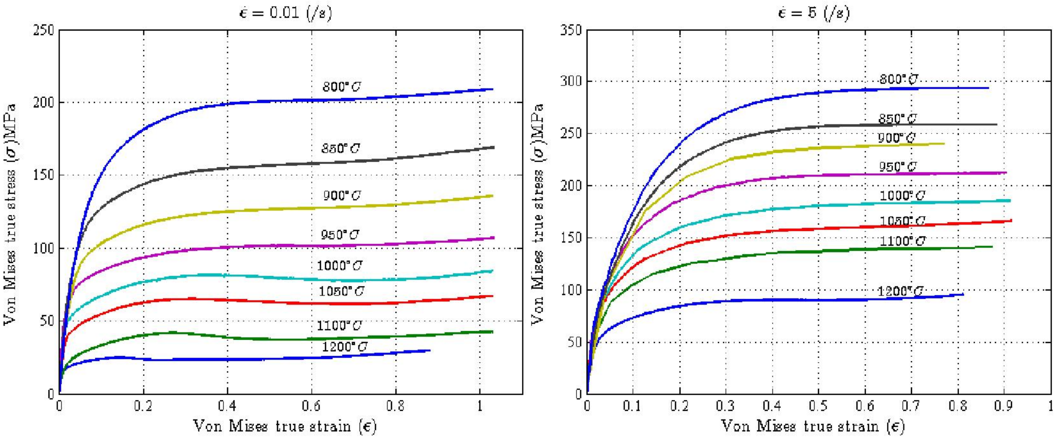

Figure 5.2: **Combined Von Mises stress – strain curves for 321 austenitic stainless steel with constant strain rate but varying deformation temperature**

The graphs in Figure 5.3 below show the effect of keeping the deformation temperature constant while varying the strain rate for the 321 stainless steel. The stress flow curves were generated using the friction compensated equation. From the graphs, it can be seen that at low deformation temperatures the flow curves' characteristics show that the dominant mechanism is DRV regardless on whether the strain rate is low or high while when the deformation temperatures are high, the dominant mechanism becomes DRX.

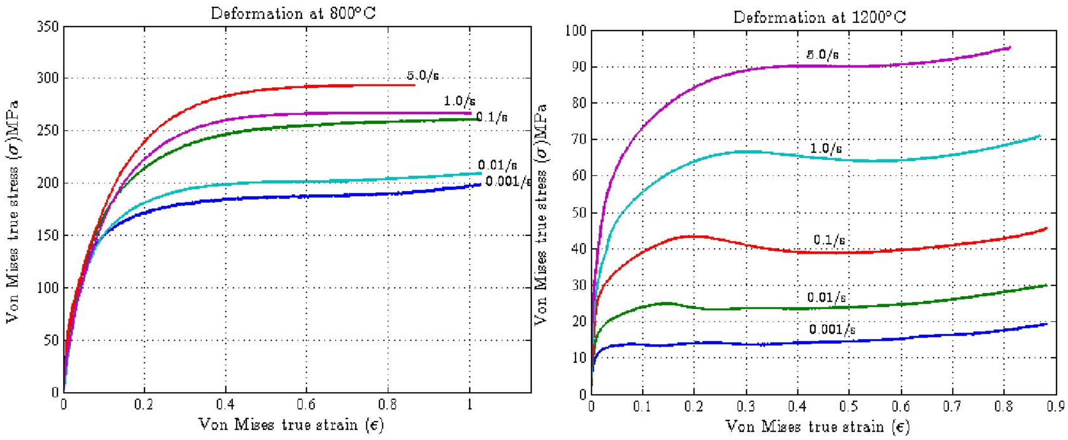

Figure 5.3: **Combined Von Mises stress – strain curves for AISI 321 austenitic stainless steel with constant deformation temperatures but varying strain rates.**

5.3 Multipass Gleeble tests results for AISI 321

To further understand the effect of deformation temperature on the MFS, multipass tests were carried out with strain rates ranging from $0.001s^{-1}$ to $5s^{-1}$ and a total true strain of about 1.0 while the interpass time T_{ip} was kept constant at $20s$. The mean flow stress (MFS) per pass was calculated from the flow curves using the relationship described in equation [3-35]. A series of tests was mainly done in order to find the cut-off point that separates dynamic recrystallisation from dynamic recovery. These tests were done following the deformation schedule profiles shown in Figure 4.4 and the information given in Table 4.3. When the flow stress of each pass was plotted against the Von Mises strain, the profile is shown in Figure 5.4. The deformation was initiated at $1200^{\circ}C$ after soaking the specimens at $1250^{\circ}C$ for 15 minutes and terminated at $800^{\circ}C$ and Figure 5.5 shows the plots of MFS versus deformation temperature for the various deformation conditions indicated in each graph. It was observed that the MFS gradually increased at each pass as the temperature was lowered and that there was a clear change of gradient signalling the change in the softening mechanism, i.e. from DRX to DRV. The point where this change in gradient takes place is referred to as the dynamic recrystallisation to dynamic recovery transition temperature, $\left(\mathrm{DR_{TT}}\right)$. This temperature is known to be the temperature below which material stores energy during an isothermal interrupted test, i.e. softening processes are not completed during the pass as well as during the pause between the passes [92]. This change in gradient is also attributed to the accumulation of strain or work hardening that takes place since the specimens are now being deformed below the $\mathrm{DR_{TT}}$ [90]. The rate at which DRX takes place is given by the gradient from the start of deformation to the $\mathrm{DR_{TT}}$ transition while the rate at which DRV takes place is the gradient from the $\mathrm{DR_{TT}}$ transition to the end of deformation.

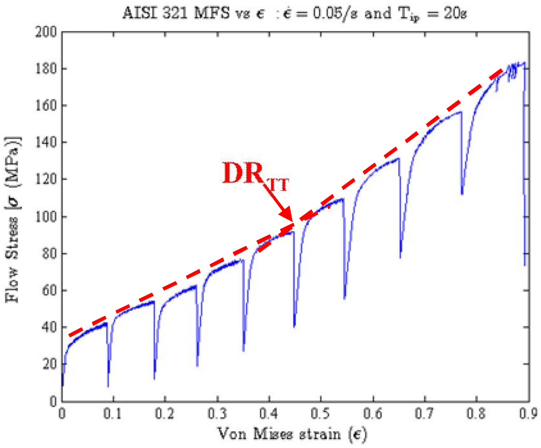

Figure 5.4: **The graph depicting multipass flow stress for each pass against strain for AISI 321.**

The graphs in Figure 5.5 below show the trend of the mean flow stresses that were calculated using equation [3-38] as strain rate and deformation temperatures were varied.

5.3.1 Deformation results at a constant interpass time but varying the strain rate

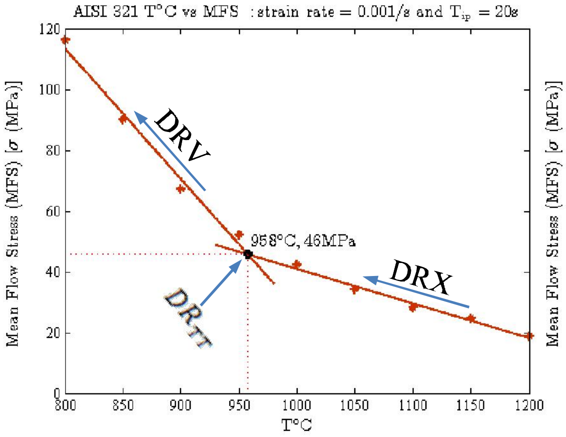

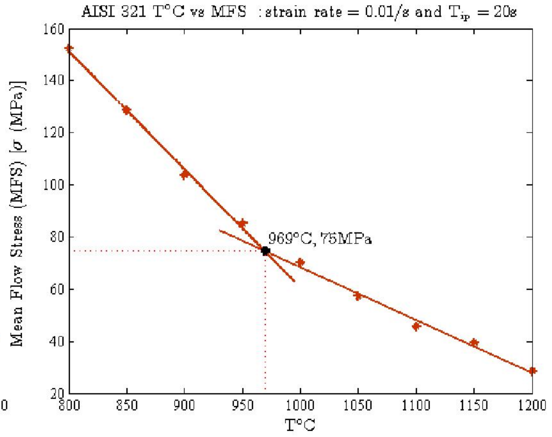

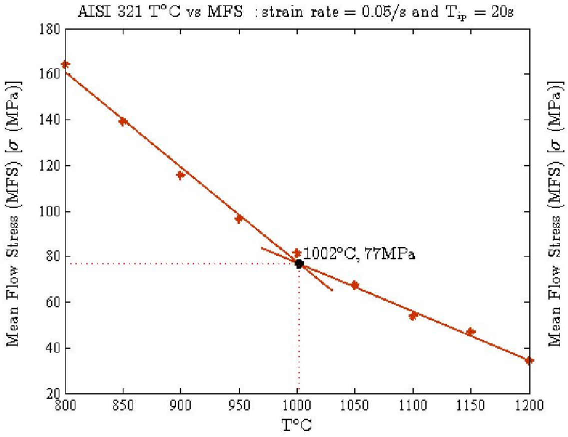

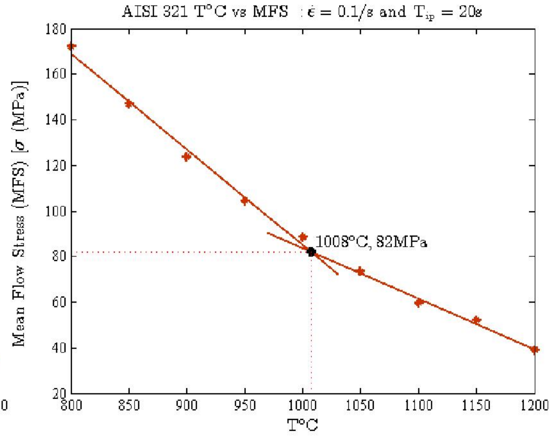

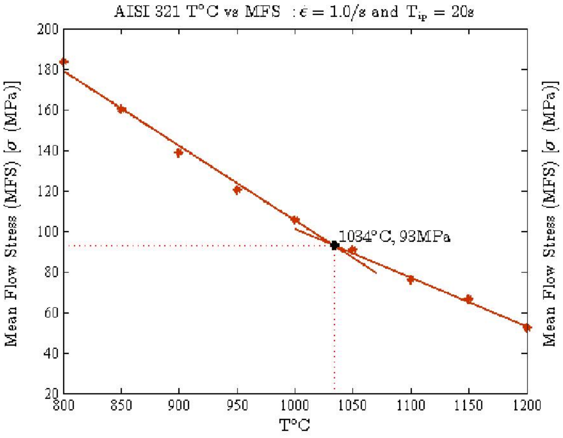

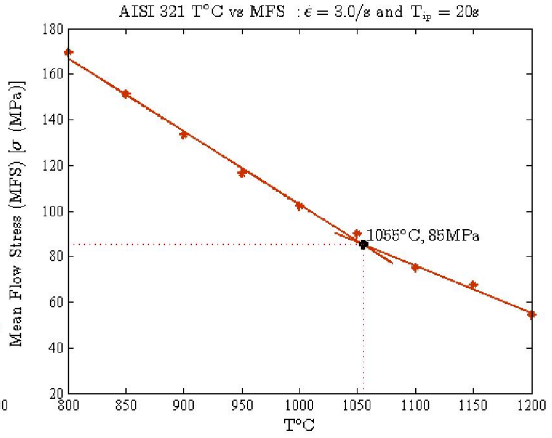

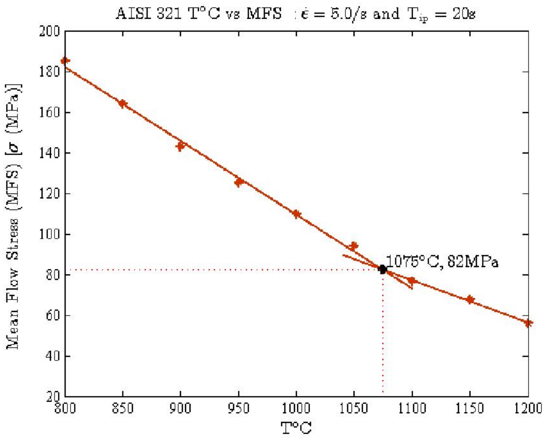

Figure 5.5: **The MFS versus deformation temperature for AISI 321 steel at constant strain rate and interpass time but varying the deformation temperatures.**

As may be seen from Figure 5.5, the dynamic recrystallisation to dynamic recovery transition temperature (DR_{TT}) shifts to higher temperatures as the strain rate increases. This means that at high strain rates it is very difficult for dynamic recrystallisation to occur unless the deformation temperature is increased.

5.3.2 Deformation at a constant strain rate and with varying interpass times

Multipass tests were also done to establish the effect of the interpass time on the DR_{TT} and the results are given in Figure 5.6 below.

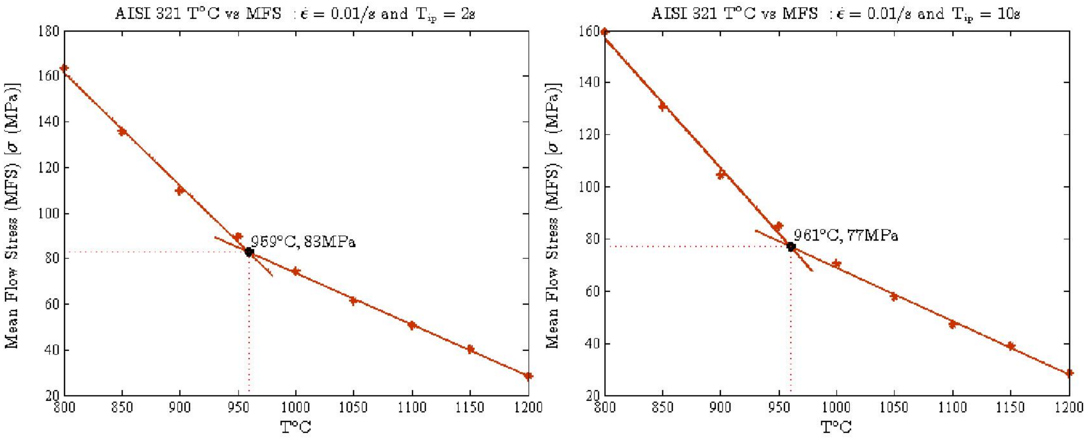

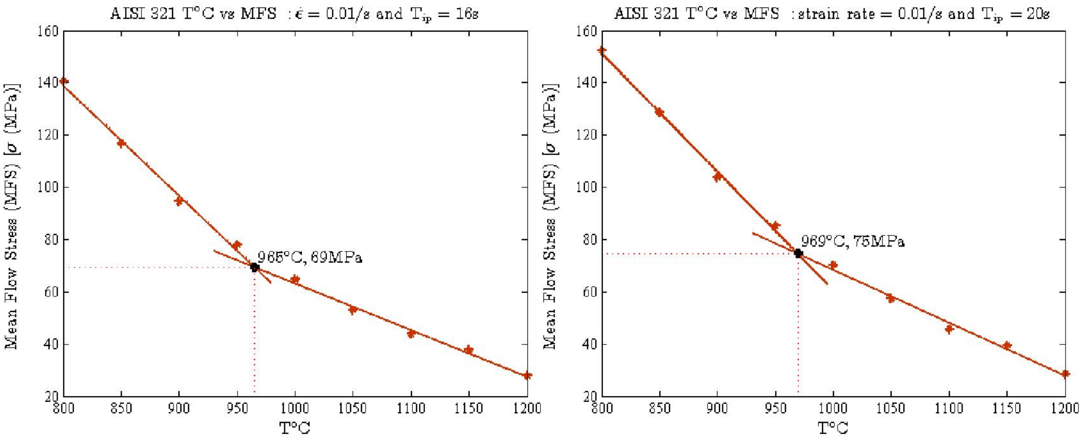

Figure 5.6: **The MFS versus deformation temperature for AISI 321 steel at constant strain rate but varying the deformation temperatures and interpass times.**

From these graphs (Figure 5.6), it can be observed that as the interpass time is increased, so does the DR_{TT} and the results in Figures 5.5 and 5.6 are respectively summarised in Figure 5.7(a) and (b) below with Figure 5.7(a) plotted with lnZ.

As may be seen from Figure 5.7(a), DR_{TT} increases with an increase in lnZ. Increase in lnZ comes from either increase in strain rate or lower deformation temperature. When the strain rate is low, the DR_{TT} is also low, which means that it is easier to induce DRX at a lower temperature when deformation is done slowly. When rolling is done above the DR_{TT}, the austenite grain size is refined because of complete DRX [91].

It is also evident from Figure 5.7(b) that as the interpass time is increased, the DR_{TT} increases correspondingly. This is attributed to the reduction in driving force for subsequent DRX by SRV during the interpass time.

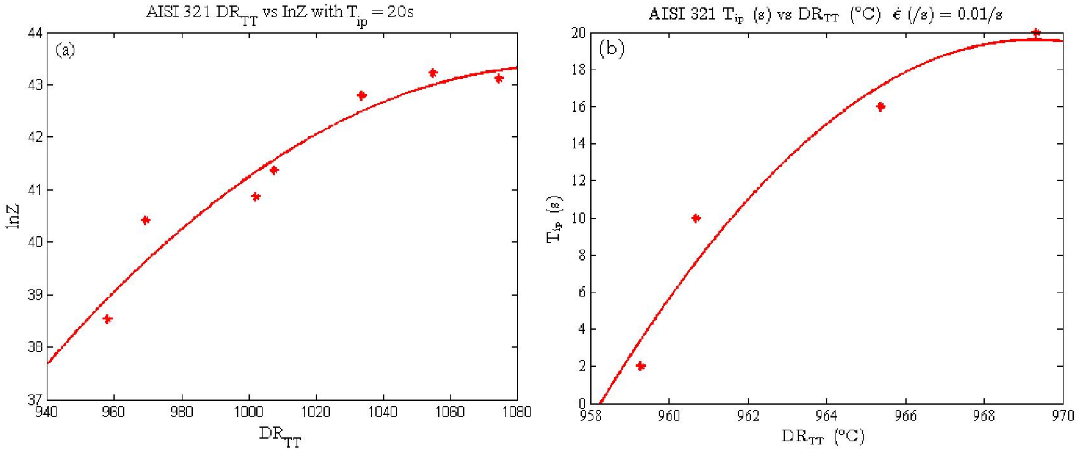

Figure 5.7: **Plots showing (a) the effect of $\dot{\epsilon}$ on the DR_{TT} and (b) the effect of T_{ip} on DR_{TT} for AISI 321 steel.**

When deformation is done at higher strain rates, DRV is predominant as dislocation re-arrangement requires less self-diffusion than DRX does. Likewise, longer interpass times allow the accumulated driving force to decrease making DRV in the next pass more likely than DRX. By using a fifth order polynomial curve fitting, the model that can be used to describe the relationship between strain rate $\dot{\varepsilon}$ and the $\mathrm{DR}_{\mathrm{TT}}$ at a constant interpass time of 20s but varying strain rate is:

$$\dot{\varepsilon} = a\mathrm{DR}_{\mathrm{TT}}^{5} + b\mathrm{DR}_{\mathrm{TT}}^{4} + c\mathrm{DR}_{\mathrm{TT}}^{3} + d\mathrm{DR}_{\mathrm{TT}}^{2} + e\mathrm{DR}_{\mathrm{TT}} + f \qquad [5\text{-}1]$$

with the following coefficients:

$a = -2.2534 \times 10^{-9}$

$b = -1.1347 \times 10^{-5}$

$c = -0.022838$

$d = 22.969$

$e = -11543$

$f = 2.319 \times 10^{6}$

By using a second order polynomial curve fitting, the model that can be used to describe the relationship between interpass time and $\mathrm{DR}_{\mathrm{TT}}$ at a strain rate of $0.01\mathrm{s}^{-1}$ is:

$$\mathrm{T}_{\mathrm{ip}} = a\mathrm{DR}_{\mathrm{TT}}^{2} + b\mathrm{DR}_{\mathrm{TT}} + c \qquad [5\text{-}2]$$

with coefficients:

$a = -0.16063$

$b = 311.39$

$c = -1.509 \times 10^{5}$

For instance, using Figure 5.7(a), if the deformations are to be done at $1000^{\circ}C$ and with a strain rate of 2.5 s^{-1} the expected mechanism is DRV while if deformations are to be done at $1060^{\circ}C$ with a strain rate of $1\mathrm{s}^{-1}$ the expected mechanism is DRX. These results are well corroborated with the single hit deformation tests that were done.

5.4 Single hit Gleeble tests results for AISI 304

Similar single pass deformation tests were done for 304 for comparison purposes which were scheduled according to table 10.3 and as may be seen, there were 21 tests in total. The graphs presented below demonstrate the similar trends as highlighted under 321 and the trends were found to be similar in general but with minor differences to 321.

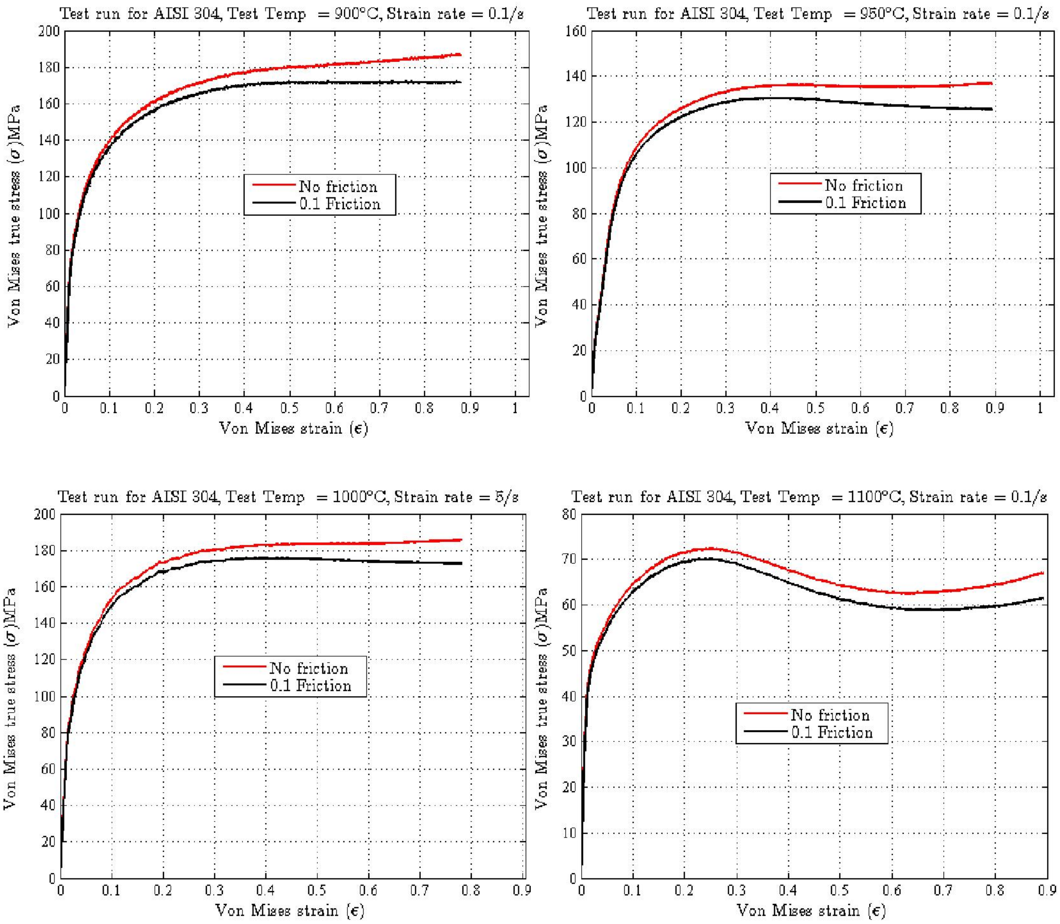

Figure 5.8: **Von Mises stress – strain curves for AISI 304 austenitic stainless steel**

The graphs in Figure 5.9 below show the effect of keeping the strain rate constant while varying the deformation temperature in 304. The general trends were also found to be similar to that of 321, i.e. DRX was dominant at slow strain rates and DRV at higher strain rates.

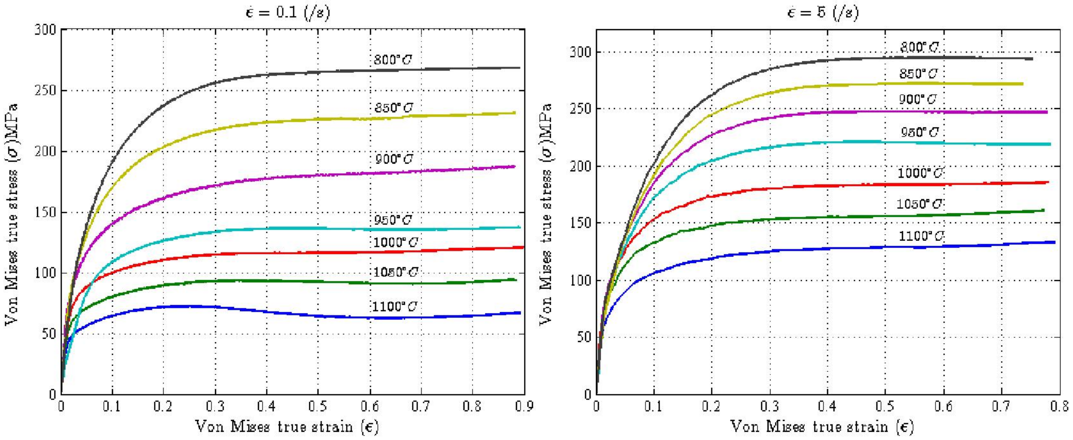

Figure 5.9: **Combined Von Mises stress – strain curves for the AISI 304 austenitic stainless steel with a constant strain rate but varying the deformation temperature.**

The graphs in Figure 5.10 below show the effect of keeping the deformation temperature constant while varying the strain rate in steel 304. It can be seen from the curves that as the temperature is raised, the peak flow stress drops (while keeping the strain rate constant) and that DRX is the dominant softening mechanism at higher deformation temperatures while DRV is dominant at lower deformation temperatures.

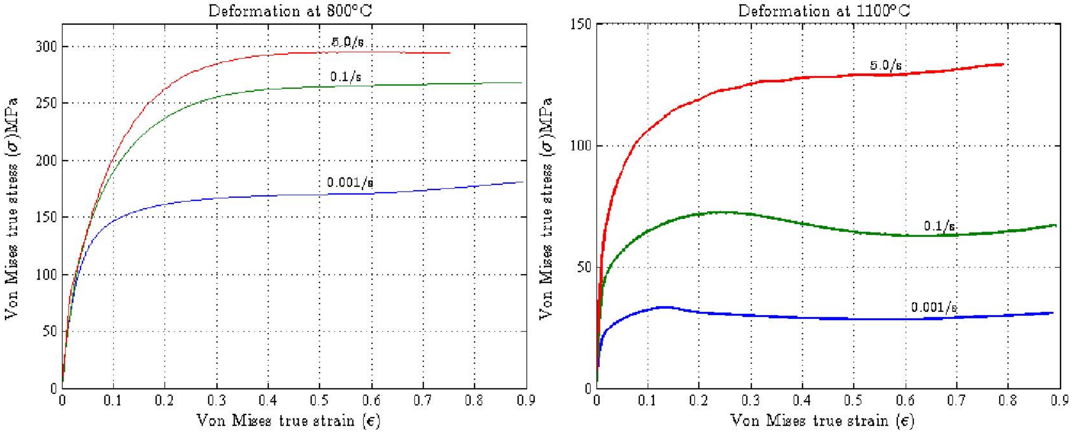

Figure 5.10: **Combined Von Mises stress – strain curves for AISI 304 austenitic stainless steel with constant deformation temperatures but varying the strain rate.**

5.5 Multipass Gleeble tests results for AISI 304

Similar tests as described in §5.3 were also done for AISI 304 and the similar procedure was followed to calculate the mean flow stress. Partial results are presented in Figure 5.11.

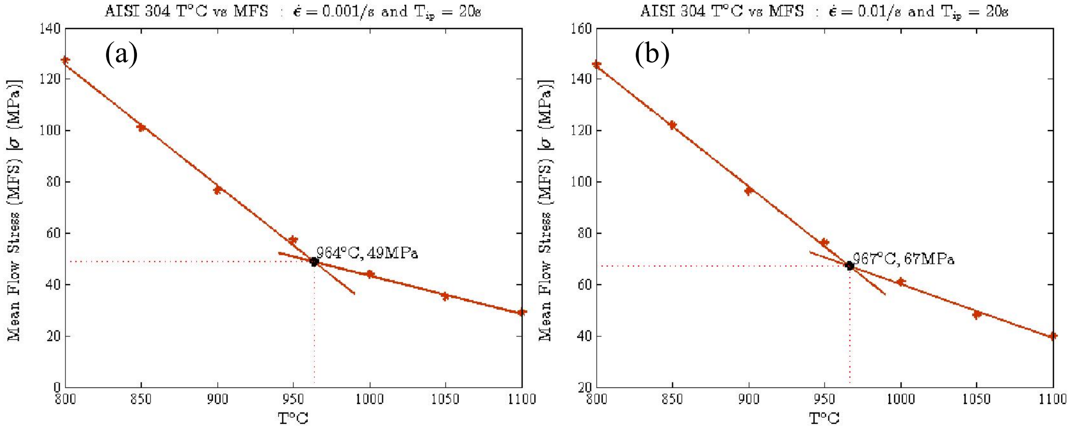

Figure 5.11: **Multipass MFS versus deformation temperature curves for AISI 304 austenitic stainless steel at constant interpass times but varying the deformation temperature and the strain rate. This figure shows that as the strain rate is increased, the MFS increases as well.**

5.6 TEM results

The TEM results of the uniaxial multipass compression tests are presented in this section. The microstructures were obtained from the two regions clearly marked DRX and DRV after deforming at a strain rate of 0.01/s, see Figure 5.12 below. Shown in

Figure 5.13 and Figure 5.14 below are the TEM micrographs from the as received materials and the experimentally deformed specimens. As may be seen from micrographs (c) to (f) in Figures 5.14 below, it is evident that DRX took place at a strain rate of 0.01 s^{-1} between 1150℃ and 1000℃ at an interpass time of 20s and below 1000°C, only DRV occurred. This observation is derived from the relatively dislocation-free microstructures for DRX as opposed to the DRV microstructures with a substantial amount of dislocations. In other words, there is a good correlation between these TEM results and the graph shown in Figure 5.14.

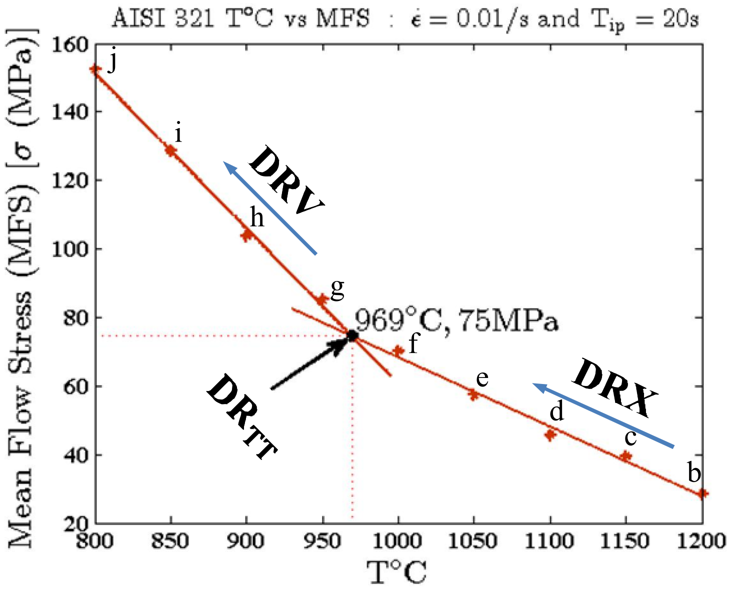

Figure 5.12: **Graph showing representative results of the multipass tests that were carried out on steel 321. The deformation was started at 1200℃ which is represented by data point (b) down to 800℃ which is represented by the data point (j).**

Figure 5.14(c) shows some evidence of necklacing which is regarded as a special type of the classical strain induced grain–boundary migration (SIBM) mechanism as the possible nucleation mechanism for DRX. Grain–boundary serration was also observed as another possible nucleation mechanism for DRX, see Figure 5.4(f) below for what appears to be the serrated austenite to austenite grain boundaries precursor of the nucleation of new DRX grains [108][109].

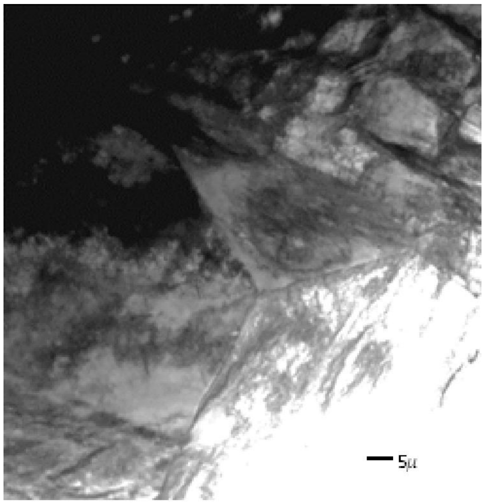

Figure 5.13: TEM micrograph for as-received hot band AISI 304 stainless steel

Presented below are TEM microstructures of 321 steel with Figure 5.14(a) coming from the as-received specimen while the rest are from the specimens that were experimentally deformed in a single isothermal compression test at different strain rates and temperatures.

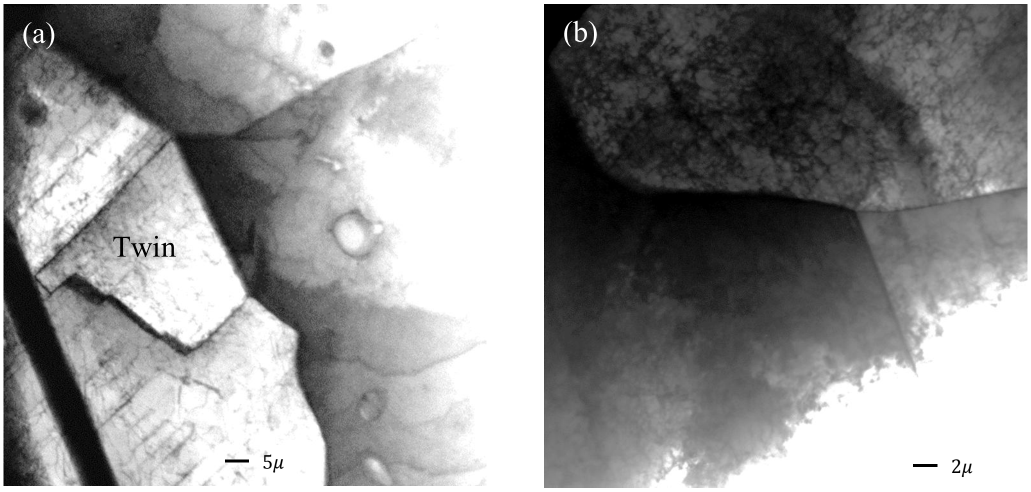

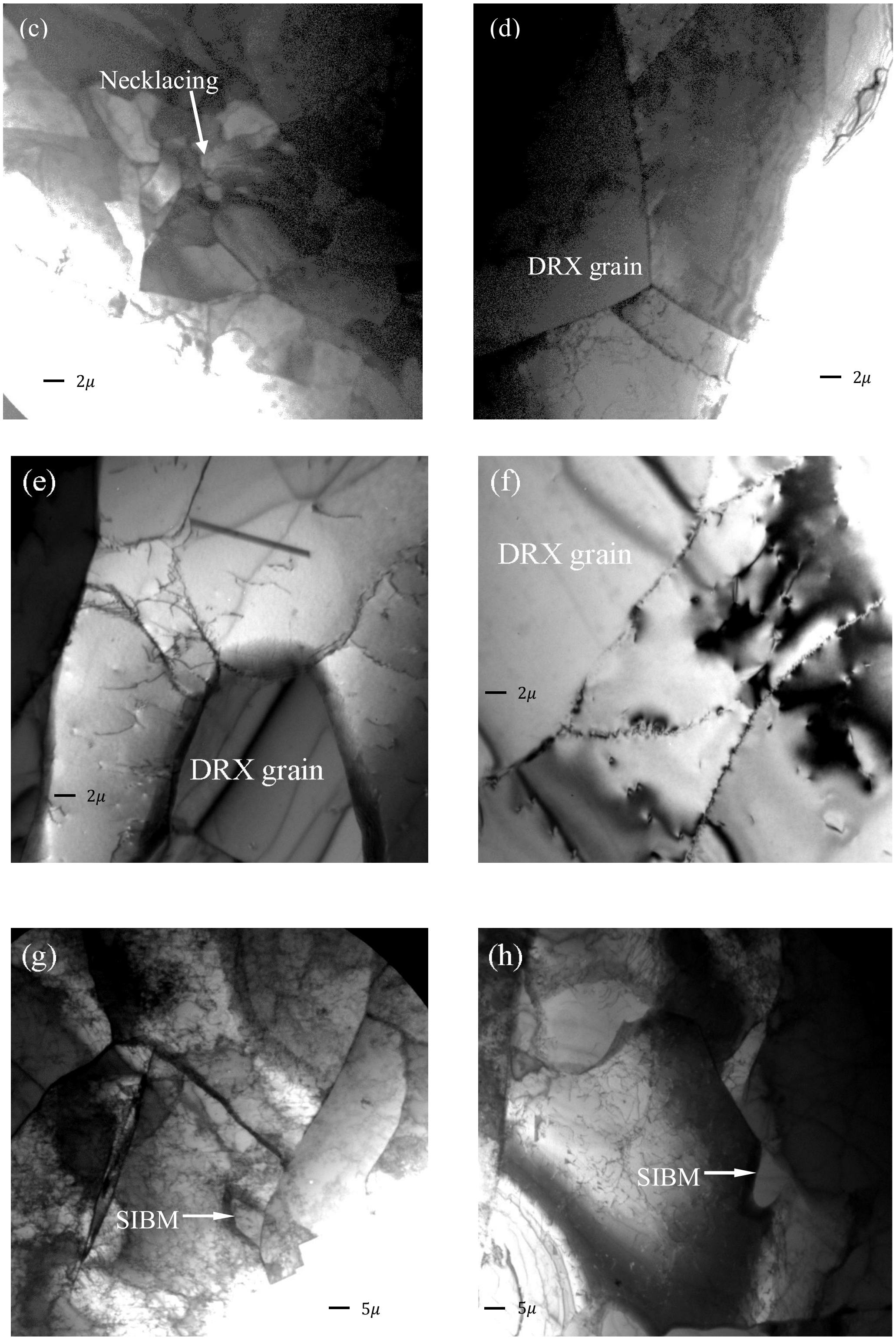
(c)
Necklacing
2μ
(d)
DRX grain
2μ
(e)
DRX grain
2μ
(f)
DRX grain
2μ
(g)
SIBM
5μ
(h)
SIBM
5μ

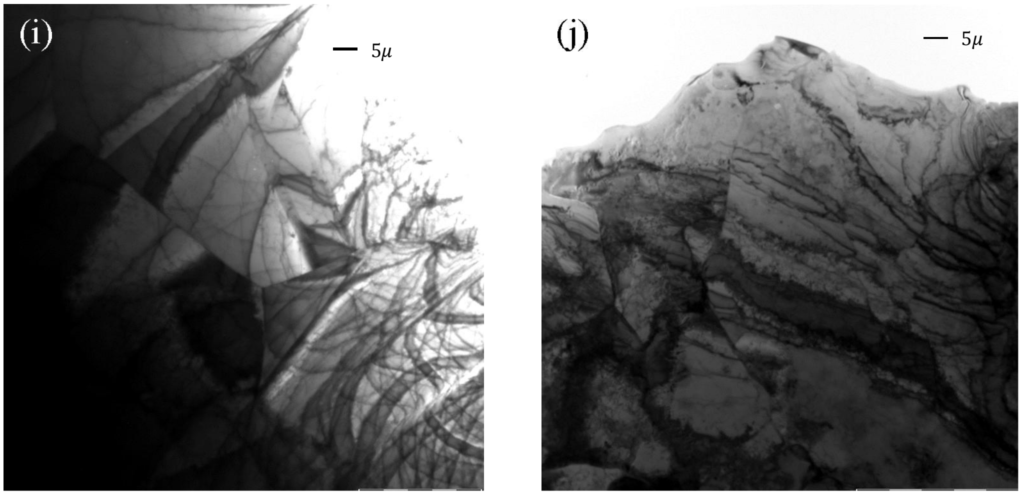

Figure 5.14: **TEM microstructures of 321 steel that was deformed according to Figure 5.12. The numbering from figures (b) to (j) is as shown in Figure 5.12 while the figure (a) is for the as received hot band specimen for 321 steel.**

5.7 SEM results

The two steels showed that the most prominent phases after solidification are austenite and delta ferrite. It was previously pointed out that the delta ferrite is more pronounced in 321 as compared to 304 and this can be seen in both normal optical and SEM micrographs. They appear as stringers both inter- and intra-granularly along the rolling direction. The possibility of formation of stringers of delta ferrite happens when the steel has high ratios of Cr / N_i and as well as high content of alloys/impurities such as sulphur and phosphorus [2], [110], [111]. The delta ferrite has a high solubility for sulphur which transforms to austenite upon cooling but sometimes not all of the ferrite transforms but creates an austenitic material that has tiny patches of residual delta ferrite which remain at room temperature and manifest itself as shown in the micrographs. It is also reported that sometimes this delta ferrite can transform to sigma phase which is a very brittle phase if heated above 550℃ for a long period of several hours, depending on the chromium level. This can be confirmed by the Thermo-Calc graphs presented earlier in section 4.10

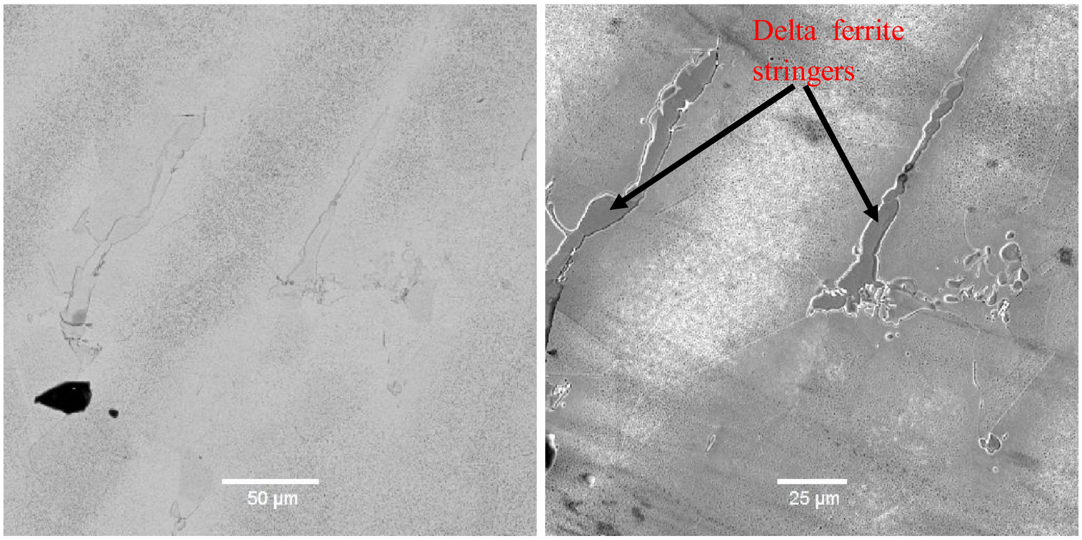

Figure 5.15: **As received SEM micrographs for AISI 304 stainless steele**

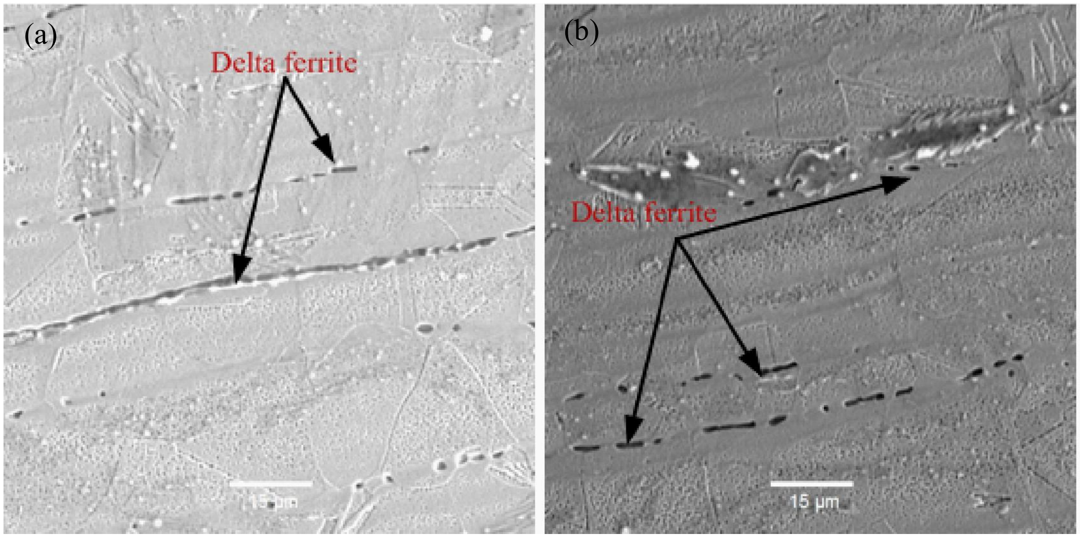

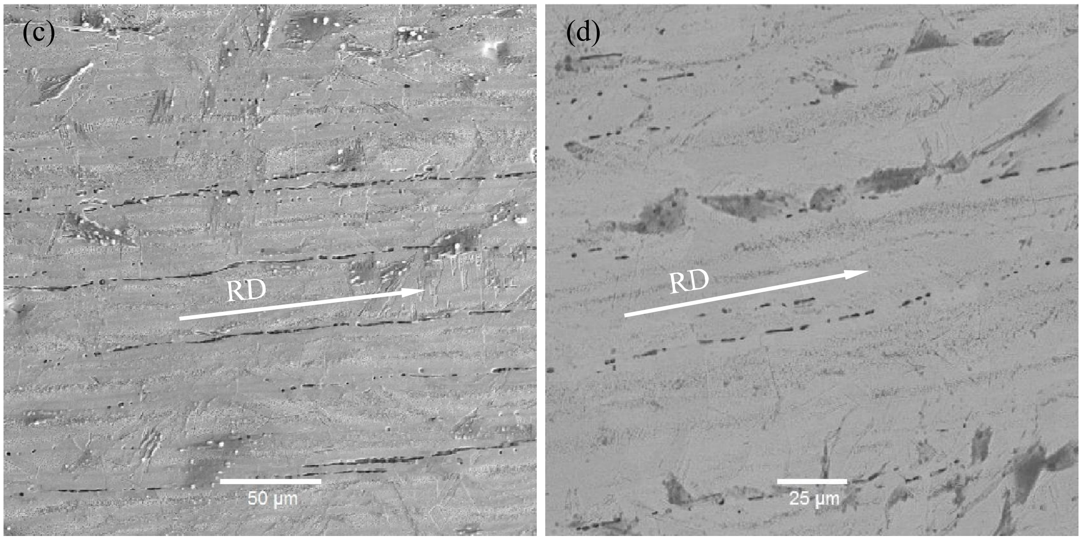

Figure 5.16: As received hot band SEM micrographs showing microstructures of the AISI 321 stainless steel. The black coloured 'stringers' are the delta ferrite structures running parallel to the rolling direction.

5.8 Normal optical microscopy results

Figure 5.17 and Figure 5.18 below show the microstructures of the respective steels 304 and 321 that were deformed in 9 passes while Figure 5.19 and Figure 5.20 show the same specimens that were deformed in 4 passes. The results confirm that the specimens with nine passes (the final deformation temperature was 800°C, with interpass time of 20 seconds and strain rate of 0.01s^{-1}) show pan-caked microstructures meaning that DRV had taken place while the specimens deformed in four passes (the final deformation temperature was 1050°C, with interpass time of 20 seconds and strain rate of 0.01s^{-1}) showed recrystallised grains which is the typical indication of the occurrence of DRX.

5.8.1 Nine pass' results

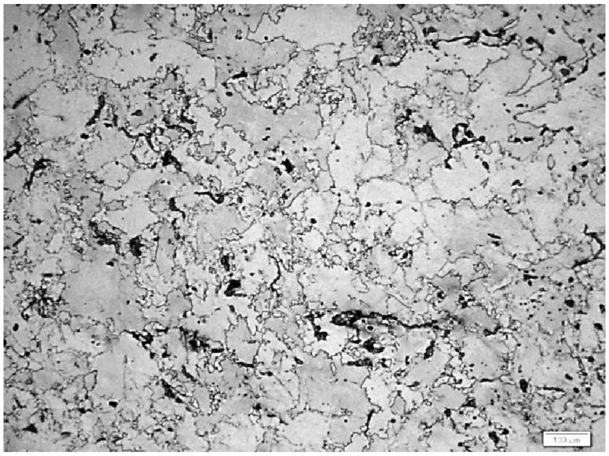

Figure 5.17: Optical micrograph of steel 304 after 9 passes at a strain rate of 0.01 s^{-1}. The final deformation temperature after the 9 passes was 800°C. Note the unrecrystallised microstructures. (the scale bar indicated on the figure is 100 μm).

Figure 5.18: Optical micrograph steel 321 after 9 passes at a strain rate of 0.01 s^{-1}. The final deformation temperature after the 9 passes was 800°C. Note the unrecrystallised microstructures. (the scale bar indicated on the figure is 100 μm).

5.8.2 *Four pass' results*

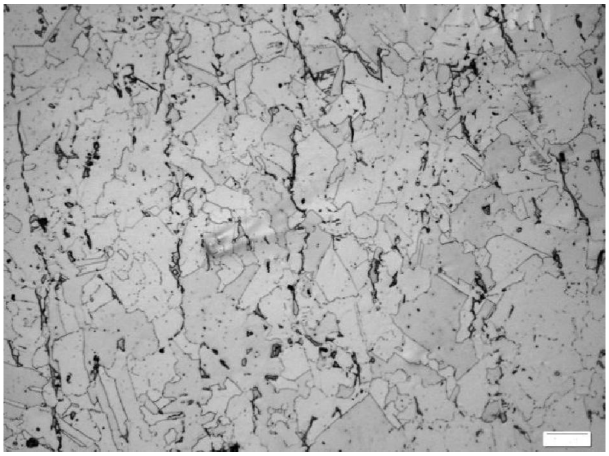

Figure 5.19: Optical micrograph of steel 304 after 4 passes at a strain rate of 0.01 s^{-1}. The final deformation temperature after the 9 passes was 1050°C. Note the recrystallised microstructures. (the scale bar indicated on the figure is 100 μm).

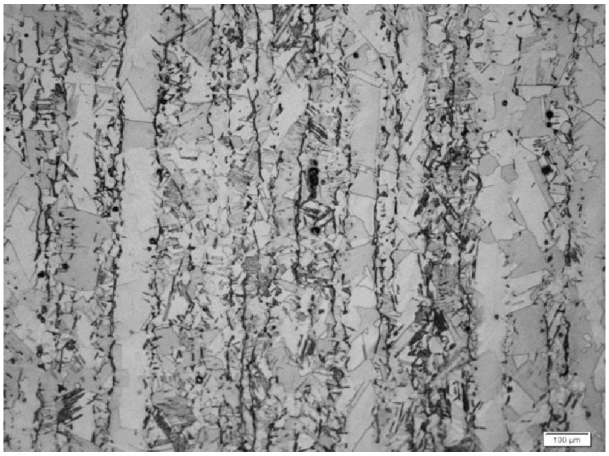

Figure 5.20: Optical micrograph of the steel 321 after 4 passes at a strain rate of 0.01 s^{-1}. The final deformation temperature after the 9 passes was 1050°C. (the scale bar indicated on the figure is 100 μm).

5.9 EBSD results

Figure 5.21 shows EBSD results which were done to verify the presence of DRX or DRV. The interpretation can be fully understood with the help of grain boundary character distribution (GBCD) plots that show the fraction of recrystallised and non recrystallised grains. Coincident site lattice (CSL) is a special grain boundary type in which there is good atomic matching across the boundary and a significant fraction of the atom sites are common to both crystals. The reciprocal of the ratio of atom sites which are common to both crystals (coincidence sites) to lattice sites is denoted by $\sum$. For example, in a twin boundary in fcc materials, one third of the lattice sites are common to both crystals and this is therefore a $\sum 3$ boundary [112].

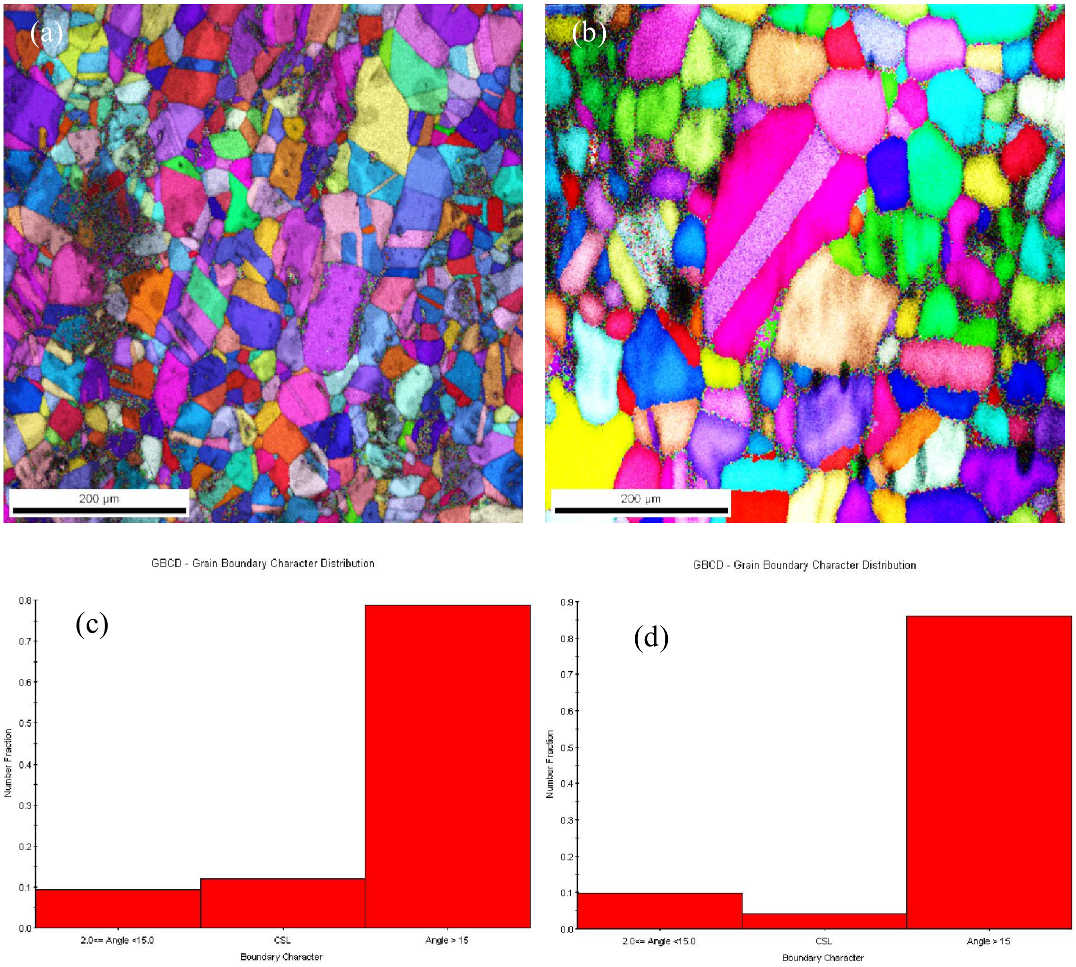

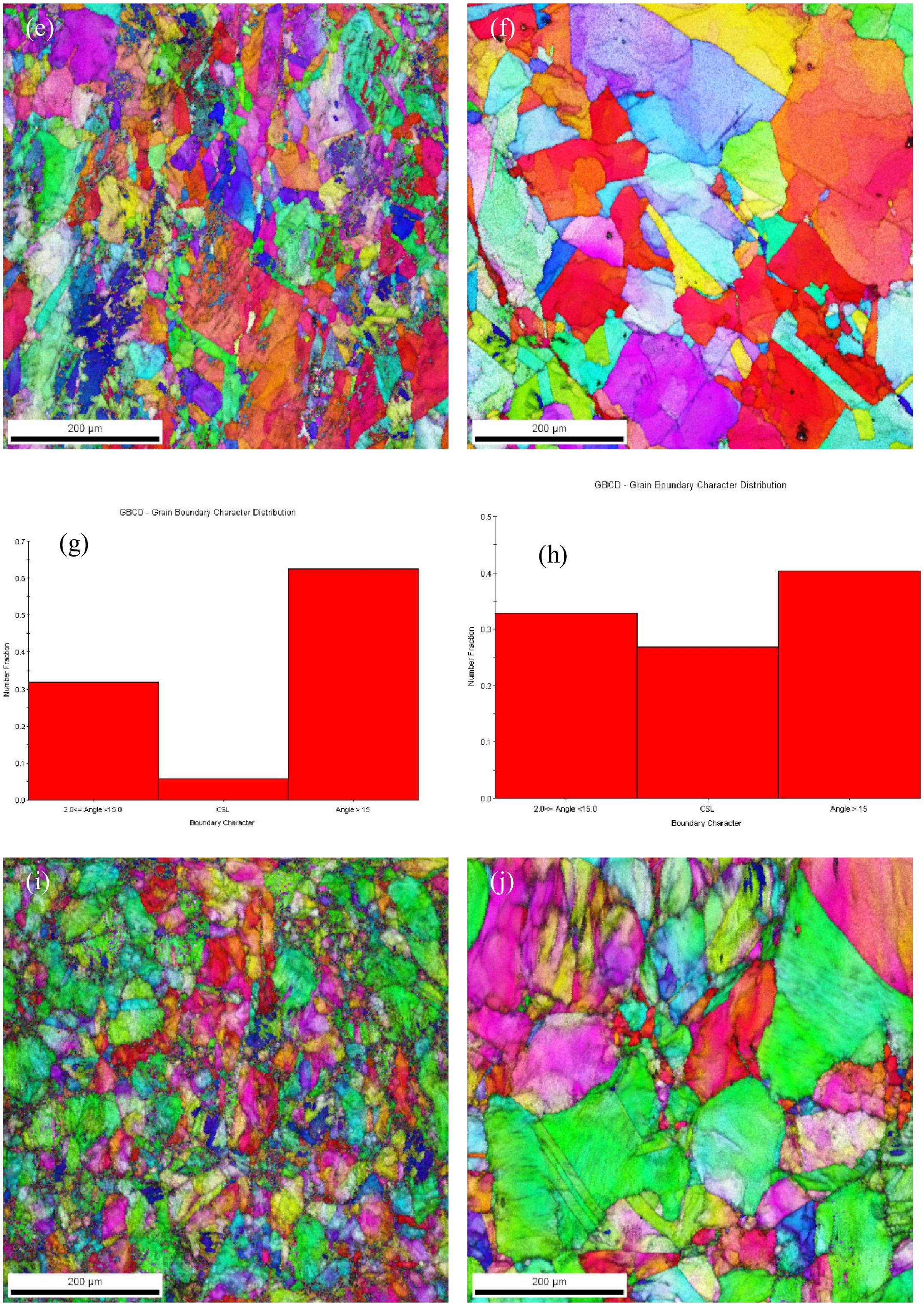
(e)
200 µm
(f)
200 µm
GBCD - Grain Boundary Character Distribution
(g)
Number Fraction
0.0
0.1
0.2
0.3
0.4
0.5
0.6
0.7
2.0<= Angle <15.0
CSL
Angle > 15
Boundary Character
GBCD - Grain Boundary Character Distribution
(h)
Number Fraction
0.0
0.1
0.2
0.3
0.4
0.5
2.0<= Angle <15.0
CSL
Angle > 15
Boundary Character
(i)
200 µm
(j)
200 µm

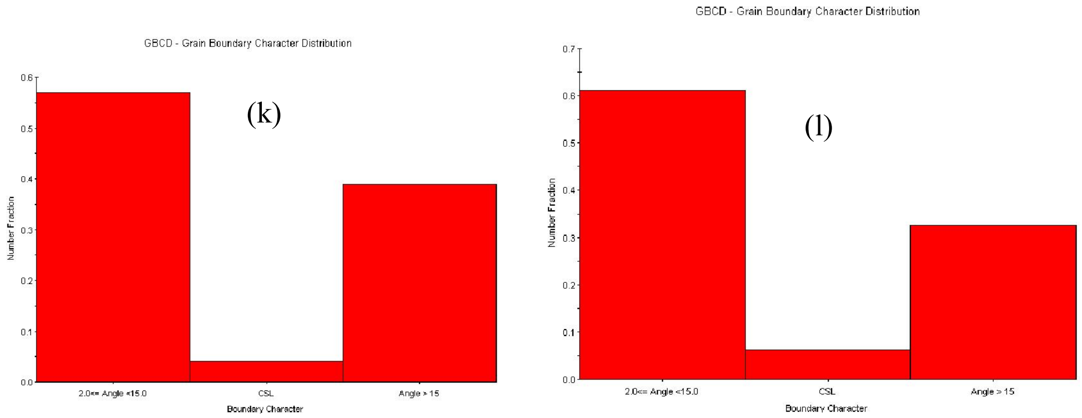

Figure 5.21: **EBSD orientation maps and grain boundary character distributions for (a) to (d) solution annealed (SA) and (e) to (h) 4 and (i) to (l) 9 multipass compression tests of 321 steel (left column) and 304 steel (right column).**

Figure 5.21 shows EBSD orientation maps and grain boundary character distributions of 321 steel and 304 steel as follows:

a. the quality map of 321 steel that was solution annealed at 1250°C for 5 min,
b. the quality map of 304 steel that was solution annealed at 1250°C for 5 min,
c. grain boundary character distribution for 321 steel that was solution annealed at 1250°C for 5 min,
d. grain boundary character distribution for 304 steel that was solution annealed at 1250°C for 5 min,
e. hot deformed 321 steel at 1050°C at a strain rate of 0.01/s,
f. hot deformed 304 steel at 1050°C at a strain rate of 0.01/s,
g. grain boundary character distribution for 321 steel that was hot deformed at 1050°C at a strain rate of 0.01,
h. grain boundary character distribution for 304 steel that was hot deformed at 1050°C at a strain rate of 0.01,
i. hot deformed 321 steel at 800°C at a strain rate of 0.01/s,
j. hot deformed 304 steel at 800°C at a strain rate of 0.01/s,
k. grain boundary character distribution for 321 steel that was hot deformed at 800°C at a strain rate of 0.01, and
l. grain boundary character distribution for 304 steel that was hot deformed at 800°C at a strain rate of 0.01

From the grain boundary character distributions of 321 and 304 steels that were solution annealed at 1250°C in Figure 5.21(a) and Figure 5.21 (b) respectively in which it can be seen that 321 steel is slightly less recrystallised as compared to 304 steel. This observation is taken from the fact that if there are more high angle grain boundaries, the structure is recrystallised while if there are more low angle boundaries, it means that the structure is recovered. The 321 steel has more CSL boundaries which may be attributed to the twins structure in the quality image map. These quality image maps in Figure 5.21 (e), (f), (i) and (j) are for specimens that were deformed at 1050°C and 800°C respectively at a a strain rate of $0.001s^{-1}$. As expected the specimen that was deformed at 800°C has slightly more low angle grain boundaries in comparison to the one deformed at 1050℃ which has more high angle grain boundaries. The GBCD plots show that the two specimens still have recrystallised structures owing to the slow strain rate that was used even though the respective deformation temperatures were low.

From the GBCD plots, the EBSD results tell a much more detailed story than using the stress-strain graphs to distinguish DRX from DRV as the dominant softening mechanism. In GBCD plots, the extent of DRX and DRV can be fully appreciated as they are displayed as fractions. Using stress-strain graphs alone is not sufficient as it is often difficult to tell how much DRX and DRV has taken place.

CHAPTER 6: CONSTITUTIVE CONSTANTS

6.1 Introduction

In this chapter all the results that were found through the use of modelling equations will be analysed further. Sections 2.3 and 2.4 have been used in the modelling simulations and the results will be presented graphically in this chapter. As mentioned, there are many techniques which can be used to identify possible linear relationships between several quantitative constants and variables that mainly come in forms of equations. For instance, these constants and variables may be completely independent from each other while sometimes there may be a linear relationship between two or more independent input variables. In some cases, the relationship is not merely linear but nonlinear which is usually represented by a polynomial of some degree (order). The results as presented in the graphs, depict the exact relationship that was considered case by case. In the range between these extremes, one can have different degrees of correlation between variables and constants. In some cases, when analysing the data it is found that some constants and variables are dependent upon more than one input constant or variable. The boundary conditions and the assumptions that are made, help to simplify these apparent complicated relationships sufficiently enough to draw meaningful conclusions.

6.2 Constitutive constants for AISI 321

Using equations [3-4] through to equation [3-18], the following graphs were generated:

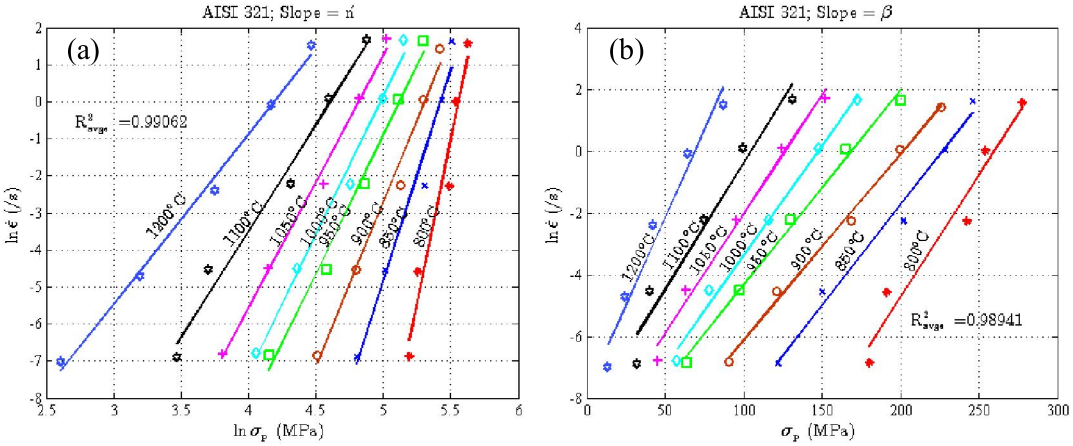

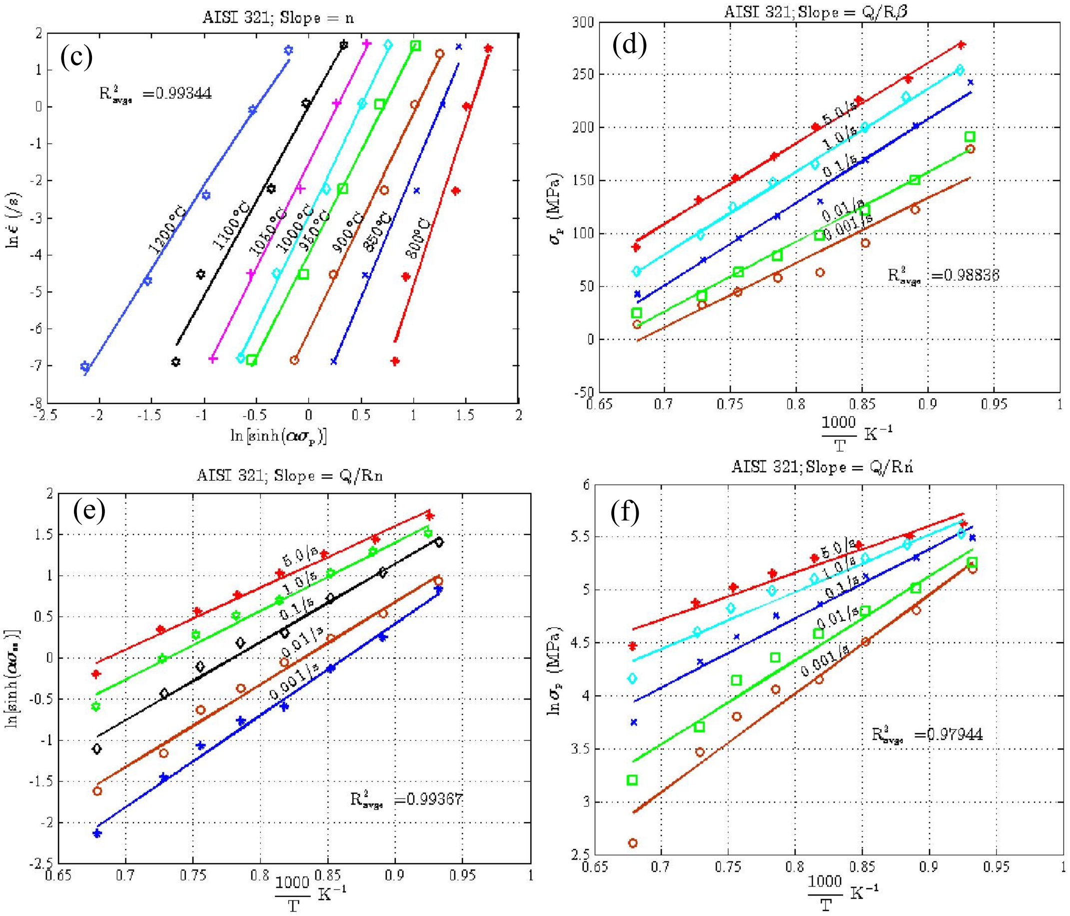

Figure 6.1: **Plots used for the determination of n', β, n and Q values for AISI 321 steel**

Figure 6.1(a) was plotted using equation [3-10] where the deformation temperatures are assumed constant while the strain rate is varied. The slope of the plotted graphs gives the constant n'. This constant will be used later to find the strain hardening exponent n. From this plot n' was found to be 8.77. Using equation [3-12], plots as shown in Figure 6.1 (b) were generated of which the slope of the plots gives β and it was found to be 0.0764. Using these two values, the average value for α was found to be 0.009 MPa^{-1}. As for Figure 6.1 (c), equation [3-17] was used by also keeping the deformation temperature constant and the slope of these plots give the value of n. There are several ways to find the value of n and all the ways were explored out of which the average value of n was found to be 6.1 and the value of A_3 was 9.76×10^{17} s^{-1} MPa^{-1} for steel 321.

The other method of finding n is by plotting equation [3-8], i.e. the plot of lnZ against $ln\left[sinh\left(\alpha\sigma_p\right)\right]$ as shown in Figure 6.1(d) and using the Q value from Figures 6.2 (f) and (d) which was found to be 465 kJ/mol.

The DRX data was isolated from the DRV data and the former was used to plot $ln\varepsilon_p$ against lnZ in order to obtain the Z exponent q and the intercept $A_1 d_o^m$ and d were found to be 0.13

and 1.9×10^{-3} respectively, see Figure 6.1(c). For 321, equation [3-8] can now be rewritten in full as:

$$Z_{321} = \dot{\varepsilon} e^{\frac{465\,000}{8.314T_d}} = 9.76 \times 10^{17} \times \left[sinh\left(0.0087\sigma_p\right)\right]^{6.1} \qquad [6\text{-}1]$$

When all the data points are plotted using equation [3-5], the profile of the plots for $ln\varepsilon_p$ against lnZ are shown in Figure 6.2(a) below. It was observed that there seem to be two regions, i.e. one region is for DRX and the other region is for DRV. These two regions are approximated by the straight lines as shown in Figure 6.2(b) with the horizontal line depicting the DRV region while the slanting line depicting the DRX region. Point of interest is where the circle is placed as it represents a transition from DRX to DRV. The transition point means that DRV and its associated material properties will result, if hot rolling is done where $lnZ \geq 44$ and that there will be a mixture of DRX and DRV regions if hot rolling is to be done where $40 \leq lnZ \leq 44$. If rolling is done where $lnZ \leq 40$, DRX and its associated material properties will result.

So far, this transition region can be viewed as a $f\,(T_d, \varepsilon)$ as the calculations of lnZ were based on these parameters.

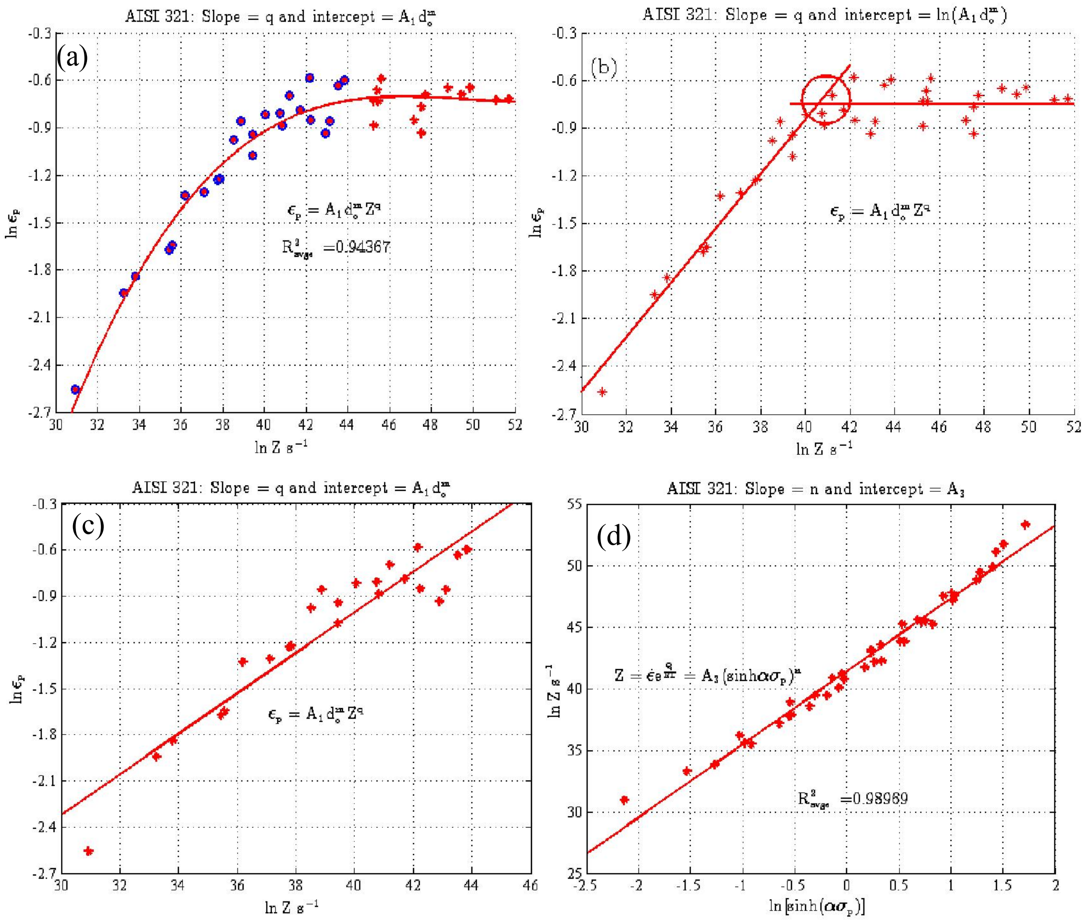

Figure 6.2: **Plots used for the determination of n, $(A_1 d_o^m)$ and A_3 values for AISI 321 steel**

6.2.1 *Modelling the ϵ_c/ϵ_p and σ_c/σ_p ratios for AISI 321*

The critical strain and critical stress for the initiation of DRX can be analysed using either direct microstructural observations or from analysis of the flow stress curve profiles. The basic principle is that for DRX to be initiated, the local dislocation density must be high enough to allow new grains to nucleate and grow during deformation. The point at which this occurs corresponds to the critical strain (ε_c). It has been shown [54] that typically the initiation of DRX is preceded by growing fluctuations of grain boundary shape (serrations and bulges develop) prior to the new grains forming along these grain boundaries. Once the grain boundaries have been consumed by these 'new' grains the recrystallisation process will continue via nucleation at the interface between the recrystallised and non–recrystallised material. These two parameters (critical strain and stress) are significant for the prediction of the initiation of DRX as the operating restoration mechanism in hot working processes. In order to avoid any ambiguities, only flow stress profiles that clearly showed occurrences of DRX, i.e. flow stress profiles that show a peak first before lowering to the steady state, were used to find the relationship between critical and peak stress as well as the relationship between critical and peak strain. Because of "noise" in the signal, the data was first filtered and then approximated by a 9th order polynomial, see the dotted line b as superimposed in Figure 6.23.

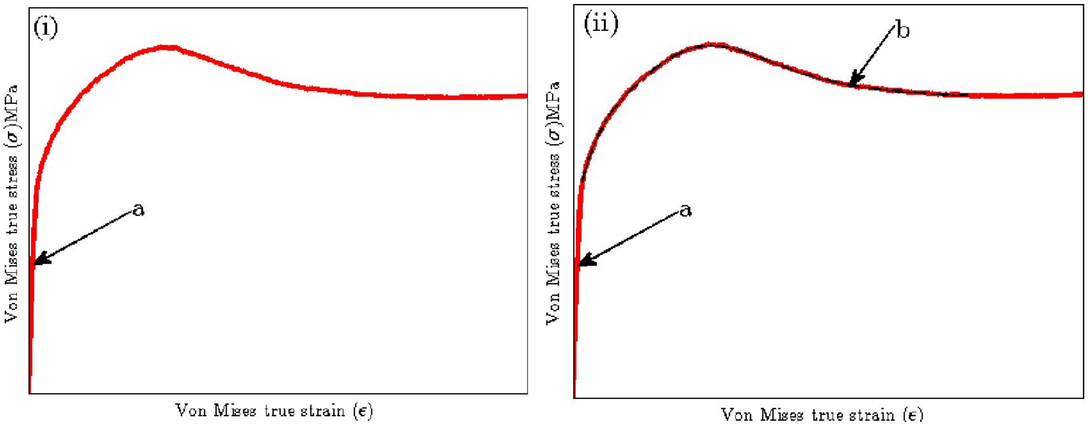

Figure 6.3: Von Mises true stress-strain curves showing (i) original stress – strain flow curves indicated by line a and (ii) the 9th order approximated polynomial curve indicated by line b. There is almost no difference between the approximated and the actual flow curves if higher order polynomials are considered. These profile curves are for AISI 321 stainless steel after deformation at a temperature of 1050℃ and strain rate of $0.01/s$.

The 9th order polynomial function which was used in all true stress-true strain curves was differentiated and the results are shown in Figure 6.4 below where the work hardening rate (θ) was plotted against the Von Mises stress (σ) and $ln\theta$ was plotted against the Von Mises strain (ε). The critical stress and strain values were then read off as indicated on the graphs on the points of inflection.

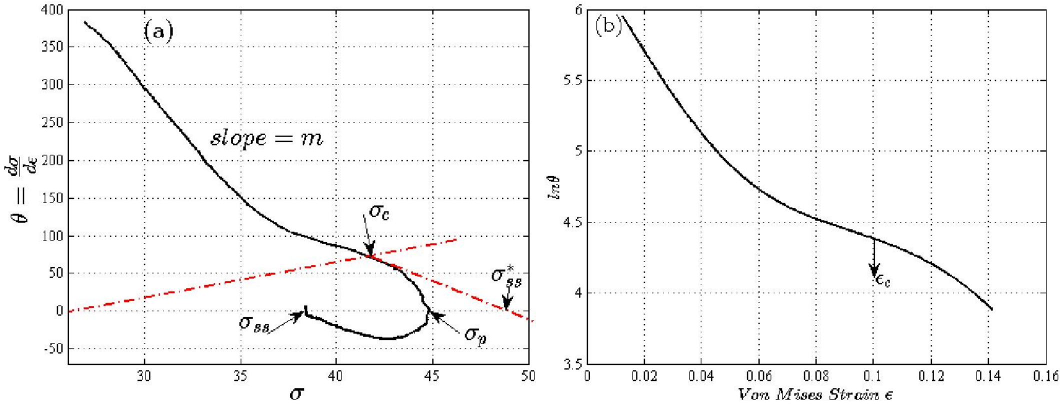

Figure 6.4: **Stain hardening rate plots indicating (a) how to find the critical stresses and (b) how to find the critical strain values for AISI 321 stainless steel.**

Only the profiles that depicted the occurrence of DRX were isolated and analysed and the procedures as explained above were performed on each and every one of them. Presented below are the results of the θ vs σ and $ln\theta$ vs ε of DRX flow curve profiles for the steel 321.

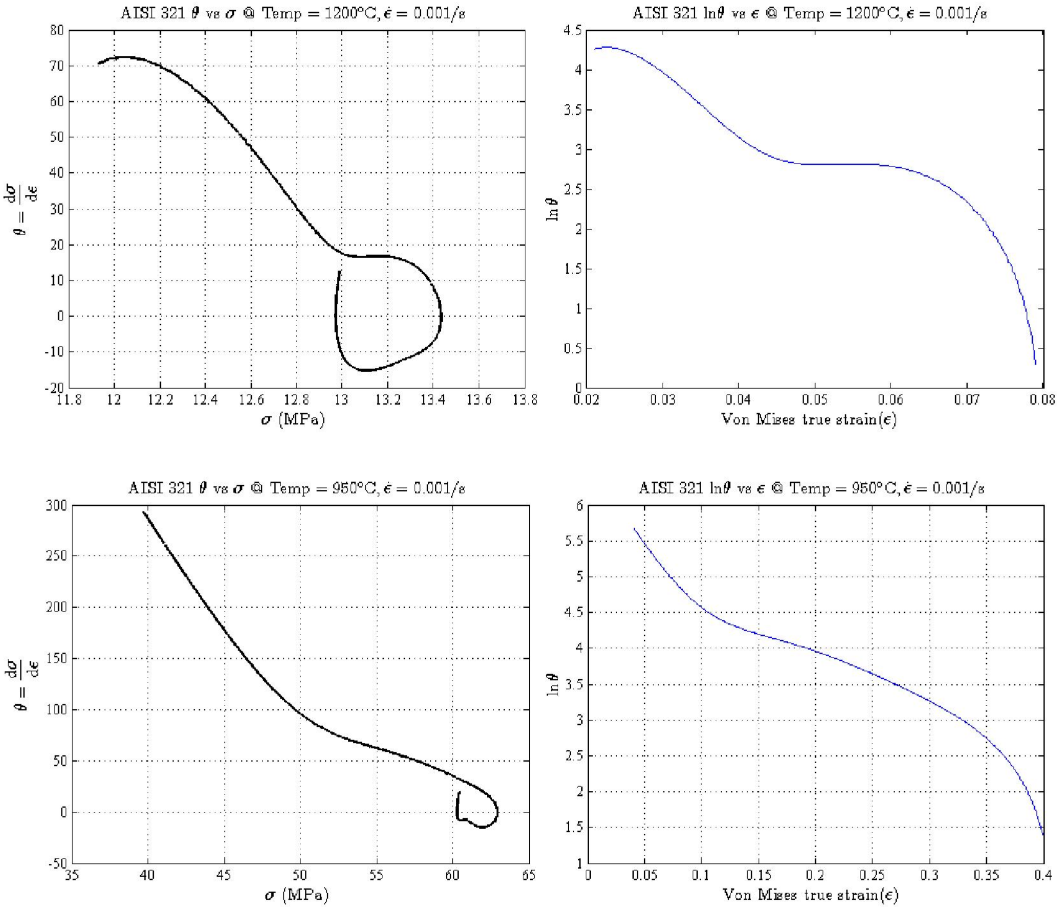

Figure 6.5: **Stain hardening rate θ vs σ(left) $ln\theta$ vs ε(right) used to find σ_c and ε_c for AISI 321 stainless steel.**

The σ_c and ε_c values collected were plotted together with their respective σ_p and ε_p values against lnZ as shown in Figure 6.6 and the following relationships were drawn:

$$\sigma_c = 0.88\sigma_p \tag{6-2}$$

$$\varepsilon_c = 0.69\varepsilon_p \tag{6-3}$$

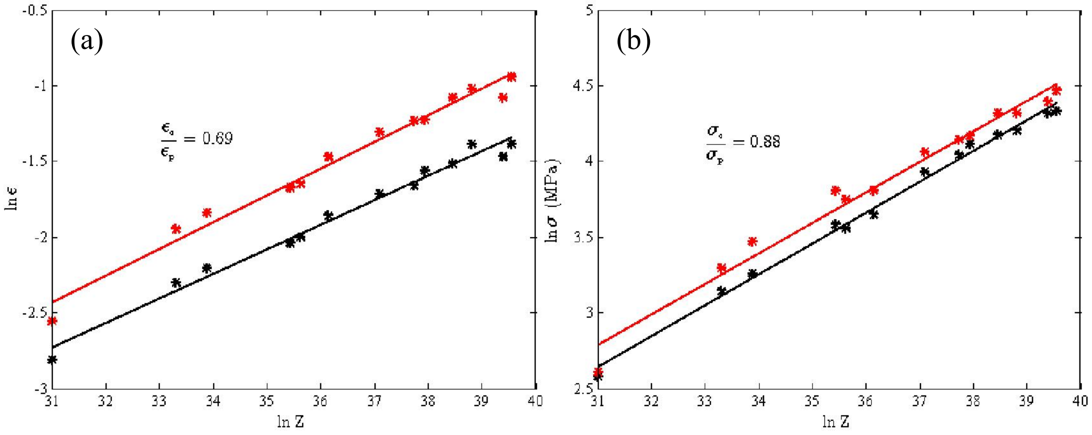

Figure 6.6: Plots of (a) lnε against lnZ and (b) lnσ against lnZ indicating how the relationship between ε_c and ε_p (left) and between σ_c and σ_p (right) were found for AISI 321 stainless steel.

6.3 Constitutive constants for AISI 304

The process of obtaining the constants for AISI 304 stainless steel followed the same procedures as above for AISI 321 stainless steel. Below are the graphs that depict the relationships used for finding the constants.

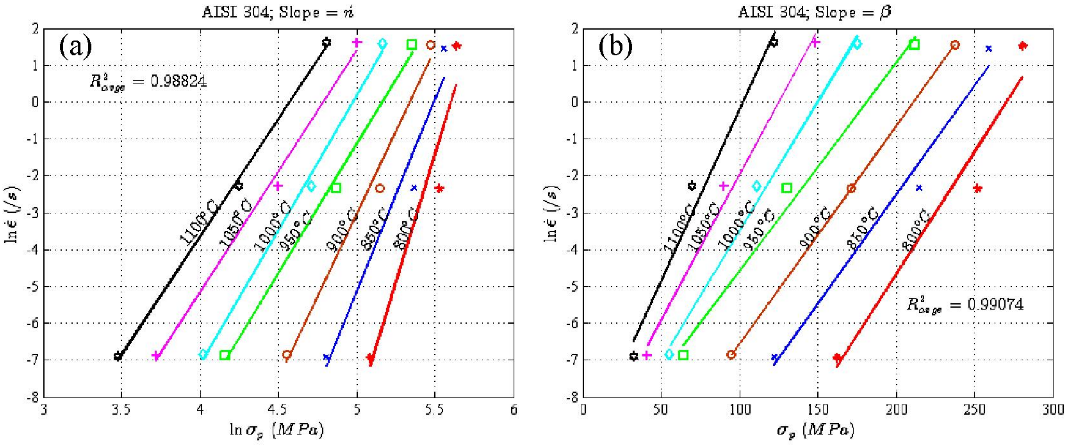

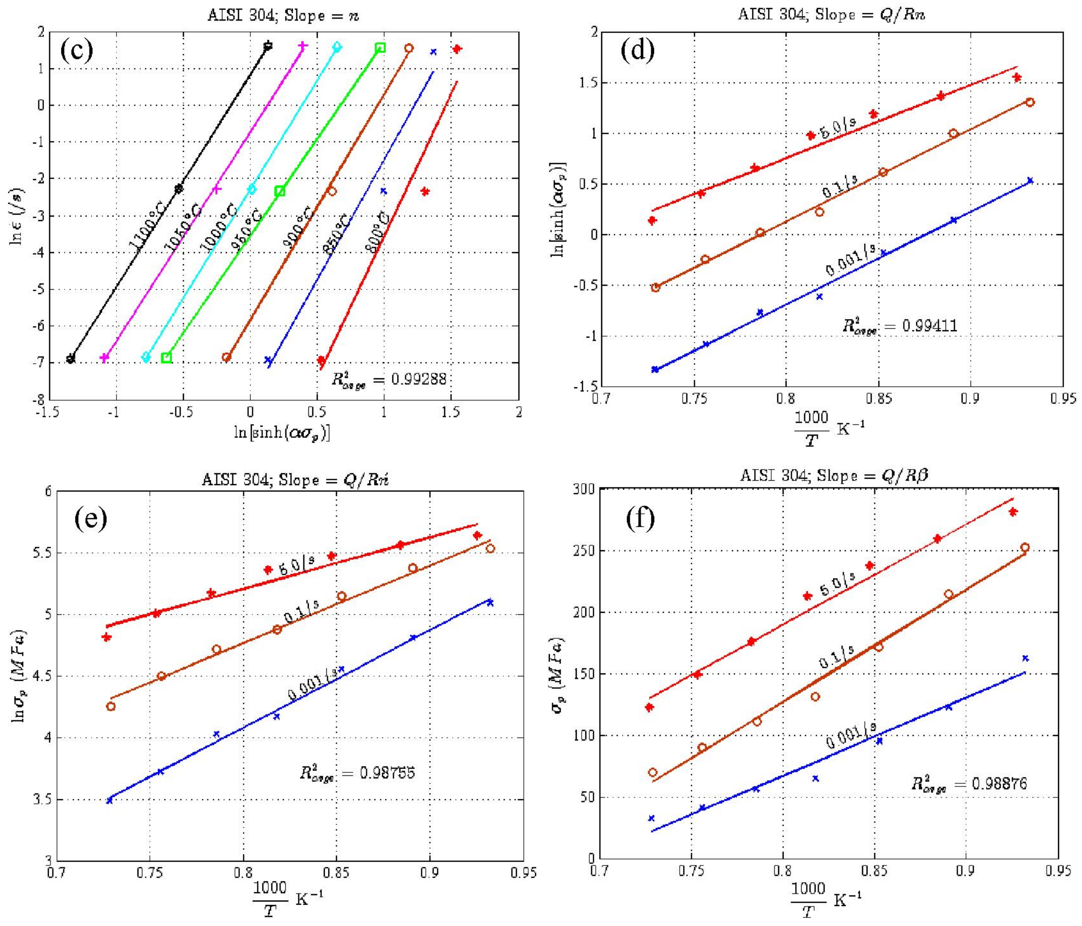

Figure 6.7: **Plots used for the determination of n', β, n and Q values for AISI 304 steel**

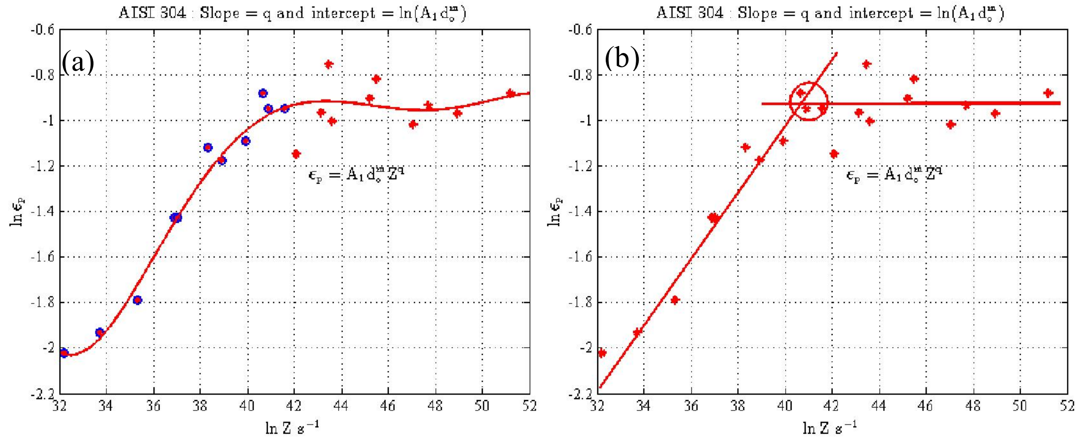

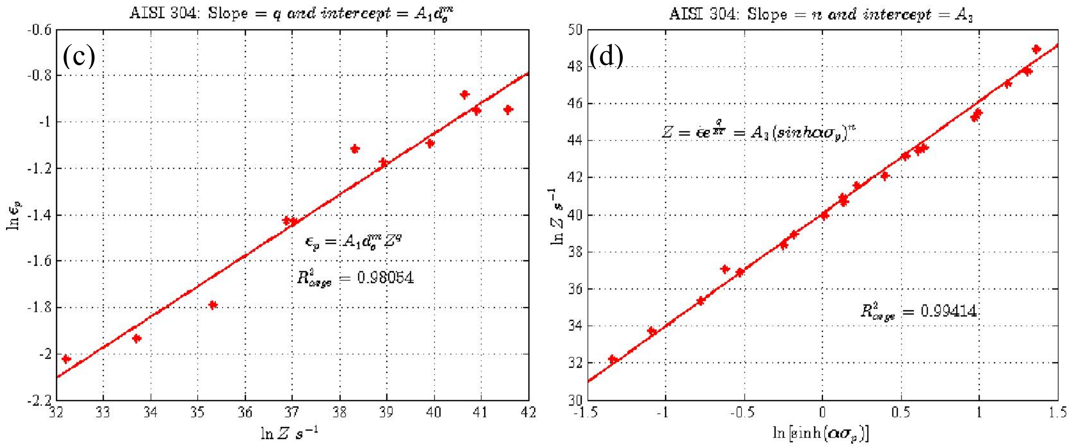

Figure 6.8: **Plots used for the determination of n, $(A_1 d_o^m)$ and A_3 values for AISI 304 steel**

6.3.1 Modelling the ϵ_c/ϵ_p and σ_c/σ_p ratios for AISI 304

The same procedure as outlined for 321 steel was applied to 304 steel and below are the results.

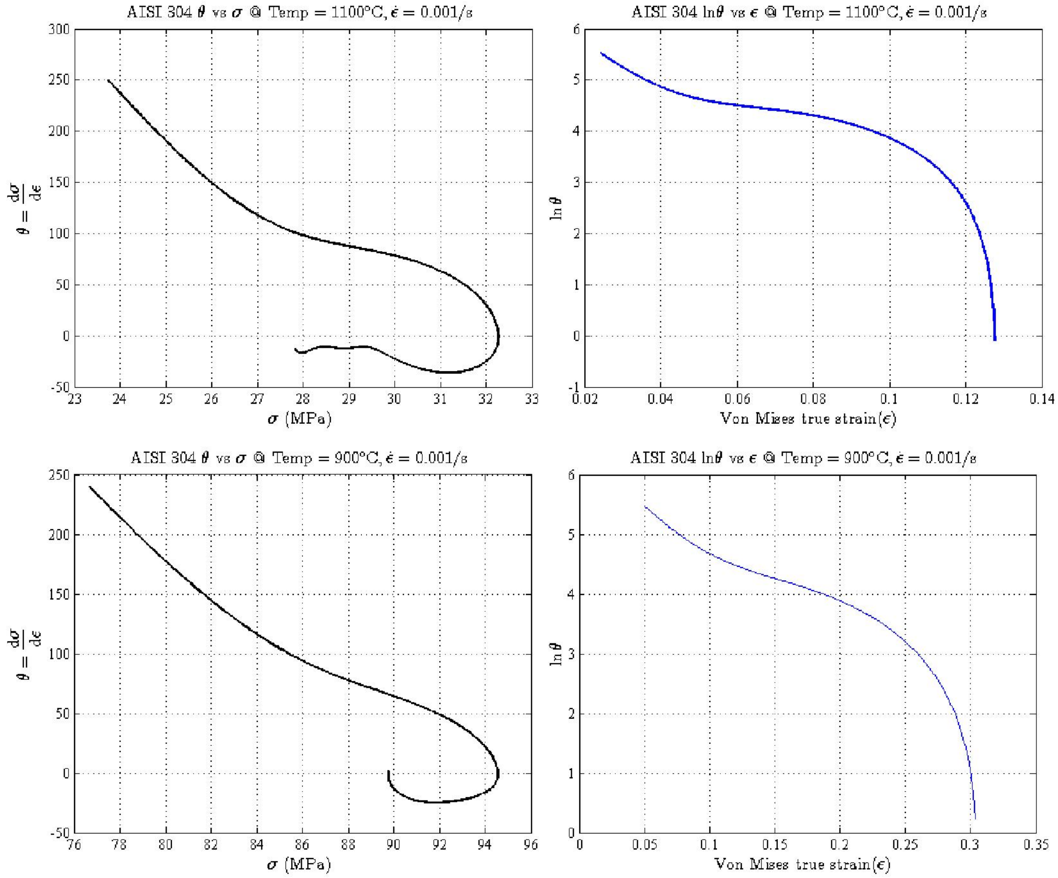

Figure 6.9: **Stain hardening rate θ vs σ(left) $ln\theta$ vs ε(right) used to get σ_c and ε_c for AISI 304 stainless steel**

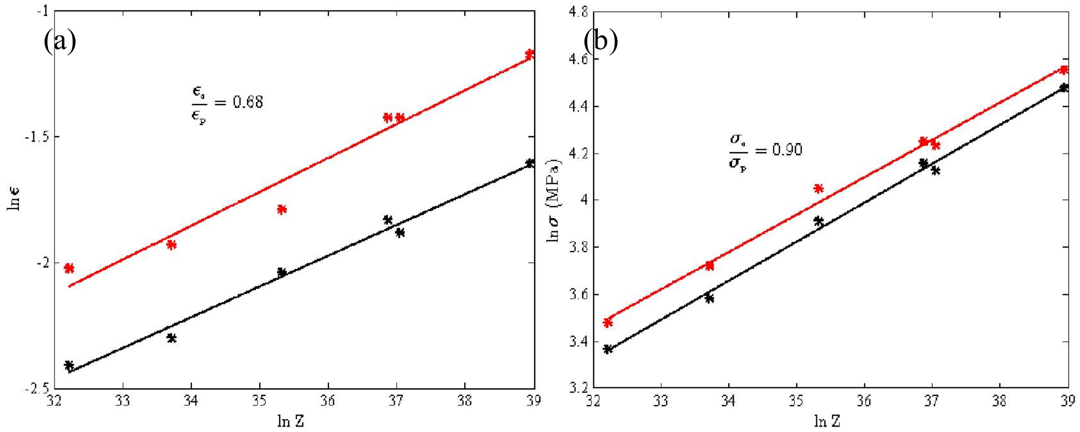

Figure 6.10: **Plots of (a) lnε against lnZ and (b) lnσ against lnZ indicating how the relationship between (a) ε_c and ε_p and (b) between σ_c and σ_p were found for AISI 304 stainless steel.**

The following is a summary of constitutive constants for 304: $n' = 8.6563$, $\beta = 0.0690$, $\alpha = 0.008$, Q = 446 kJ/mol, $A_1 d_o^m = 1.8 \times 10^{-3}$, $A_3 = 2.14 \times 10^{17}$ MPa$^{-1}s^{-1}$, $q = 0.13$, $n = 6.1$, $\sigma_c = 0.9\sigma_p$, $\varepsilon_c = 0.68\varepsilon_p$, and, therefore, the full equation for steel 304 becomes:

$$Z_{304} = \dot{\varepsilon} e^{\frac{446\ 000}{8.314 T_d}} = 2.14 \times 10^{17} \times \left[\sinh\left(0.008\sigma_p\right)\right]^{6.1}$$

CHAPTER 7: DISCUSSION

7.1 Introduction

This chapter discusses the thermomechanical simulation and modelling results that have been presented in the previous chapters. The differences or similarities between the two steels under study will be highlighted through their constants and their flow stress profiles given the same deformation conditions. It is worthwhile recognising again that carbon is in solution in AISI 304 stainless steel during hot working while carbon is tied up by titanium in AISI 321 in the form of carbides and these carbides can be as seen in Figure 7.1 and similar Ti(CN) particles were also observed in as quenched 321 steel.

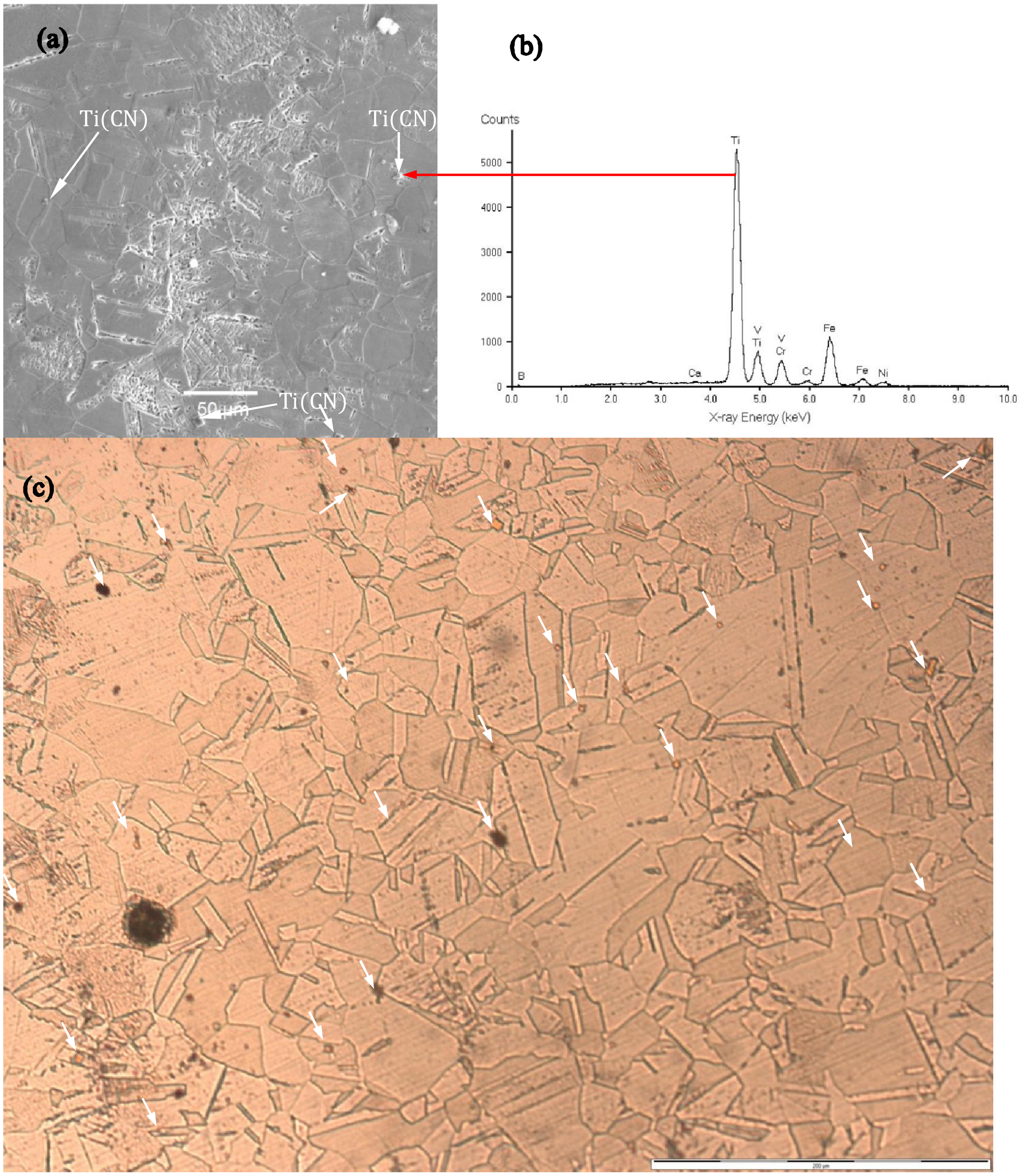

Figure 7.1: Figure of the Ti(CN) carbides in 321 steel: (a) is the SEM micrograph and (b) is the EDS spectrum of the Ti(CN) carbides and in (c) the arrows point to the Ti(CN) in the as received 321 steel.

The general observation on the flow stress curves was that all these curves show initial work hardening which was followed by either DRX or DRV. Some deformation conditions exhibited a clear peak stress indicative of the occurrence dynamic recrystallization. These peaks were mainly visible when the deformations were done at high temperature and low strain rate combinations. The majority of the flow curves that showed the occurrence of DRX exhibited a single peak except those that were carried out at 1200°C and a strain rate of $0.001/s$, i.e. at high temperature and low strain rate. Multiple peaks occur if $\mathrm{d_o} > 2\mathrm{d_{DRX}}$ where $\mathrm{d_{DRX}}$ is the dynamically recrystallised grain size and $\mathrm{d_o}$ is the initial grain size and this generally occurs at high temperatures and slow strain rates [113].

It is evident from the results presented that DRX takes place in both materials under the deformation conditions where the critical lnZ value for both steels is about 41 (with Z in s^{-1}). Below this critical value, the operating softening mechanism is DRX while above this value, the dominant softening mechanism is DRV. The Z parameter is related to the dislocation density through the flow stress or strain rate equations such as $\sigma = c\mathrm{G}\, b\sqrt{\mathrm{N_d}}$ and $\dot{\varepsilon} = b\mathrm{N_d}\bar{v}$ respectively where c is a constant of the order of 0.5 [114], G is the shear elastic modulus, b is the burgers vector, $\mathrm{N_d}$ is the dislocation density and $\bar{v}$ is the average mobile dislocation velocity while the rate of recovery is directly proportional to the dislocation density [56]. As the Z parameter increases (higher strain rates and lower deformation temperatures), the dislocation density also increases and this causes the peak strain to rise until a critical value is reached as shown in Figure 6.2 (b) and Figure 6.8(b). At this critical point, the subgrain structure reaches a steady state and the dislocation density remains constant [56]. The strength of the material is bound to increase because a larger stress will be required to move these dislocations through a matrix already containing many other dislocations. As seen in Figure 6.2 (b) and Figure 6.8(b), a further increase in the Z parameter has no influence on the peak strain because of the fact that the mobile dislocation density has reached a steady state.

7.2 Marked differences between 321 and 304 steels

The differences in hot working constants found between these two steels are most significant in the activation energies (465000 J/mol for 321 versus 446000 J/mol for 304) and the structure factors $\mathrm{A_3}$ (9.76×10^{17} $\mathrm{MPa}^{-1}s^{-1}$ for 321 versus 2.4×10^{17} $\mathrm{MPa}^{-1}s^{-1}$ for 304) while all other constants show relatively minor differences if at all. It can be seen from these results that the $\mathrm{A_3}$ for 321 steel is about four times higher than the $\mathrm{A_3}$ for 304 steel. Wherefrom do these differences arise and how significant are they in terms of hot working characteristics? Are they fundamentally different or are they caused by minor differences in chemical composition relevant only to these two steels?

7.3 Effect of deformation conditions and alloying elements on DRV and DRX

There are two factors that can affect dynamic recrystallisation which are, firstly, deformation conditions because it is a thermally activated process and secondly, the alloying elements. It can be seen in Figure 5.2 and Figure 5.3 that DRX can be retarded by either increasing the strain rate or by reducing the deformation temperature. But deformation conditions should not have an effect on the activation energy if the low stacking fault energies of both of these steels restrict cross slipping of screw dislocations during recovery which is then dominated by climb of edge dislocations. Work hardening behaviour of austenitic steels is related mainly to their stacking fault energy (SFE) since the lower the SFE the higher the work hardening rate. The SFE for 321 is about $20\ \mathrm{mJ/m^2}$ while that of 304 is about $21\ \mathrm{mJ/m^2}$ [115] and these two materials are both classified as low stacking fault energy steels. The low SFE of about 20 mJ/m^2 will lead to widely extended dislocations which makes cross slipping difficult. If DRX takes place by self-diffusion, DRV can only have the “same relative” Q value for both steels if DRV occurs primarily by climb of edge dislocations and not by cross slipping of screw dislocations.

On the other hand it is known that some alloying elements have retarding effects on DRX while others have retarding effects on DRV [116] and this makes it very difficult to conclude for certain what the net effect of any differences in the alloying elements may be. These may have an effect of solute drag on the movement of dislocations and grain boundary mobility which affects the ease of nucleating new grains. In this case, the contributions are potentially arising from the differences in concentration between the two steels in their solute content of C, N, Cr, Si, Mn, Ti, Al and Ni. The nucleation rate of new DRX grains is *inter alia* a function of the rate of self-diffusion and the rate of nucleation will, therefore, become lower with a higher activation energy at constant temperatures. Furthermore, alloying elements may also have retarding effects on DRX by increasing the activation energy of deformation [117]. These are mainly the alloying elements that have a similar atomic radius to Fe such as Cr, Mn, Si, Al and Ni which occupy substitutional sites in austenite. Retardation of DRX comes from the effect of solute particles that provide solute drag which affects the mobility of the migrating grain boundaries.

Those elements that occupy interstitial sites, however, have a tendency to lower the activation energy and this accelerates the initiation of dynamic recrystallisation [118][38]. This was confirmed in this study, for instance at a value of Z = 40 in figure 6.2(b) and 6.8(b), the critical strain ε_c for DRX in steel 304 was found to be 0.24 while that for the steel 321 at the same value of Z was 0.31. The N and C in solution during hot working in the steel 304 thereby have accelerated the onset of DRX if compared to steel 321 where the N and C is bound within the Ti(CN).

7.4 Effect of δ −ferrite on the activation energy Q for DRX

Concerning the differences in activation energy between 321 and 304, it has been found by McQueen and co-workers [119] that the peak strain, flow stress and activation energy can be raised by the amount of retained δ −ferrite present in the steel which was found to be higher in the steel 321. It is also mentioned that the amount of high temperature carbides and carbonitrides such as Ti(CN)/TiC can raise the activation energy of hot working mainly because the carbon and nitrogen which are responsible for reducing Q, are tied up in the carbonitride. This can be verified by the two steels studied here in that Q is lower in 304 steel because it has free nitrogen and carbon in solution as compared to 321 steel which has carbon and nitrogen tied up by titanium. Chromium and titanium have the tendency to promote $\delta -$ferrite formation and it is suggested that in order to avert this, nickel additions should be increased as the presence of $\delta -$ferrite greatly impairs the hot workability of steels and the strength of austenite [120]. However the contributions of other alloying elements should be taken into account depending upon whether they are austenite or ferrite formers as they will have a positive or negative effect on the $\delta -$ ferrite formation. The adverse effect of $\delta -$ferrite in hot working is attributed to a maximum alpha/gamma interfacial area at which voids may nucleate [120].

Others [119][121] have shown that Q is generally a function of the chemical composition of the alloy and that it increases with alloy content save for carbon and nitrogen. Since n is the same for both steels under study, the change in A_3 can be said to arise partly from the change in Q which is affected by parameters such as the chemical composition, the dislocation density, the grain size, and the delta-ferrite content. This may be seen in Figure 6.2(d)'s intercept, which represents "$\ln A_3$" as a change in Q raises or lowers the trend line, hence the value for A_3 will also be higher or lower at constant strain rate. The general observation from the literature [122] on the structure factor A_3 of steels is that it is proportional to the activation energy of hot working, i.e. when Q is high, A_3 is also high and it is also a function of the chemistry of the material and other factors as pointed out before. This can be corroborated by the findings of Medina and Hernandez [121] who studied a number of materials and came to the same conclusion. Therefore, A_3 as a constant has no simple physical meaning [123] but it is a function of the strain rate, but as the name suggests, A_3 is also a function of the structure of the material itself. Therefore, it can be concluded from the results obtained in this study that this observation is also obeyed qualitatively.

No direct correlation has been observed between α and Q from the literature and neither can it be related to the chemistry but it has been stated to be material specific [124]. Finally, it was found that the values of n' increased with a decrease in deformation temperature, confirming that the power law breaks down, resulting in an increase in flow stress. This is clearly seen from Figure 6.1(a) that the lines drawn are not necessarily parallel to each other; mainly on the two extremes (very high temperatures and very low temperatures). This fact is attributed to the exponential dependence of strain rate on the applied stress [125]. A trend in other material constants was similar in that they did not remain constant over the whole range of deformation conditions. Observation from these graphs, shows this breakdown to take place at about 900°C.

7.5 Summary of the characteristic constants

The first primary objective was to characterise the hot working process through Gleeble thermomechanical simulations in order to determine the hot working constants. The reason was to investigate the hot working characteristics of type AISI 321 steel so as to improve on its room temperature strength with AISI 304 used as a benchmark. Therefore, the hot working constants of types 304 stainless steel and 321 were compared through Gleeble simulated thermomechanical processing where the temperature was varied between 800°C and 1200°C and the strain rate between 0.001/s and 5/s. It was found that the constants for the sine–hyperbolic equation for hot working are as summarised and shown in Table 7.1

Table 7.1: A summary of the characteristic constants.

Cst	AISI 304	AISI 321
n'	8.66	8.77
β	0.0690	0.0764
α	0.008	0.009
A_3	$2.14 \times 10^{17}\ \mathrm{MPa^{-1}s^{-1}}$	$9.76 \times 10^{17}\ \mathrm{MPa^{-1}s^{-1}}$
$A_1 d_o^m$	1.8×10^{-3}	1.9×10^{-3}
Q	446 kJ/mol	465 kJ/md
q	0.13	0.13
n	6.1	6.1
σ_c	$0.9\sigma_p$	$0.88\sigma_p$
ε_c	$0.68\varepsilon_p$	$0.69\varepsilon_p$

Overall, therefore, the results presented in Table 7.1 are in general agreement with what is reported in the literature [7] [119][126] and more specifically in agreement with what others have found in austenitic stainless steels [33]. The values for Q, A_3, α, and n from Table 7.1 will enable one to predict the maximum deformation resistance during hot rolling through the temperature compensated strain rate parameter Z for these materials. Hence, the final respective Z parameter for the two steels can indeed be written as:

$$Z_{304} = \dot{\varepsilon}\exp\left(\frac{446000}{8.314T_d}\right) = 2.14 \times 10^{17} \times [\sinh(0.008\sigma_p)]^{6.1} \qquad [7\text{-}1]$$

$$Z_{321} = \dot{\varepsilon}\exp\left(\frac{465000}{8.314T_d}\right) = 9.76 \times 10^{17} \times [\sinh(0.009\sigma_p)]^{6.1} \qquad [7\text{-}2]$$

Given the same deformation conditions (e.g. same strain rate and same deformation temperature), it is evident from equation [7-1] and [7-2] that the Z parameter for 304 will be slightly lower than that of the 321 steel. This is corroborated by Figure 6.8 that if the same Z value is considered, the deformation stress values for the 304 steel will be higher than the equivalent values for the 321 steel. As may be seen from Figure 6.2 and Figure 6.8, increasing the Z value increases the critical stress and strain for the initiation of DRX. Conversely, when the Z value is low, the rate of softening becomes higher.

7.6 Comparison of the flow curves of 321 and 304 steels

The differences in the flow curves can be accounted for by using equation [3-8] whereby σ is made the subject of the formula of which the final expression becomes:

$$\sigma = \frac{1}{\alpha}\sinh^{-1}\left[\frac{1}{A_3}\dot{\varepsilon}\mathrm{exp}\left(\frac{Q}{RT_d}\right)\right]^{1/n} \qquad [7\text{-}3]$$

From this equation, it can be seen that the major contribution to differences in the flow stress curves comes from α, Q, and A_3

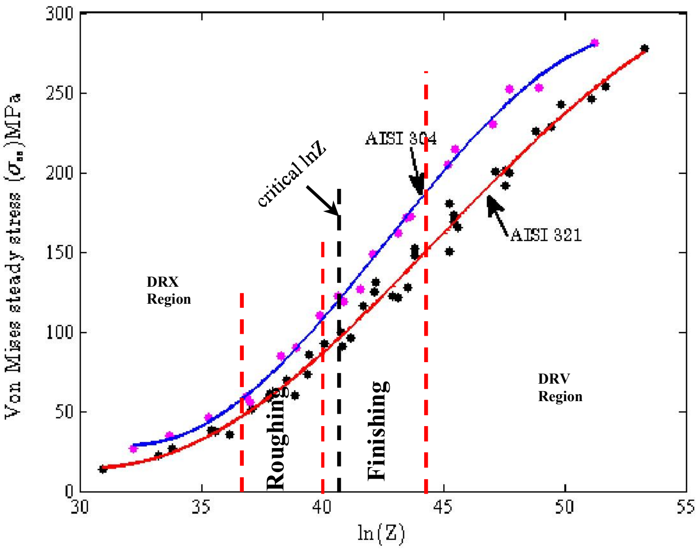

Figure 7.2: **Comparison of flow stress profiles of the two steels 321 and 304 as a function of lnZ.**

Figure 7.2 shows that if the same Z is used for hot rolling these two materials, the 321 steel will always be softer if compared to the 304 steel, both within the DRV and the DRX regions and it is, therefore, expected that the hot rolling mill loads of 304 will be higher than those for 321 at equivalent Z values. Should equivalent flow stresses be required, however, the hot rolling conditions in terms of Z of the steel 321 would have to be adjusted to a higher value than for steel 304, i.e. lower Steckel hot rolling temperatures. The dotted vertical lines in Figure 7.2 are regions taken from the mill logs through which Roughing and Steckle milling is done at the plant.

7.7 Comparison of the peak strains of 321 and 304 steels

It was observed in the flow curve profiles that exhibited DRX that the peak strain for 304 was lower than that of 321 under the same deformation conditions. The similar trend was also observed in the DRV region as can be seen in Figure 7.3. The differences in ε_p in the two steels in the DRX and DRV regions can be attributed to the structural property, differences in initial grain sizes – according to equation [3-5], the influence of titanium and accumulation of dislocations [48] given the same deformation conditions. The initial austenite grain size is affected by the reheat temperature hence in a way the reheat temperature has an influence on the peak strain. In [48][49], it is found that C, Si and Mn do not have an influence on the peak strain and it is suggested that the effect of the specific micro-alloying elements on the peak strain could be calculated cumulatively. The curves that showed characteristics of DRV, the peak strain was taken as the start of the steady state strain because the peak and start of steady state strain coincide.

Therefore, the differences in peak strains between these two steels can be attributed to the titanium addition. It can be seen from the above graph that the addition of titanium did not have much of an influence on the slope in the DRX region but there is more of a noticeable difference in the DRV region.

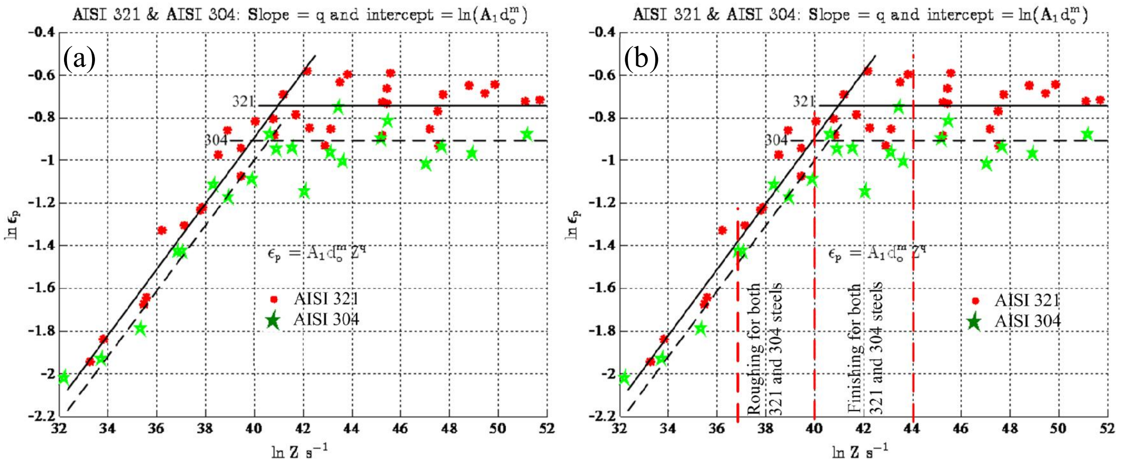

Figure 7.3: **Comparison of the peak strains for 321 and 304 as a function of lnZ with (b) indicating where rough rolling and finish rolling start and end. According to information from the mill logs, both steels have the same rolling schedule.**

7.8 Comparison of the work hardening rates of 321 and 304 steels

Figure 7.4 shows a comparison of strain hardening rate of the two steels under study and in this figure, it can be seen that the strain hardening rate for the 321 steel is consistently lower than that for the 304 steel for the same lnZ. This is in agreement with the observation from the industry that 304 steel is harder as compared to 321 steel. For clear comparison, a normalised stress σ / σ_p was used in the x-axis. A small lnZ represents dynamic recrystallisation deformation conditions (low strain rates and high deformation temperatures) while large lnZ values are for dynamic recovery conditions (high strain rates and low deformation temperatures).

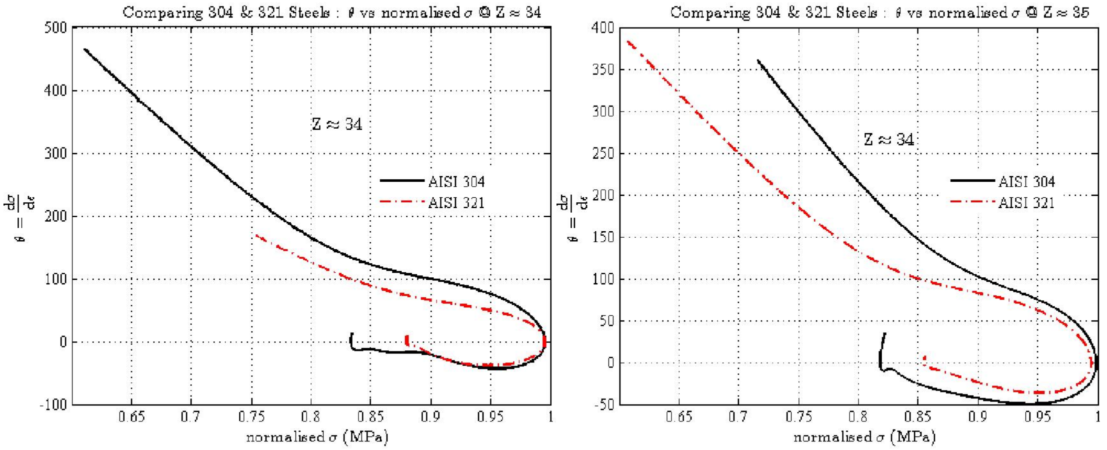

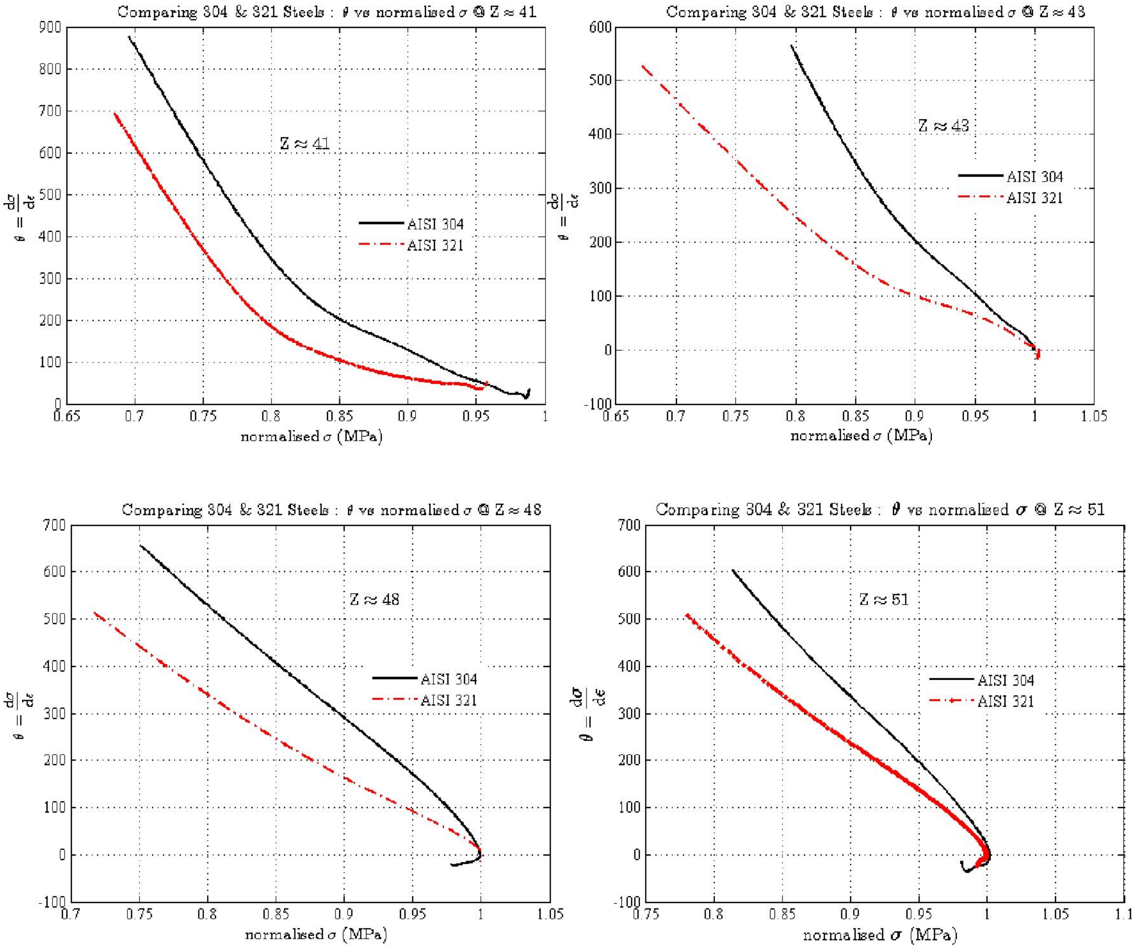

Figure 7.4: **Graphs showing the comparison of the work hardening rates at various lnZ values for 321 and 304 steels.**

There are a number of contributing factors to work hardening rate which are:

a. The activation energy
b. The particles/precipitates
c. Delta ferrite
d. The material composition and
e. The stacking fault energy among others

In theory, the lower activation energy promotes self-diffusion which in turn was supposed to lead to lower strain hardening rate. But this is not the case with what is observed in the graphs of Figure 7.4 since 321 steel has a higher activation energy as compared to 304 steel. More also, delta ferrite and Ti(CN), as explained earlier, increase activation energy and it is also more in 321 steel. The effect of material composition is very complex with literature giving conflicting information but the bottom line is that some of the chemical compositions have an additive effect while some have a negative effect on work hardening[127][128]. It can only be speculated here that the possible cause of higher work hardening rate in 304 steel could be attributed to B acting alone or BN particles that may have respectively a dragging effect on dislocations motion and pinning effect on the grain boundaries as B and N are higher in 304 steel. This may be the subject for further investigation in future work on these two steels.

The differences in work hardening rate between 321 and 304 steels can possibly also be attributed to the influence of carbon–manganese complexes in austenite [129]. It has been shown that when carbon combines with manganese it forms complexes that retard the climb rate of dislocations thereby increasing the work hardening rate.

7.9 What influences DR_{TT}?

In this study the DR_{TT} is seen to vary with three hot deformation parameters, i.e. the change in deformation temperature, the change in strain rate and the change in interpass time. As the strain rate is increased in Figures 6.2 and 6.8, the DR_{TT} moves to higher temperatures, i.e. at higher strain rates less deformation time is available for the slower DRX to take place through self-diffusion across migrating grain boundaries and more thermal energy is, therefore, required for this to take place. This means that at lower strain rates, the range in which DRX is possible is extended as was seen in Figure 5.7(a).

Figure 5.7(b) shows the effects of increasing interpass times on the DR_{TT} which shifts to slightly higher temperatures. During the interpass time, the accumulated driving force from the previous pass is consumed, either by static recrystallisation (SRX) or by static recovery (SRV). With longer interpass times the “loss in accumulated driving force” makes DRX in the following pass less likely and hence DRV is favoured, as was shown in Figure 5.7(b). For instance, it has been shown [10] that the basic fundamental principle for DRX to initiate is that the local dislocation density must accumulate high enough to allow new grains to nucleate and grow during deformation, which is less likely if dislocations are “lost” through SRX or SRV during a longer interpass time.

It is mention in literature that some further rolling parameters that can influence the DR_{TT} are the chemical composition of the steel and the pass strain [2][21][22][6], both of which were kept constant in this study. The latter was constrained by excessive barrelling taking place during compression testing at total strains exceeding 1 which was spread over 8 or 9 passes.

7.10 Prediction of hot rolling parameters using 321 steel as a study material

The results presented in this investigation together with the results from the previous study [130] can now be used to model and therefore predict mill loads under practical plant conditions. From the multipass tests, the MFS and the Z parameter were calculated per pass and the results are presented in Figure 7.5 for all the tests. A model that describes the relationship between the MFS and the Z parameter was then developed as indicated in equation [7-4]. This relationship is a third order polynomial that best fitted the results and the constants p_1 to p_4 are obtained from the coefficients of the polynomial. The model developed here is firstly used to predict the mean flow stresses using the Z values and then secondly to use the results to predict the mill loads as a function of strain rate and deformation temperature. The results obtained will be compared to the experimental values from this study and later validated with the aid of typical data from plant mill logs kindly provided by Columbus Stainless. The model makes use of the Zener – Hollomon parameter which takes into account the effects of strain, strain rate and deformation temperature on the steady state stress of the steel being deformed to arrive at a practical model for use under plant conditions. As may be seen from Figure 7.5 below, there is a good correlation between the predicted and the actual mean flow stresses. The exercise was meant to use these experimental results and arrive at a practical model for plant use.

$$\mathrm{MFS} = p_1(\ln \mathrm{Z})^3 + p_2(\ln \mathrm{Z})^2 + p_3(\ln \mathrm{Z}) + p_4 \qquad [7\text{-}4]$$

Coefficients:

$p_1 = -0.015435$

$p_2 = 2.0646$

$p_3 = -82.814$

$p_4 = 1066.1$

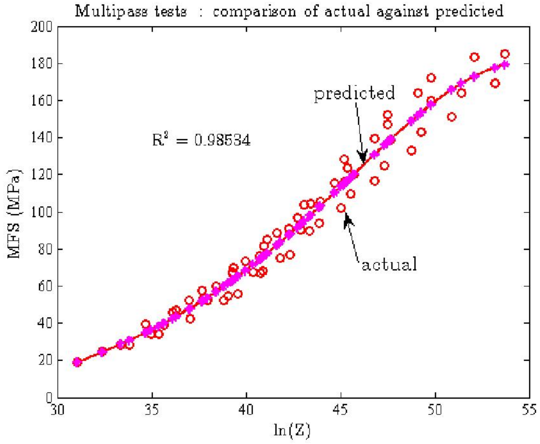

Figure 7.5: **Predicted mean flow stress (solid line) against actual mean flow stress as a function of the Z value for 321 steel.**

The Sims model for the calculation of roll force and torque in hot rolling mills under conditions of sticking friction, has been widely accepted and it makes use of the work roll flattened radius and redundant strain while others [43][131] have added forward slip under conditions where friction is less than that of sticking and the effects of front end or back end tension on the rolled steel strip. The model calculates the MFS from the mill logs as follows [43] [96][108] [132]:

$$\mathrm{MFS} = \frac{\mathrm{P}}{\frac{2}{\sqrt{3}} w \mathrm{Q} \sqrt{R'(H-h)}} \qquad [7\text{-}5]$$

with the parameter Q defined below.

To link the experimental results to the plant mill parameters, equation [7-4] is used to calculate the mean flow stresses at each pass' given temperature and strain rate as these are included in the Z parameter. Alternatively, if the Z value is known, the corresponding experimental MFS can be read off from Figure 7.5 or calculated using equation [7-4]. For example, in order to calculate the mill load, P is made the subject of the formula as in equation [7-6]:

$$\mathrm{P} = \frac{2}{\sqrt{3}} \times \mathrm{MFS} \times w\mathrm{Q}\sqrt{R'\left(H-h\right)} \qquad [7\text{-}6]$$

where P is the rolling force, w is the plate width, H and h are the entry and exit plate thicknesses respectively, R' is the flattened work roll radius which is calculated from the following Hitchcock equation [96]:

$$R' = R\left(1+\frac{\mathrm{CP}}{w\Delta h}\right) \qquad [7\text{-}7]$$

R is the nominal work roll radius, $\Delta h = H - h$, and $\mathrm{C} = \frac{16\left(1-\nu^2\right)}{\pi E}$ with E being the Young's modulus of elasticity of the outer skin of the work roll material and ν is the Poisson's ratio while the factor $2/\sqrt{3}$ adjusts the MFS to Von Mises plane strain conditions. Q is the geometrical factor given by:

$$Q = \frac{1}{2}\sqrt{\frac{1-r}{r}} \times \left[\pi \times \tan^{-1}\sqrt{\left(\frac{r}{1-r}\right)} - \sqrt{\frac{R'}{h}} \times \ln\left\{\left(\frac{Y}{h}\right)^2 \left(1-r\right)\right\}\right] - \frac{\pi}{4} \qquad [7\text{-}8]$$

Where:

$$r = \frac{\Delta h}{H} \; ,$$

$Y = 2R'\left(1-\cos\Phi\right) + h$ and

$$\Phi = \sqrt{\frac{h}{R'}} \times \tan\left[\frac{\pi}{8}\sqrt{\frac{h}{R'}} \times \ln\left(1-r\right) + \frac{1}{2}\tan^{-1}\left(\sqrt{\frac{r}{1-r}}\right)\right]. \qquad [7\text{-}9]$$

These parameters are directly obtained from the mill logs and the outcomes of the equations are fed into a spread sheet for easy manipulation. It can be seen from equations [7-4] and [7-6] that all are now known except of course the mill load P.

The Sims equation does not take into account changes in temperature and strain rate while the MFS is also a function of these parameters. Moreover, the Sims model assumes that sticking friction occurs between the work rolls and the workpiece [2][133]. However, in order to improve the accuracy of the model, forward slip and friction less than sticking friction should be considered when modelling the MFS. .

The following sequence is then followed: firstly find the activation energy of hot working which is determined using single pass isothermal deformation tests. This apparent activation energy is assumed not to change within the test/rolling temperature range and it is used to calculate the Z parameter for each pass using $Z = \dot{\varepsilon} \exp\left(\frac{Q}{RT_d}\right)$. Secondly, find the MFS per pass from multipass tests after which the relationship between Z and MFS is developed as was shown in Figure 7.5 above. The best fit relationship found (equation [4-2] above) is then used together with the Sims equation to predict the mill parameters such as mill loads and the steel's mean flow stresses.

7.11 Validation of the model

Using this method, it was initially observed that the predicted mean flow stresses by the Sims model were higher by a factor of 1.35 than those predicted by the proposed model in this study as shown in Figure 7.6(a) which, when corrected by this factor, the correlation of the MFS is as shown in Figure 7.6(b). These differences were expected as the two methods used (i.e. the Sims model and the model used in this study) are not the same in all respects; furthermore the Sims model [133] does not take the effect of slipping friction, deformation temperature and strain rate into account while the proposed model in this work takes these parameters into account in the calculations through the Z parameter. Moreover the Sims model also does not take into account any front and back end tensions from the operation of the Steckel mill. When these parameters are to be considered they should lower the Sims' predicted values closer to the experimental ones. This "correction" was partly verified by a calculation where only the coefficient of friction was used in the modified Sims equation [43]. In summary, therefore, the Sims model calculates the MFS directly from the mill logs while the proposed model uses the experimental data to calculate MFS in order to predict the mill loads. From these observations, the predictions of the rolling force and the Z parameter were put to test using plant mill logs for a seven pass Steckel mill and are as shown in Figure 7.7 and Figure 7.8.

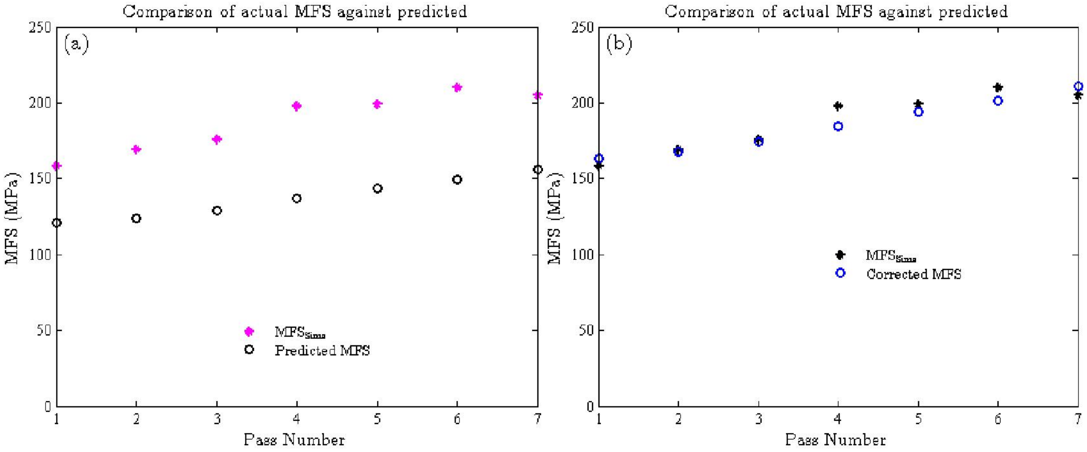

Figure 7.6: **MFS vs Pass Number showing the relationship between the actual and predicted values, (a) predicted MFS data and (b) corrected MFS data.**

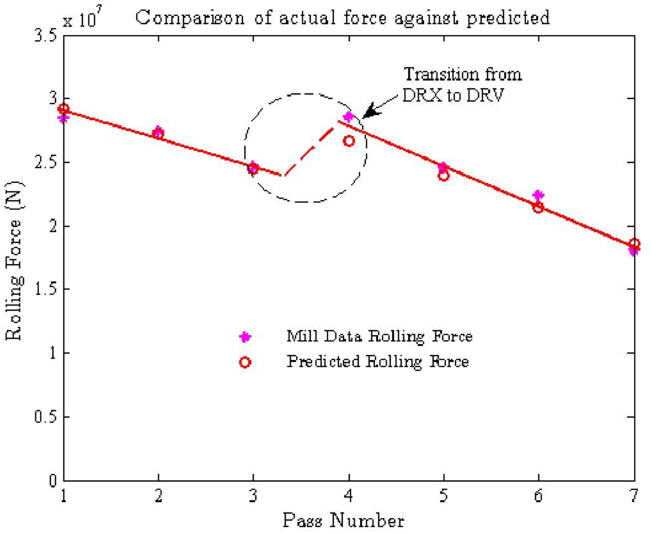

Figure 7.7: **Rolling force vs Pass Number showing the relationship between the actual and predicted for AISI 321 steel**

Figure 7.7 shows the calculated mill loads per pass using equations [7-4] and [7-6] and their comparison to the actual mill loads from the plant data. There is a “kink” between pass three and pass four which can be attributed to the microstructural change from DRX to DRV. This is substantiated by the observation that the transition from DRX to DRV occurs at about $\ln Z \approx 41$ which correlates well with pass 3 and 4.

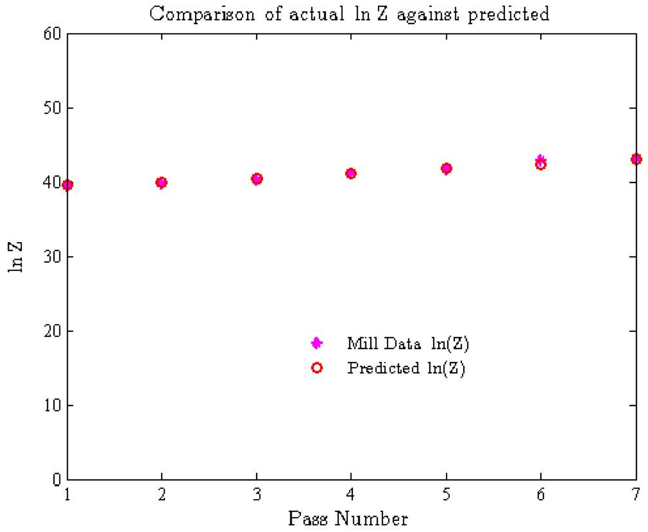

Figure 7.8: lnZ vs Pass Number showing the relationship between the actual and predicted for AISI 321 steel

CHAPTER 8: CONCLUSIONS

The hot working characteristics of AISI 321 and 304 stainless steels over a temperature range of 800 - 1200°C and over a strain rate of 0.001 – 5/s have shown the following:

1. The difference in hot working flow stress between the two steels arises from differences in A_3, Q, $\delta -$ ferrite content, free nitrogen and free carbon. The three parameters (A_3, Q, $\delta -$ ferrite) are interlinked in that they affect each other. The apparent higher levels of $\delta -$ ferrite in the steel 321, will increase the activation energy Q which in effect will also contribute to an increase in A_3. The objective in 321 stainless steels, should therefore, be to lower the $\delta -$ ferrite content by adjusting the content of austenite formers because of the loss of the C and N in solution, as the $\delta -$ferrite has a detrimental effect on the hot workability of steels.
2. A constitutive mathematical model has been developed for the evaluation and prediction of the mean flow stresses, the Z parameter and industrial mill loads for the stainless steel AISI 321 by taking into account the strain rate, the strain and the deformation temperature. This is a useful way to use laboratory obtained hot compression test results and apply them to optimise plant hot rolling processes. The comparison between the theoretical and experimental values confirms the validity of the model.
3. The critical stress and strain conditions for the initiation of dynamic recrystallisation were found to be; $\sigma_c = 0.88\sigma_p$ and $\varepsilon_c = 0.69\varepsilon_p$ for steel 321 and $\sigma_c = 0.90\sigma_p$ and $\varepsilon_c = 0.68\varepsilon_p$ for steel 304;
4. The hot working activation energy for steel 321 is significantly higher than that for 304 at 465 kJ/mol and 446 kJ/mol respectively, which affects their respective Z parameters at otherwise equivalent conditions.
5. The material structure factors for 321 and 304 steels are $9.76 \times 10^{17}\,\mathrm{MPa}^{-1}s^{-1}$ and $2.14 \times 10^{17}\,\mathrm{MPa}^{-1}s^{-1}$ respectively.
6. For the optimisation of hot working of the 321 steel, a different rolling schedule at slightly higher Z values than for the steel 304 may be adopted to achieve equivalence in the mill loads.
7. To improve the room temperature proof stress of 321 steel, the following are suggested: when rolling, the Z value must be high enough to target the DRV region and secondly, consideration should be given to change the chemistry of 321 steel to achieve a lower delta ferrite content.
8. The critical lnZ value for the transition from dynamic recrystallisation to dynamic recovery is about 41 (with Z in s^{-1}) for both steels.
9. $\mathrm{DR}_{\mathrm{TT}}$ is a useful parameter to determine the occurrence of either DRX and DRV and it was shown that in the 321 steel, both of these softening mechanisms take place during deformation, depending on the particular conditions applied.
10. At strain rates greater than $0.05s^{-1}$, dynamic recovery as a restoration mechanism was dominant pushing the dynamic recrystallisation to dynamic recovery transition

temperature ($\mathrm{DR_{TT}}$) to higher temperatures. This implied, through extrapolation, that at typical industrial Steckel strain rates of about $60s^{-1}$ no dynamic recrystallisation is likely to occur but only dynamic recovery can be expected.

11. The EBSD results confirm the findings that although the two steels are only separated by their titanium addition and also differences in delta ferrite content, their hot workabilities are somewhat different leading to small but measurable microstructural differences. This is mainly attributed to the loss of solute carbon and nitrogen in 321 steel as well as the ineffectiveness of relatively large Ti-containing carbonitride particles to provide any strengthening to hot rolled 321 steel while differences in delta-ferrite content between 304 and 321 steels may also make some contribution to differences in hot workability.

CHAPTER 9: REFERENCES

[1] "SAE steel grades." [Online]. Available: http://www.qtstools.com/TechInfo/SAE steel grades.htm. [Accessed: 01-Jun-2011].

[2] G. E. Totten, *Steel Heat Treatment Metallurgy and Technologies*, 2nd Edition. Tailor & Francis Group, 2007.

[3] J. Beddoes and J. G. Parr, *Introduction to Stainless Steels*, 3rd Edition. ASM International, 1999.

[4] R. D. Doherty et al., "Current issues in recrystallization: a review," *Materials Science and Engineering A*, vol. 238, pp. 219–274, Nov. 1997.

[5] N. D. Ryan and H. J. McQueen, "Dynamic Softening Mechanisms in 304 Austenitic Stainless Steel," *Canadian Metallurgical Quarterly*, vol. 29, pp. 147–162, 1990.

[6] F. J. Humphries, *Recrystallisation and Related Annealing Phenomena*, Second Edi. Elsevier, 2004.

[7] A. Dehghan-Manshadi, M. R. Barnett, and P. D. Hodgson, "Recrystallization in AISI 304 austenitic stainless steel during and after hot deformation," *Materials Science and Engineering A*, vol. 485, pp. 664–672, 2008.

[8] S.-I. Kim and Y.-C. Yoo, "Dynamic recrystallization behavior of AISI 304 stainless steel," *Materials Science and Engineering A*, vol. 311, pp. 108– 113, 2001.

[9] "Application Types." [Online]. Available: http://www.elinox.com.br/index.php?option=com_content&view=article&id=21&Itemid=74&lang=us. [Accessed: 01-Aug-2011].

[10] "STECKEL MILLS – Creative solutions for the metal industry." [Online]. Available: http://www.sms-siemag.com/download/W4_309_E_Steckel_Mills_save.pdf. [Accessed: 30-Nov-2011].

[11] D. Koshal, *Manufacturing Engineer's Reference Book*. Oxford: Butterworth-Heinemann, 1993.

[12] D. R. Askeland, P. . Fulay, and D. K. Bhattacharya, *Essentials of Materials Science and Engineering*, 2nd Edition. Cengage Learning, 2010.

[13] R. W. Hertzberg, *Deformation and Fracture Mechanics of Engineering Materials*. John Wiley and Sons Inc, 1996, pp. 66, 106.

[14] W. D. Callister and D. G. Rethwisch, *Materials Science and Engineering An Introduction*, 8th Edition. John Wiley and Sons Inc, 2010.

[15] W. E. Stumpf, "Dislocations and Deformation," in *Mechanical Metallurgy Class Notes*, Unpublished, 2011, p. Chapter 2.

[16] W. D. J. Callister and D. G. Rethwisch, *Fundamentals of Materials Science and Engineering An Integrated Approach*, 4th Edition. John Wiley and Sons Inc, 2012.

[17] E. Dontsova, “Understanding of edge and screw dislocations in nanostructures by modeling and simulations,” PhD thesis. University of Minnesota, 2013.

[18] R. Abbaschian, L. Abbaschian, and R. . Reed-Hill, *Physical Metallurgy Principles*, 4th Edition. Cengage Learning, 2009, p. 106.

[19] H. K. D. H. Bhadeshia and R. W. K. Honeycombe, *Steels Microstructure and Properties Third*, 3rd Edition. Elsevier, 2006.

[20] A. M. Russell and K. L. Lee, *Structure – Property Relations in Nonferrous Metals*. John Wiley and Sons Inc, 2005.

[21] M. El Wahabi, J. M. Cabrera, and J. M. Prado, “Hot working of two AISI 304 steels: a comparative study,” *Materials Science & Engineering*, vol. A343, pp. 116–125, 2003.

[22] W. Liu, “Precipitation of TiCN in austenite experimental results analysis and modelling,” PhD thesis. McGill University, 1987.

[23] S. Serajzadeh and A. K. Taheri, “An investigation of the silicon role on austenite recrystallization,” *Materials Letters*, vol. 56, pp. 984 – 989, 2002.

[24] R. W. Cahn and P. Haasen, Eds., *Physical Metallurgy*, 4th Edition. Elsevier Science B.V., 1996.

[25] G. R. Stewart, J. J. Jonas, and F. Montheillet, “Kinetics and Critical Conditions for the Initiation of Dynamic Recrystallization in 304 Stainless Steel,” *ISIJ International*. vol. 44, no. 9, pp. 1581–1589, 2004.

[26] E. Sequoia, R. W. K. Honeycombe, and R. W. Pethen, “Dynamic recrystallization,” *Less-Common Metals*, vol. 28, pp. 201–212, 1972.

[27] J. Choi, B. Seong, S. C. Baik, and H. Lee, “Precipitation and Recrystallization Behavior in Extra Low Carbon Steels,” *ISIJ International*, vol. 42, no. 8, pp. 889–893, 2002.

[28] L. T. Mavropoulos, “The Synergistic Effect of Niobium and Boron of Recrystallisation in Hot Worked Austenite,” *PhD thesis,* McGill University, 1986.

[29] E. López-Chipres, I. Mejía, C. Maldonado, A. Bedolla-Jacuinde, M. El-Wahabi, and J. M. Cabrera, “Hot flow behavior of boron microalloyed steels,” *Materials Science and Engineering A*, vol. 480, pp. 49–55, 2008.

[30] I. Mejía, A. Bedolla-Jacuinde, C. Maldonado, and J. M. Cabrera, “Determination of the critical conditions for the initiation of dynamic recrystallization in boron microalloyed steels,” *Materials Science and Engineering A*, vol. 528, pp. 4133–4140, 2011.

[31] AK Steel, "Stainless Steel Comparator."

[32] Commettee, *ASM Metals Handbook Vol 19*. ASM International, 1996.

[33] C. A. C. Imbert and H. J. McQueen, "The physical metallurgy of hot working," *Materials Science and Engineering A*, vol. 313, pp. 104– 116, 2001.

[34] E. I. Poliak and J. J. Jonas, "Initiation of Dynamic Recrystallization in Constant Strain Rate," *ISIJ International*, vol. 43, no. 5, pp. 684–691, 2003.

[35] H. Mirzadeh and A. Najafizadeh, "Prediction of the critical conditions for initiation of dynamic recrystallization," *Materials and Design*, vol. 31, no. 3, pp. 1174–1179, 2010.

[36] "Effect of Nominal Strain-Rates on the Initiation and Growth of Adiabatic Shear Bands in Steels," *Journal of Applied Mechanics*, vol. 55, no. March, 1988.

[37] M. Li and J. Zhang, "Analysis of Crack Initiation and Propagation within HDPE Pipes in Bridge Construction," *Architectural Engineering*.

[38] L. Liang-yun, Q. Chun-lin, Z. De-wen, G. Xiu-hua, and D. Lin-xiu, "Dynamic and Static Recrystallization Behavior of Low Carbon High Niobium Microalloyed Steel," *Journal of Iron and Steel Research International*, vol. 18, no. 1, pp. 55–60, 2011.

[39] A. S. Taylor and P. D. Hodgson, "Dynamic behaviour of 304 stainless steel during high Z deformation," *Materials Science and Engineering A*, pp. 1–11, 2011.

[40] J. J. Jonas, X. Quelennec, L. Jiang, and E. Martin, "The Avrami kinetics of dynamic recrystallization," *Acta Materialia*, vol. 57, pp. 2748–2756, 2009.

[41] C. M. Sellars, "The physical metallurgy of hot working," *Hot Working and Forming Processes*, vol. B35, pp. 3–16, 1980.

[42] E. I. Poliak and J. J. Jonass, "A one-parmenter approach to determining the critical conditions for the initiation of dynamic recrystallization," *Acta Materialia*, vol. 44, no. 1, pp. 127–136, 1996.

[43] G. E. Dieter, *Mechanical Metallurgy*, SI Metric. McGraw-Hill, 1988, p. 597,612.

[44] V. B. Ginzburg, *Flat-Rolled Steel Processes*. CRC Press Taylor and Francis Group, 2009.

[45] M. Shaban and B. Eghbali, "Determination of critical conditions for dynamic recrystallization of a microalloyed steel," *Materials Science & Engineering A*, vol. 527, no. 16–17, pp. 4320–4325, 2010.

[46] H. Wu, L. Du, and X. Liu, "Dynamic Recrystallization and Precipitation Behavior of Mn – Cu – V Weathering Steel," *Journal of Materials Science & Technology*, vol. 27, no. 12, pp. 1131–1138, 2011.

[47] G. E. Dieter, H. A. Kuhn, and S. L. Semiatin, Eds., *Handbook of Workability and Edited by*. ASM International, 2003, p. 18.

[48] W. Sun, C. Lu, A. K. Tieu, Z. Jiang, X. Liu, and G. Wang, “Influence of Nb , V and Ti on peak strain of deformed austenite in Mo-based micro-alloyed steels,” *Journal of Materials Processing Technology*, vol. 125–126, pp. 72–76, 2002.

[49] S. F. Medina and C. A. Hernandez, “The Influence of Chemical Composition on Peak Strain of Deformed in Low Alloy and Microalloyed Steels,” *Acta Mater*, vol. 44, no. I, pp. 149–154, 1996.

[50] H. Mirzadeh, J. M. Cabrera, and A. Najafizadeh, “Constitutive relationships for hot deformation of austenite,” *Acta Materialia*, vol. 59, no. 16, pp. 6441–6448, 2011.

[51] D. Yuan-pei, L. Ping, and X. Ke-min, “Flow behavior and microstructure evolution of TB8 alloy during hot deformation process,” *Transactions of Nonferrous Metals Society of China*, vol. 17, pp. 1199–1204, 2007.

[52] I. Shimizu, “Theories and applicability of grain size piezometers: The role of dynamic recrystallization mechanisms,” *Journal of Structural Geology*, vol. 30, pp. 899–917, 2008.

[53] M. Jafari and A. Najafizadeh, “Correlation between Zener – Hollomon parameter and necklace DRX during hot deformation of 316 stainless steel,” *Materials Science and Engineering A*, vol. 501, pp. 16–25, 2009.

[54] M. Jafari, A. Najafizadeh, and J. Rasti, “Dynamic Recrystallization by Necklace Mechanism During Hot Deformation of 316 Stainless Steel,” *International Journal of Iron & Steel Society of Iran*, vol. 4, pp. 16–23, 2007.

[55] H. J. McQueen and C. A. C. Imbert, “Dynamic recrystallization: plasticity enhancing structural development,” *Journal of Alloys and Compounds*, vol. 378, pp. 35–43, 2004.

[56] F. J. Humphreys and M. Hatherly, *Recrystallization And related Annealing Phenomena*, 2nd Edition. Elsevier Ltd, 2004, pp. 17,218–220.

[57] J. W. Cahn, “The Kinetics of Grain Boundary Nucleated Reactions,” *Acta Metallurgica*, vol. 4, pp. 449–459, 1956.

[58] W. Roberts, H. Boden, and B. Ahlblom, “Dynamic Recrystallization Kinetics,” *Metal Science*, no. MArch-April, pp. 195–205, 1979.

[59] J. G. Lenard, *Primer on Flat Rolling*, 1st Edition. Elsevier, 2007.

[60] X. Tan, “Comparisons of friction models in bulk metal forming,” *Tribology International,* vol. 35, pp. 385–393, 2002.

[61] P. Åkerstrom, B. Wikman, and M. Oldenburg, “Material parameter estimation for boron steel from simultaneous cooling and compression experiments,” *Modelling and Simulation in Material Science and Engineering*, vol. 13, pp. 1291–1308, 2005.

[62] T. M. Alan and V. Depierre, “The Validity of Mathematical Solutions for Determining Friction From the the Ring Compression Test,” *Lubrication Technology*, no. July, pp. 389–395, 1970.

[63] F. Bach, D. Bormann, M. Rodmann, and H. V. S. genannt Haverkamp, “Friction and Temperature Development in the Hot Roll Cladding Process,” *Steel Research International*, vol. 81, no. 1, pp. 48–54, 2010.

[64] R. Balakrishnan and S. Thiyagrajan, “Formability Aspects of Aluminium Alloys(Al-4Mg),” *Advanced Engineering Sciences and Technologies*, vol. 2, no. 1, pp. 119 – 124, 2011.

[65] A. I. Baltov and A. G. Nedev, “An approach to the modelling of contact friction during rolling,” *Journal of Materials Processing Technology*, vol. 53, pp. 695–711, 1995.

[66] K. Baskaran, R. Narayanasamy, and S. Arunachalam, “Effect of friction factor on barrelling in elliptical shaped billets during cold upset forging,” *Materials Science*, vol. 42, pp. 7630–7637, 2007.

[67] F. Chen and C. Chen, “On the Nonuniform Deformation of the Cylinder Compression Test,” *Engineering Materials and Technology*, vol. 122, no. April, pp. 192–197, 2000.

[68] R. Ebrahimi and A. Najafizadeh, “A new method for evaluation of friction in bulk metal forming,” *Materials Processing Technology*, vol. 152, no. March 2004, pp. 136–143, 2004.

[69] R. Hill and M. J. Sewell, “A General Theory of Inelastic Column Failure - III,” *The Mechanics and Physics of Solids*, vol. 10, pp. 285–300, 1962.

[70] B. Hum, H. W. Colquhoun, and J. G. Lenard, “Measurements of friction during hot rolling of aluminum strips,” *Materials Processing Technology*, vol. 60, pp. 331–338, 1996.

[71] Y. Im, J. Choen, and S. Kang, “Determination of Friction Condition by Geometrical Measurement of Backward Extruded Aluminum Alloy Specimen,” *Manufacturing Science and Engineering*, vol. 124, no. MAY, pp. 409–415, 2002.

[72] W. Jin, D. Piereder, J. G. Lenard, and G. John, “A study of the coefficient of friction during hot rolling of a ferritic stainless steel,” *The Scociety of Tribologists and Lubrication Engineers*, no. November, 2002.

[73] M. S. Joun, H. G. Moon, I. S. Choi, M. C. Lee, and B. Y. Jun, “Tribology International Effects of friction laws on metal forming processes,” *Tribology International*, vol. 42, pp. 311–319, 2009.

[74] J. G. Lenard, "The Effect of Temperature on the Coefficient of Friction in Flat Rolling," *Annals of the CIRP*, vol. 40, no. 1, pp. 223–226, 1991.

[75] J. G. Lenard and L. Barbulovic-nad, "The Coefficient of Friction During Hot Rolling of Low Carbon Steel Strips," *Tribology*, vol. 124, no. October 2002, pp. 840–845, 2002.

[76] Y. P. Li, E. Onodera, H. Matsumoto, and A. Chiba, "Correcting the Stress-Strain Curve in Hot Compression Process to High Strain Level," *Metallurgical and Materials Transactions A*, vol. 40A, no. April 2009, pp. 982–990, 2009.

[77] Y. Li, E. Onodera, and A. Chiba, "Friction Coefficient in Hot Compression of Cylindrical Sample," *Materials Technology*, vol. 51, no. 7, pp. 1210–1215, 2010.

[78] Y. C. Lin, Y. Xia, X. Chen, and M. Chen, "Constitutive descriptions for hot compressed 2124-T851 aluminum alloy over a wide range of temperature and strain rate," *Computational Materials Science*, vol. 50, no. August 2010, pp. 227–233, 2010.

[79] P. A. Munther and J. G. Lenard, "The effect of scaling on interfacial friction in hot rolling of steels," *Materials Processing Technology*, vol. 88, pp. 105 – 113, 1999.

[80] D. . Petty, "Friction Models for Finite Element Modelling," *Materials Processing Technology*, vol. 45, pp. 7–12, 1994.

[81] D. E. Pierce, R. P. Burns, H. M. Dauplaise, and L. J. Mizerka, "Evaluation of Solid Lubricants: The Chemistry of Sputterd MoSx Films Using Combined Thin Film Analysis Techniques," *Report,* Watertown, Massachisetts, 1990.

[82] S. V. Sajadifar, M. Ketabchi, and M. Nourani, "Mathematical Modeling For 34CrMo4 Steel During Hot Compression," *Association of Metallurgical Engineers of Serbia*, pp. 9–17, 2011.

[83] K. Shin, S. Chi, and N. Kim, "Prediction of flow stress of metallic material and interfacial friction condition at high temperature using inverse analysis," *Journal Of Mechanical Science And Technology*, vol. 24, pp. 639–648, 2010.

[84] A. P. Singh, K. A. Padmanabhan, and M. Engineering, "Axi-symmetric compression of solid cylinders Slow loading conditions," *Materials Science*, vol. 26, pp. 5481–5487, 1991.

[85] A. A. Tseng, J. Horsky, M. Raudensky, and P. Kotrbacek, "Deformation Behavior of Steels in Mushy State." *Materials & Design*, vol 22, , pp. 83–92, 2001

[86] G. J. Richardson, D. N. Hawkins, and C. . Sellars, *Worked Examples in Metalworking*. London: The Institute of Metals, 1985.

[87] T. A. Knudsen, "An experimental study of plastic deformation of materials," *PhD thesis,* Technical University of Denmark, 2008.

[88] P. R. Cetlin, S. Yue, J. J. Jonas, and T. M. Maccagno, “Influence of Strain Rate on Interpass Softening During the Simulated Warm Rolling of Interstitial-Free Steels,” *Metallurgical Transactions A*, vol. 24A, no. July, pp. 1543–1553, 1993.

[89] J. W. Bowden, F. H. Samuel, and J. J. Jonas, “Effect of Interpass Time on Austenite Grain Refinement by Means of Dynamic Recrystallization of Austenite,” *Work*, vol. 22, no. December, 1991.

[90] S. Cho and Y. Yoo, “Hot rolling simulations of austenitic stainless steel,” *Materials Science*, vol. 36, pp. 4267 – 4272, 2001.

[91] Committee, “ASM Handbook , Volume 1 , Properties and Selection: Irons , Steels , and High Performance Alloys Section,” 2005.

[92] F. Kovac, M. Dzubinsky, and J. Boruta, “Prediction of low carbon steels behaviour under hot rolling service conditions,” *Acta Materialia*, vol. 51, pp. 1801–1808, 2003.

[93] J. J. Jonas, “The Hot Strip Mill as an Experimental Tool,” *ISIJ International*, vol. 40, no. 8, pp. 731–738, 2000.

[94] W. F. Gale and T. C. Totemeir, Eds., *Smithells Metals Reference Book*, 8th Edition. 2004.

[95] J. T. Black and K. R. A., *DeGarmo's Materials & Processes in Manufacturing*, 10th Editi. John Wiley & Sons, Inc, 2008.

[96] W. Stumpf, “Grain size modelling of a low carbon strip steel during hot rolling in a Compact Strip Production (CSP) plant using the Hot Charge Route,” *The Journal of South African Institute of Mining and Metallurgy*, vol. 103, no. 10, pp. 617–632, 2003.

[97] G. Vander Voort, “Metallographic Specimen Preparation for Electron Backscattered Diffraction.” [Online]. Available: http://vacaero.com/information-resources/metallography-with-george-vander-voort/1131-metallographic-specimen-preparation-for-electron-backscattered-diffraction.html. [Accessed: 19-Sep-2013].

[98] “Sample Preparation For EBSD - Polishing.” [Online]. Available: http://www.ebsd.com/index.php/sample-preparation/sample-preparation-for-ebsd/polishing. [Accessed: 20-Sep-2013].

[99] J. L. Uvira, “Hot Compression of ARMCO Iron and Silicon Steel,” *PhD thesis,* McGill University, 1969.

[100] S. H. I. Ping-fang, A. Engstrom, B. Sundman, M. Hillert, and C. Qing, “Computational Thermodynamics and Kinetics in Materials Modelling and Simulations,” in *Proceedings of the Sino-Swedish Structural Materials Symposium*, 2007, pp. 2010–2015.

[101] W. J. Liu, S. Yue, and J. J. Jonas, "Characterization of Ti Carbosulfide Precipitation in Ti Microalloyed Steels," *Metallurgical Transactions*, vol. 20A, no. October, pp. 1907–1915, 1989.

[102] Y. Mandiang and G. Cizeron, "Precipitation of M 3 P phosphide in titanium modified type 316 stainless steel," *Material Science and Technology*, vol. 12, no. September, pp. 771–775, 1996.

[103] M. Vach et al., "Evolution of secondary phases in austenitic stainless steels during long-term exposures at 600 , 650 and 800 ° C," *Materials Characterization*, vol. 59, no. 12, pp. 1792–1798, 2008.

[104] N. Takata, H. G. Armaki, Y. Terada, M. Takeyama, and K. S. Kumar, "Plastic deformation of the C14 Laves phase (Fe,Ni)2Nb," *SCRIPTA MATERIALIA*, no. January, pp. 10–13, 2013.

[105] I. Saeki et al., "Growth process of protective oxides formed on type 304 and 430 stainless steels at 1273K," *Corrosion Science*, vol. 40, no. 8, pp. 1295–1305, 1998.

[106] N. Karimi et al., "Characterization of the oxides formed at 1000 °C on the AISI 304 stainless steel by X-ray diffraction and infrared spectroscopy," *Applied Surface Science*, vol. 254, pp. 2292–2299, 2008.

[107] H. K. Danielsen, "Z-phase in 9-12 % Cr Steels," *PhD thesis,* Technical University of Denmark, 2007.

[108] F. Siciliano, "Mathematical Modeling of the Hot Strip Rolling of Nb Microalloyed Steels," *PhD thesis,* McGill University, 1999.

[109] F. Tehovnik, B. Arzensek, B. Arh, D. Skobir, B. Pirnar, and B. Zuzek, "Microstructure Evolution in SAF 2507 Super Duplex Stainless Steel," *Materials and Technology*, vol. 45, no. 4, pp. 339–345, 2011.

[110] Y. Zhao, H. Ma, L. Wang, C. Sun, and C. Guo, "Effect of solution treatment on microstructures and mechanical properties of AISI 321 service," *Acta Metall*, vol. 24, no. 3, pp. 243–248, 2011.

[111] "Austenitic stainless steels." [Online]. Available: http://www.gowelding.com/met/austenitic.html. [Accessed: 25-Feb-2013].

[112] F. J. Humphreys, "Grain and subgrain characterisation by electron backscatter diffraction," *Journal of Materials Science*, vol. 36, pp. 3833–3854, 2001.

[113] A. Dehghan-Manshadi and P. D. Hodgson, "Dynamic recrystallization of austenitic stainless steel under multiple peak flow behaviours," *ISIJ International*, vol. 47, no. 12, pp. 1799–1803, 2007.

[114] W. Stumpf, "Hot work modelling of two equivalent low carbon strip steels produced, respectively, by the cold charge route and by the hot charge route," *Journal of South African Institute of Mining and Metallurgy*, vol. 104, no. 11, pp. 643–652, 2004.

[115] W. Zhang, J. Wu, Y. Wen, J. Ye, and N. Li, "Characterization of different work hardening behavior in AISI 321 stainless steel and Hadfield steel," *Journal of Materials Science*, vol. 45, no. 13, pp. 3433–3437, Mar. 2010.

[116] A. I. Fernández, P. Uranga, and B. López, "Dynamic recrystallization behavior covering a wide austenite grain size range in Nb and Nb – Ti microalloyed steels," *Materials Science & Engineering A*, vol. 361, pp. 367–376, 2003.

[117] S. Bao, G. Zhao, C. Yu, Q. Chang, C. Ye, and X. Mao, "Recrystallization behavior of a Nb-microalloyed steel during hot compression," *Applied Mathematical Modelling*, vol. 35, pp. 3268–3275, 2011.

[118] E. Lopez-Chipres, I. Mejia, C. Maldonado, A. Bedolla-Jacuinde, and J. M. Cabrera, "Hot ductility behavior of boron microalloyed steels," *Materials Science and Engineering A*, vol. 460–461, pp. 464–470, 2007.

[119] H. J. McQueen, S. Yue, N. D. Ryan, and E. Fry, "Hot Working Characteristics Of Steels In Austenitic State," *Journal of Materials Processing Technology*, vol. 53, pp. 293–310, 1995.

[120] F. B. Pickering, *Physical Metallurgy And The Design Of Steels*, 1st Edition. Applied Science Publishers, 1978.

[121] S. F. Medina and C. A. Hernandez, "General Expression Of The Zener-Hollomon Parameter As A Function Of The Chemical Composition Of Low Alloy And Microalloyed Steels," *Acta Metallurgica*, vol. 44, no. 1, pp. 137–148, 1996.

[122] H. J. McQueen and N. D. Ryan, "Constitutive analysis in hot working," *Materials Science and Engineering A*, vol. 322, pp. 43 – 63, 2002.

[123] K. P. Rao and Y. V. R. K. Prasad, "High temperature deformation kinetics of Al—4Mg alloy," *Journal of Mechanical Working Technology*, vol. 13, pp. 83–95, 1986.

[124] W. Stumpf, "Hot working of low carbon strip steels: are the constitutive constants universal for this class of alloy or are they material specific?," *South African Journal of Science*, vol. 102, no. 11/12, pp. 565–571, 2006.

[125] D. Li et al., "Hot deformation behavior of an austenitic Fe–20Mn–3Si–3Al transformation induced plasticity steel," *Materials and Design*, vol. 34, no. 2012, pp. 713–718, Feb. 2012.

[126] B. Verlinden, J. Driver, I. Samajdar, and R. D. Doherty, *Thermo-Mechanical Processing of Metallic Materials*, 1st Edition. Elsevier, 2007.

[127] D. T. Llewellyn, “Work hardening effects in austenitic stainless steels,” *Materials Science and Technology*, vol. 13, no. May, pp. 389–400, 1997.

[128] P. C. J. Gallagher, “The Influence of Alloying, Temperature, and Related Effects on the Stacking Fault Energy,” *Metallurgical Transactions*, vol. I, no. September, pp. 2429–2461, 1970.

[129] C. W. Siyasiya and W. E. Stumpf, “Hot Working of Carbon-Manganese Strip Steels: The Effects Of Carbon And Manganese Content,” in *19th IAS Steel Conference, Rolling and Steel Products*, 2013.

[130] R. Nkhoma, C. W. Siyasiya, and W. E. Stumpf, “Hot workability of AISI 321 and AISI 304 austenitic stainless steels,” *Acta Materialia (submitted manuscript no. A-13-1497)*, 2013.

[131] W. F. Hosford and R. M. Caddell, *Metal Formimg*, 3rd Edition. Cambridge University Press, 2007.

[132] F. J. Siciliano, K. Minami, T. M. Maccagno, and J. J. Jonas, “Mathematical Modeling of the Mean Flow Stress, Fractional Softening and Grain Size During the Hot Strip Rolling of C-Mn Steels,” *ISIJ International*, vol. 36, no. 0, pp. 1500–1506, 1996.

[133] R. B. Sims, “The Calculation of Roll Force and Torque in Hot Rolling Mills,” in *Proceedings of the Institution of Mechanical Engineers*, 1954.

CHAPTER 10: APPENDICES

10.1 Appendix A – Excel worksheet

Table 10.1 is an extract from the excel template used to calculate the Von Mises stress and strain.

Table 10.1: The extract from the excel worksheet template used

Exp/series no:	321_1100.d04	Material:	AISI 321	Cast/slab no	NA	Condition:	Hot rolled	Test date	31-08-2012		
Main purpose of test	Constitutive constants for Hot Working		Initial sample	D(0) cold mm	H(0) cold mm	D(0) hot mm	H(0) hot mm				
			dimensions	10.021	14.967	10.167	15.185				
Heat to 1250C in 4 min, soak for 15 min			Final sample	D(f) cold mm	H(f) cold mm	D(f) hot mm	H(f) hot mm				
Decrease T to T(def) in 5 sec, He quench			dimensions	16.470	6.428	16.710	6.522				
		Plan'd def t	916.3	Actual stroke	-7.988	Barrel factor	0.862				
Gleeble prg	321_1100.d04	Act def time	916.300	Plan'd strain	0.976	Plan'd str rte	0.0011				
Load cell	1.000	Plan'd def T	1100	Actual strain	0.862	Calc str rte	0.0009				
Corr factor	NA	Meas def T	1099.8	Meas cold str	0.976	Cold str rt	0.0011				
Gleeble prg data point	Gleeble time seconds	Temp. meas. Deg C	Gleeble stroke mm	Gleeble force kN	Zero'd Gleeble stroke mm	Zero'd Gleeble force N	True strain (negative)	Flow stress (no friction) MPa	Von Mises flow stress (fr=0.1) MPa	Cum stress/strain (no friction)	Cum stress/strain (fr=0.1)
0	0	1100	0.016765	-0.47157	0.0000	0.00	0.000	0.0	0.0	0.00	0.00
1	0.5	1099	0.013794	-0.59693	-0.0030	125.36	0.000	1.5	1.5	0.00	0.00
2	1	1099.9	0.0093206	-0.78474	-0.0074	313.17	0.001	3.9	3.8	0.00	0.00
3	1.5	1100	0.0051146	-0.93812	-0.0117	466.55	0.001	5.7	5.6	0.01	0.00
4	2	1099.3	-0.0001563	-1.1167	-0.0169	645.13	0.001	7.9	7.8	0.01	0.00
5	2.5	1099.9	-0.005406	-1.1135	-0.0222	641.93	0.002	7.9	7.7	0.01	0.00
6	3	1100	-0.0098422	-1.1622	-0.0266	690.63	0.002	8.5	8.3	0.01	0.00
7	3.5	1100	-0.014653	-1.2346	-0.0314	763.03	0.002	9.4	9.2	0.02	0.00
8	4	1100	-0.018867	-1.3004	-0.0356	828.83	0.003	10.2	10.0	0.02	0.00
9	4.5	1100	-0.024322	-1.364	-0.0411	892.43	0.003	11.0	10.7	0.03	0.00
10	5	1100	-0.02942	-1.4408	-0.0462	969.23	0.004	11.9	11.6	0.03	0.00
11	5.5	1100	-0.033773	-1.4916	-0.0505	1020.03	0.004	12.5	12.2	0.04	0.00
12	6	1100	-0.038572	-1.5467	-0.0553	1075.13	0.004	13.2	12.9	0.04	0.01
13	6.5	1100	-0.043572	-1.6088	-0.0603	1137.23	0.005	14.0	13.6	0.05	0.01
14	7	1100	-0.048272	-1.6766	-0.0650	1205.03	0.005	14.8	14.4	0.05	0.01
15	7.5	1100	-0.053367	-1.721	-0.0701	1249.43	0.005	15.3	15.0	0.06	0.00
16	8	1100	-0.057643	-1.7673	-0.0744	1295.73	0.006	15.9	15.5	0.06	0.01
17	8.5	1100	-0.062819	-1.826	-0.0796	1354.43	0.006	16.6	16.2	0.07	0.01
18	9	1099	-0.067486	-1.8549	-0.0843	1383.33	0.006	16.9	16.6	0.08	0.01
19	9.5	1099.5	-0.072753	-1.9155	-0.0895	1443.93	0.007	17.7	17.3	0.08	0.01
20	10	1100	-0.076911	-1.9529	-0.0937	1481.33	0.007	18.1	17.7	0.09	0.01
21	10.5	1100	-0.081533	-1.9663	-0.0983	1494.73	0.007	18.3	17.9	0.10	0.01
22	11	1099.7	-0.087643	-1.993	-0.1044	1521.43	0.008	18.6	18.2	0.10	0.01
23	11.5	1100	-0.092066	-2.0282	-0.1088	1556.63	0.008	19.0	18.6	0.11	0.01
24	12	1099.8	-0.09733	-2.057	-0.1141	1585.43	0.009	19.4	18.9	0.12	0.01
25	12.5	1099.8	-0.10177	-2.0586	-0.1185	1587.03	0.009	19.4	19.0	0.13	0.01
26	13	1099	-0.10716	-2.092	-0.1239	1620.43	0.009	19.8	19.4	0.13	0.01
27	13.5	1099.8	-0.11149	-2.1061	-0.1283	1634.53	0.010	20.0	19.5	0.14	0.01
28	14	1100	-0.11651	-2.117	-0.1333	1645.43	0.010	20.1	19.6	0.15	0.01
29	14.5	1099.9	-0.12034	-2.1177	-0.1371	1646.13	0.010	20.1	19.6	0.16	0.01
30	15	1100	-0.12642	-2.1497	-0.1432	1678.13	0.011	20.5	20.0	0.16	0.01
31	15.5	1099.1	-0.131	-2.1406	-0.1478	1669.03	0.011	20.4	19.9	0.17	0.01
32	16	1100	-0.1357	-2.1589	-0.1525	1687.33	0.012	20.6	20.1	0.18	0.01
33	16.5	1099.1	-0.14058	-2.1672	-0.1573	1695.63	0.012	20.7	20.2	0.19	0.01
34	17	1099	-0.14594	-2.1737	-0.1627	1702.13	0.012	20.7	20.3	0.19	0.01
35	17.5	1100	-0.14992	-2.1819	-0.1667	1710.33	0.013	20.8	20.4	0.20	0.01
36	18	1100	-0.15574	-2.1975	-0.1725	1725.93	0.013	21.0	20.5	0.21	0.01
37	18.5	1099.9	-0.16049	-2.2116	-0.1773	1740.03	0.014	21.2	20.7	0.22	0.01
38	19	1100	-0.16553	-2.2094	-0.1823	1737.83	0.014	21.1	20.7	0.23	0.01
39	19.5	1099	-0.17	-2.2248	-0.1868	1753.23	0.014	21.3	20.8	0.23	0.01
40	20	1099.1	-0.17533	-2.2325	-0.1921	1760.93	0.015	21.4	20.9	0.24	0.01
41	20.5	1100	-0.18081	-2.2237	-0.1976	1752.13	0.015	21.3	20.8	0.25	0.01
42	21	1099.9	-0.18517	-2.2579	-0.2019	1786.33	0.015	21.7	21.2	0.26	0.01

Table 10.2 shows the number of tests that were carried out for 321 steel together with deformation temperature, strain and strain rate and deformation time that were used during the tests.

Table 10.2: The table showing single pass experimental schedule

Test #	Temp °C	Strain	Strain rate	Def Time (s)
1	1200	1.0580	0.001	1058.0
2			0.01	105.8
3			0.1	10.58
4			1	1.058
5			5	0.2116
6	1100	1.0580	0.001	1058.0
7			0.01	105.8
8			0.1	10.58
9			1	1.058
10			5	0.2116
11	1050	1.0580	0.001	1058.0
12			0.01	105.8
13			0.1	10.58
14			1	1.058
15			5	0.2116
16	1000	1.0580	0.001	1058.0
17			0.01	105.8
18			0.1	10.58
19			1	1.058
20			5	0.2116
21	950	1.0580	0.001	1058.0
22			0.01	105.8
23			0.1	10.58
24			1	1.058
25			5	0.2116
26	900	1.0580	0.001	1058.0
27			0.01	105.8
28			0.1	10.58
29			1	1.058
30			5	0.2116
31	850	1.0580	0.001	1058.0
52			0.01	105.8

33			0.1	10.58
34			1	1.058
35			5	0.2116
36	800	1.0580	0.001	1058.0
37			0.01	105.8
38			0.1	10.58
39			1	1.058
40			5	0.2116

Table 10.3 shows the number of tests that were carried out for 304 steel together with deformation temperature, strain and strain rate and deformation time that were used during the tests.

Table 10.3: AISI 304 single hit tests schedule

Test #	Temp °C	Strain	Strain rate	Def Time (s)
1	1100	1.058	0.001	1058
2	1100		0.1	10.58
3	1100		5	0.2116
4	1050	1.058	0.001	1058
5	1050		0.1	10.58
6	1050		5	0.2116
7	1000	1.058	0.001	1058
8	1000		0.1	10.58
9	1000		5	0.2116
10	950	1.058	0.001	1058
11	950		0.1	10.58
12	950		5	0.2116
13	900	1.058	0.001	1058
14	900		0.1	10.58
15	900		5	0.2116
16	850	1.058	0.001	1058
17	850		0.1	10.58
18	850		5	0.2116
19	800	1.058	0.001	1058
20	800		0.1	10.58
21	800		5	0.2116

10.2 Appendix B - Equations

All calculations were done based on equations as presented in Table 10.1 which were taken from the paper by Stumpf [96] which were arranged in a spread sheet and the results are tabulated as in Table 10.1 below. The actual plant values were supplied by Columbus Stainless such as the roll modulus, Young's modulus E of the roll's skin which was 210 GPa while the Poisson's ratio was taken as 0.3. The rest of the values were taken from the mill logs which were supplied by Columbus Stainless. Of particular importance is how the proposed model results (indicated as predicted in table A.2) can compare with the actual values from the mill logs.

Table 10.4: Table of equations used for the mill analyses

	Equation	**Definitions**
	$R' = R\left[1 + \frac{CP}{w\Delta h}\right]$ $C = 16\left(\frac{1+\nu^2}{\pi E}\right)$	R' = fattened work roll radius (mm) R = nominal radius (mm) ν = Poisson's ratio E = Young's modulus of outer skin of roll material (GPa) P = roll force (N) w = width of the plate (mm) $\Delta h = (H-h) \rightarrow$ thickness reduction (mm)
	$\varepsilon_r = \frac{\Delta h}{4\sqrt{4(R')^2 sin^2\left(\frac{\alpha}{2}\right) - \frac{\Delta h^2}{4}}}$ $\alpha = cos^{-1}\left(1 - \frac{\Delta h}{2R'}\right)$	ε_r = redundant strain
	$V_e = V_t\left[1 + \left\{\left(\frac{2R'}{h}cos\Phi_n - 1\right)\left(1 - cos\Phi_n\right)\right\}\right]$ $\Phi_n = \left(\frac{h}{R'}\right)^{1/2} tan\left[\frac{\pi}{8}\left(\frac{h}{R'}\right)^{1/2} ln(1-r) + \frac{1}{2}tan^{-1}\left(\frac{r}{r-1}\right)^{1/2}\right]$	$r = \frac{\Delta h}{H}$ V_e = exit strip speed (corrected for forward slip) in m/s V_t = tangential velocity of working roll = $2\pi R'U$ U = revolutions/sec of working roll
	$MFS_{Sims} = \frac{P}{\frac{2}{\sqrt{3}} wQ\sqrt{(R'\Delta h)}}$ $Q = \frac{1}{2}\left(\frac{1-r}{r}\right)^{1/2}(K_3 - K_4) - \frac{\pi}{4}$	MFS_{Sims} = mean flow stress according to Sims (MPa) P = roll force (MN) W = plate width (mm)

	$K_1 = \frac{\pi}{8}\left(\frac{h}{R'}\right)^{1/2} ln(1-r)$ $K_2 = \frac{1}{2} tan^{-1}\left(\frac{r}{1-r}\right)^{1/2}$ $K_3 = 2\pi K_2$ $K_4 = \left(\frac{R'}{h}\right)^{1/2} ln\left[\left(\frac{Y}{h}\right)^2 (1-r)\right]$ $\Phi = \left(\frac{h}{R'}\right)^{1/2} tan(K_1 + K_2)$ $Y = 2R'(1-cos\Phi)+h$	
	$\varepsilon_m = \frac{0.1048R'U\varepsilon_T}{\sqrt{R'\Delta h}(FSR)}$ $\varepsilon_T = \varepsilon_n + \varepsilon_r$ $V = \frac{2\pi R'U}{60} = 0.1048R'U(m/s)$	ε_m = corrected strain rate (/s) U = roll speed in RPM FSR = forward slip ratio = $\frac{V_e}{V_t}$ ε_T = total strain per pass ε_r = redundant strain ε_n = nominal strain per pass
	$\varepsilon_n = \frac{2}{\sqrt{3}} ln\left(\frac{H}{h}\right)$	$\frac{2}{\sqrt{3}}$ = Von Mises conversion for plane strain
	$t_{ip} = \frac{Y(FSR)}{V_t}$	Y = interpass distance (m) V_t = peripheral roll speed (m/s)

10.3 Appendix C – Extract of the calculated results

Table 10.5 shows an extract of the results obtained from simulated and actual mill log values.

Table 10.5: The comparison between the predicted Z, load and MFS against the actual values from the mill logs

321 stainless steel							
Pass	**P1**	**P2**	**P3**	**P4**	**P5**	**P6**	**P7**
Entry height H (mm)	25.68745	17.62809	12.23977	8.857164	6.238854	4.645786	3.643891
Exit height h (mm)	17.6518	12.32631	8.919522	6.303156	4.686196	3.67386	3.020233
Entry Temp (℃)	1029.977	1034.169	1027.277	1014.294	998.896	983.4908	962.8185
Exit Temp (℃)	1030.766	1031.385	1016.576	1008.898	985.7334	965.2961	940.0677
Δh (mm)	8.035646	5.301778	3.320249	2.554008	1.552658	0.971926	0.623658
Cumulative Δh (mm)	-8.03565	-13.3374	-16.6577	-19.2117	-20.7643	-21.7363	-22.3599
True strain per pass (ratio)	-0.37516	-0.35776	-0.31645	-0.34018	-0.28618	-0.23472	-0.18772
Cummulative true strain (ratio)	-0.37516	-0.73292	-1.04937	-1.38955	-1.67572	-1.91044	-2.09816
Interpass time	-	11.18312	13.52769	16.1114	20.98068	21.935	-
Nominal Strain per pass (ratio)	0.433203	0.413103	0.365403	0.392802	0.330447	0.271029	0.216758
Redundant Strain (ratio)	0.030948	0.024863	0.019394	0.01663	0.012626	0.00961	0.007453
Cummulative strain (ratio)	0.464151	0.437965	0.384797	0.409432	0.343073	0.280639	0.224211
Strain rate (/s)	17.28805	29.03056	40.16162	60.85073	77.34125	88.104	95.59377
compression ratio r (ratio)	0.312824	0.300757	0.271267	0.288355	0.248869	0.209206	0.171152
Vr (m/s)	2.507517	3.580715	4.367394	5.365523	6.112525	6.408496	6.67953
Ve (m/s)	2.71887	3.875259	4.691434	5.797855	6.532501	6.773268	6.985746
Forward Slip Ratio (FSR) (ratio)	1.084288	1.082258	1.074195	1.080576	1.068708	1.05692	1.045844
R Flattened Radius (mm)	526.3849	537.3807	552.5326	577.8083	609.1286	657.972	701.842
Alpha (radians)	0.123633	0.099368	0.077538	0.066497	0.050493	0.038436	0.029811
U (rev/min)	47.64989	68.04368	82.99279	101.9601	116.1552	121.7795	126.9299
theta_n (radians)	0.053662	0.043713	0.034761	0.029737	0.023039	0.017854	0.014062
width (mm)	1571.62	1573.569	1574.51	1574.706	1573.535	1571.178	1540.672
K1	-0.02698	-0.02128	-0.01579	-0.01395	-0.00986	-0.00689	-0.00484
K2	0.296775	0.290233	0.273913	0.283431	0.261146	0.237529	0.21326
K3	1.864689	1.823587	1.721049	1.780848	1.640828	1.49244	1.339951
K4	-1.24405	-1.39533	-1.43007	-1.84936	-1.80748	-1.70458	-1.52748
C	0.021109	0.021109	0.021109	0.021109	0.021109	0.021109	0.021109
r	0.312824	0.300757	0.271267	0.288355	0.248869	0.209206	0.171152
Y	19.0014	13.26266	9.541185	6.783956	4.995016	3.876434	3.155327
Phi	0.05064	0.041745	0.033544	0.028847	0.022517	0.017547	0.013874
Q	1.51837	1.668663	1.796981	2.066077	2.209957	2.322453	2.369677
Roll force (N) - Mill logs data (actual)	28412961	27417740	24648144	28545512	24554613	22379157	18055117
Roll force (N) - Predicted	28855518	26810435	24116326	26332815	23631612	21196796	18339204
(SIMS) MFS (MPa)	158.5477	169.4166	176.1414	197.7969	198.8434	210.0302	204.7098
predicted MFS (MPa)	161.0172	165.664	172.3409	182.4647	191.3689	198.9336	207.9308
ln(Z) - Predicted	39.63	39.96	40.44	41.17	41.83	42.41	43.13
ln(Z) - Mill logs data (actual)	39.42	39.82	40.19	41.17	41.7	42.97	43.09